J. Indian Inst. Sci., Jan.–Feb. 1995, 75, 71–136

IISc THESES ABSTRACTS

Thesis Abstract (Ph.D.)
Crystal growth and characterization of some nonlinear optical materials (LAP, KTP and $LiNbO_3$) by G. Dhanraj
Research supervisor: H. L. Bhat
Department: Physics

1. Introduction

The progress made in the field of nonlinear optics (NLO) over the past three decades has led to the development of a new branch of science. Hundreds of materials have been identified possessing reasonable optical nonlinearity. Despite this, even today only a handful of NLO materials are used in applications. It is therefore appropriate to study the growth and properties of important as well as promising NLO materials in greater detail with their possible applications in mind. In the present study, the growth and properties of three important nonlinear optical materials, *viz*., L-arginine phosphate monohydrate (LAP), potassium titanyl phosphate (KTP) and lithium niobate ($LiNbO_3$) were studied. These materials are used in visible to IR region. LAP has higher nonlinearity and damage threshold, and is less deliquescent when compared to KDP and is expected to be used in laser fusion[1]. KTP has excellent combination of properties like high nonlinearity, high damage threshold, less temperature sensitivity and is nonhygroscopic[2]. $LiNbO_3$ has become a multidimensional material because of its different technological applications in nonlinear optics, electrooptics, SAW devices, optical waveguides and tunable solid-state lasers[3].

2. Crystal growth and characterization

(a) *L-Arginine phosphate monohydrate*: A systematic study on the growth of LAP crystals from solution was carried out with special emphasis on the methods to prevent the growth of undesirable microorganisms and colouration of the solution. The study on the effect of pH value on solubility and habit revealed that the pH of the solution has significant influence on them. The X-ray topography of the grown crystals clearly demonstrated the influence of growth conditions and seeding process on the defect content in them. Polarised Raman and IR spectra were recorded and the symmetries of molecular vibrations were determined. In the Raman spectra, lattice lines are fairly strong and show pronounced intensity variations with the orientation of the crystal. Thermal expansion was measured as a function of temperature and was found to be highly anisotropic. Correlating this with the crystal structure it is found that the thermal expansion is maximum in the direction perpendicular to the chains of arginine molecules. The higher damage threshold reported for DLAP as compared to that of LAP is consistent with the thermal expansion data. Despite being a complex organic crystal the temperature variation of dielectric constant shows a behaviour similar to that of an ionic crystal. No anomaly was observed in any of these properties from LN_2 temperature up to its decomposition. The damage threshold and powder efficiency were measured, and SHG was demonstrated in single crystals cut to phase matching orientation. A few experiments were also carried out on the growth of DLAP crystals.

(b) *Potassium titanyl phosphate*: KTP crystals were grown from potassium phosphate ($K_6P_4O_{13}$) flux by slow cooling method. The crystals grown under different conditions exhibited different dendritic structures on their habit faces. Detailed microscopic studies show that the growth on {100} takes place by layer, whereas that on {011} by hillocks. X-ray topography and chemical etching in addition to revealing low dislocation density prove that the hillocks were at the emerging points of dislocations on {011} planes. The laser damage threshold was measured and second harmonic generation studies (SHG) were undertaken. Figure 1 shows frequency doubling of Nd:YAG infrared (1064 nm) laser using KTP crystals. SHG study on KTP powders synthesized in different conditions show that KTP prepared in oxygen atmosphere is more efficient.

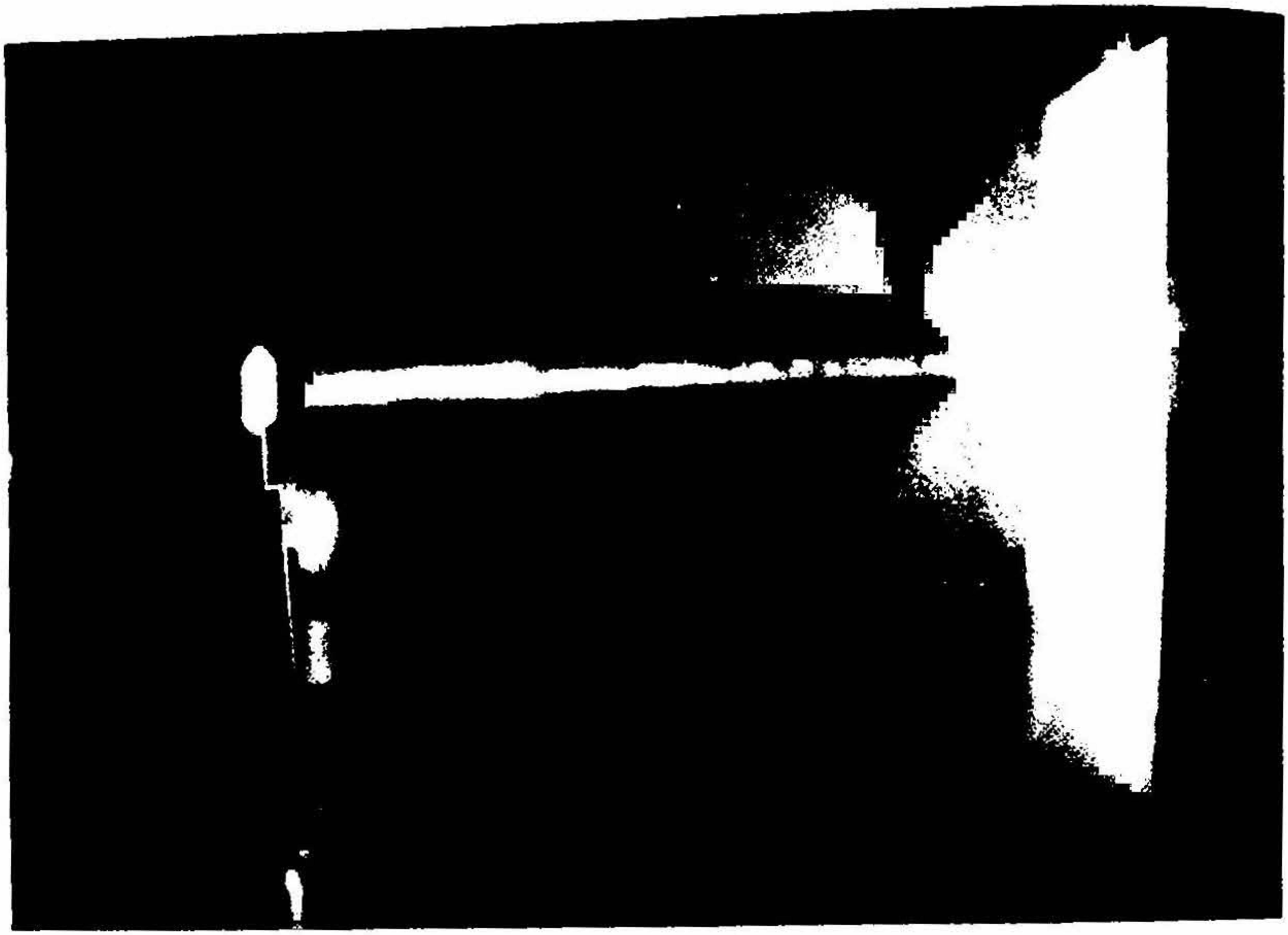

FIG. 1. Phase-matched second harmonic generation (SHG) of Nd:YAG laser, from infrared (1064 nm) to green (532 nm) wavelength, using KTP crystal.

(c) *Lithium niobate*: High-quality $LiNbO_3$ crystals were grown by Czochralski technique. The diameter of the crystals could be increased considerably by optimizing the after-heater configuration. Post-growth poling was carried out to obtain single-domain crystals. The dc conductivity was measured. From the indentation studies, microhardness variation between positive and negative domains was clearly established, wherein the negative domains show higher hardness than the positive domains. Optical quality of the crystals was assessed using optical absorption and conoscopy. These tests suggest that the grown crystals are of high optical homogeneity which is required for optical device applications.

3. Conclusions

LAP, KTP and $LiNbO_3$ single crystals were grown using three different technologically important growth methods. The quality of these crystals was assessed using chemical etching, X-ray topography, conoscopy and optical absorption methods. Raman, IR, thermal expansion, dielectric, electrical resistivity, microhardness, damage threshold and SHG studies were carried out on these crystals. The crystals were found to be of high optical homogeneity and suitable for device applications.

References

1. EIMERL, D., VELSCO, S., DAVIS, L., WANG, F., LOIACONA, G. AND KENNEDY, G. *IEEE J.*, 1989, QE-25, 179.
2. BELT, R. F., GASHUROV, G. AND LIU, Y.S. *Laser Focus*, 1985, 21, 110.

Properties of lithium niobate, *INSPEC-EMIS Data Rev.* Series No. 5, 1989.

Thesis Abstract (Ph.D.)

Algorithms for parallel compilation by N. Viswanathan

Research supervisor: Y. N. Srikant
Department: Computer Science and Automation

1. Introduction

The need for efficient and speedy compilation techniques cannot be overemphasized. With a host of different multiprocessor configurations now becoming available, parallel compilation issues have received wide attention[1]. Also, with new parallel languages and language features being tried, the question of their success depends on the compiler used. System response utilization and programmer productivity depend very much on the compiler.

The concept of incremental compilation has greatly improved recompilation speeds. By recompiling only *around* the modified parts of a program, incremental compilers save time and improve system response. Incremental compilers form a central component of integrated programming environments. In demand-driven mode, incremental compilers delay recompilation until program execution is required. Such a strategy provides immediate system response, but the preparation time for execution is high[2]. We propose to overcome this drawback by exploiting fine-grain parallelism at recompilation time. With this in mind, we propose a parallel incremental LR parser and a parallel attribute evaluator.

2. Parallel incremental LR parsing

We describe a new algorithm for parallel incremental LR parsing. The method can be used for non-incremental parallel parsing also. Our aim is to compile programs initially in parallel and then during the edit, compile and run cycle, we recommend the usage of a smaller number of processors to support incrementality. A shared memory multiprocessor model permitting concurrent read is assumed. We associate processors to parse corrections independently with minimum reparsing. A new compatibility condition is used by the associated processors to terminate reparsing and prevent redoing the work of other processors. We give an efficient parallel algorithm for assembling the final parse tree from the individual parses. We derive the compatibility information from an analysis of the LR(0) DFA at the parser construction time itself. Compatibility information is stored in a table and tested in constant time during parsing. Algorithm complexity, initial preprocessing (extra work), processor assignment, speedup and extra table space used have been discussed. Preliminary simulation studies with speedup analysis have been carried out for a subset of Pascal and we have obtained encouraging speedups by our algorithm.

3. Parallel attribute evaluation

Parallel tree contraction technique was first introduced by Miller and Reif [3]. The method employs a leaf cutting operation to contract a tree with n leaves into a single node in $O(\log n)$ time using $n/\log n$ processors on a EREW PRAM[4]. In addition to arithmetic expression evaluation, tree contraction has been applied to a wide variety of problems. We have applied tree contraction to evaluate attribute expressions in parallel. Attribute expression operators can have multiple operands and are not restricted to binary arithmetic operators. Also, multiple attributes may become available from each node of the attributed parse tree. The domains for the attributes and the operators on the domains are taken to be the same as that allowed in NEATS (New Extended Attribute Translation System)[5]. Given this predefined set of domains and operators for the attributes, we introduce a new evaluation method. We associate a priori attribute functions with intermediate results to the operators. As parse tree contraction is performed, attribute functions are composed to evaluate the attribute values. For an attribute grammar with only synthesized attributes, using our tree contraction method, we can compute all the attributes of a parse tree with n nodes in O (log) n time using n processors on a CREW PRAM model. For attribute grammars allowing inherited attributes also, we construct a new class of evaluators called the *m-pass* parallel attribute evaluators having two alternating pass types: synthesized attributes evaluation pass and inherited attributes evaluation pass. In the synthesized attributes evaluation pass, we exclusively compute synthesized attributes using our parse tree contraction method. In the inherited attribute evaluation pass, we compute in parallel only inherited attributes by the recursive doubling algorithm[6]. We evaluate all the attributes of a parse tree with n nodes in $O(m \log n)$ time using n processors on a CREW PRAM model, where m is decided by the attribute grammar. We have implemented our technique using simulation to show that the method is feasible in practice. It can be adapted to multiprocessor models of computations in a straightforward way.

4. Conclusion

We have designed new efficient algorithms for parallel incremental LR-parsing and parallel attribute evaluation. Our theoretical analysis and simulation studies show that these will be useful in practice.

References

1. Akker, R. Op Den, Alblas, H., Nijholt, A. and Luttighuis, P.O.	*An annotated bibliography on parallel parsing.* Memoranda Informatica 89-67, 1989, Department of Computer Science, Twente University, The Netherlands.
2. Ford, R. and Sawamiphakdi, D.	A greedy concurrent approach to incremental code generation. In *Conf. Record of the 12th ACM Symp. on Principles of Programming Languages,* January 1985.
3. Miller, G. L. and Reif, J. H.	Parallel tree contraction and its applications. In *Proc. of the 26th Annual IEEE Symp. on Foundations of Computer Science,* pp. 478–489, 1985.
4. Karp, R. M. and Ramachandran, V.	*A survey of parallel algorithms for shared-memory machines,* Technical Report UCB/CSD 88/408, Computer Science Division, University of California, Berkeley, CA, March 1988.
5. Riis, H. and Madsen, M.	The *NEATS system,* DAIMI MD-44, May 1982.
6. Gibbons, A. M. and Rytter, W.	*Efficient parallel algorithms,* 1988, Cambridge University Press.

Thesis Abstract (Ph.D.)

Laser processing of ductile iron by S. P. Gadag

Research supervisor: M. N. Srinivasan

Department: Mechanical Engineering

1. Introduction

High-energy sources, *viz.*, tungsten inert gas (TIG), plasma, electron beam (EB) and lasers, have been employed for improving thermo-mechanical[1-3] and electro-chemical[4,5] characteristics of the surfaces of engineering materials. In this investigation, a critical assessment of the engineering application of layer surface treatment of structure sensitive, hypereutectic ductile iron by CW CO_2 and pulsed Nd–YAG laser has been taken up. The process of laser melting has been numerically simulated by 3d finite difference method and experimentally verified. Onset of solid-state transformation, superficial or complete melting derived from numerical and experimental methods, has also been investigated. Melt and transformation profiles influenced by processing parameters, macro and micro hardness, dry sliding wear and friction, corrosion and cavitation erosion in deionised water, synthetic sea water or mild acid, have been evaluated. This has provided a better understanding of the properties of laser surface-modified ductile iron and its processing.

2. Experimental programme

Ductile iron with Bull's eye pearlitic matrix (SG 600/3 grade) was surface treated by a 300 W-pulsed Nd–YAG and a 5 kW CW CO_2 laser. Rectangular plates cut from keel blocks poured in an automotive foundry, machined to 150 × 50 × 25 mm, were laser treated. Plates mounted on a CNC work table were moved under the stationary laser beam along their length, to obtain single stripe glazed tracks at predetermined conditions. Micro and macro hardness, structure, profile of melted and frozen, transition and transformed zones were studied. Successive line scans with ≈10% overlap, resulted in a laser-modified area for X-ray and cavitation erosion studies. Flat faces of cylindrical pins were laser treated for corrosion and sliding wear tests. Processing parameters using Nd–YAG laser ranged from 100 to 140 W of average power, at two energy levels of 14 and 20 J/pulse, pulse width of 15 to 19 mS with 5 to 10 Hz of pulsing frequency. An unoscillated CO_2 CW laser beam of 1–2 mm diameter, operating in near uniform or top hat mode was employed at power levels between 0.5 and 2.5 kW and scan rates of 7.5 and 50 mm s^{-1} to obtain a wide range of lasing conditions.

3. Main results and discussion

3.1. *Numerical formulation*

Simulation, modeling and computer-aided thermal analysis of laser surface treatment by a 3D quasi-steady state moving heat source, FDM program was specially developed for the purpose. This program considers Gaussian or top hat mode energy distribution in the laser beam, energy absorptivity of the material varying with temperature, temperature-dependent thermophysical properties, radiative and connective heat transfer from the melt surface, latent heat absorption during melting and liberation during freezing, over a range of temperatures in alloys employing non-equilibrium Scheil's $\mathcal{F}_s$–T relationship. Melt profiles by computation are in close conformity with the experimental results.

Temperature profiles and freezing rates in the laser-processed zone have been computed. The typical freezing time for the eutectic solidification during laser melting with 3 mm Φ, 2.5 kW CO_2 CW laser scanned at 18 mm s^{-1}, varied between 3 and 9 mS. The peak surface temperature, T_p (Fig. 1a), attained at the surface increased

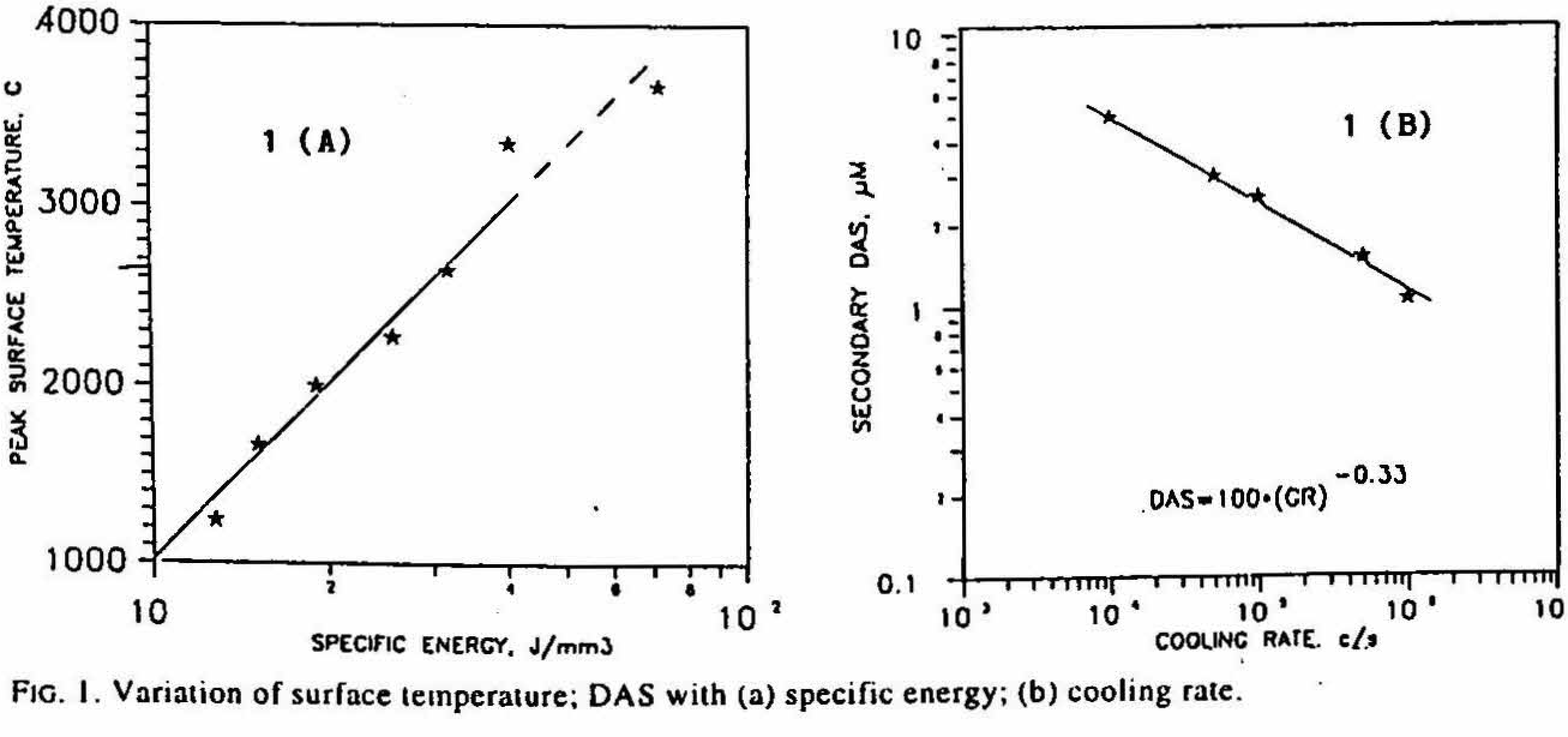

FIG. 1. Variation of surface temperature; DAS with (a) specific energy; (b) cooling rate.

linearly with the incident specific energy, $\left(\frac{P}{U-D_b^2}\right)$,(P-power, U-scan rate and D_b-beam dia.) in accordance with the equation:

$$T_p = 1444 \times \ln\left(\frac{P}{U.D_b^2}\right) - 2312.$$

Onset of transformation hardening, superficial or full melting has been computed from this. Peak cooling rates at the centre of the melt pool is of the order of 10^4 to 10^6 °C s^{-1} depending on the laser processing parameters. The cooling rate has a pronounced effect on the resulting microstructure. Eutectic of γ Fe–Fe_3C was typical dendritic at high cooling rates transforming to feathery at a low cooling rate. Secondary dendrite arm spacing (λ_2) of retained austenite in the eutectic ledeburite of the melt zone, varied (Fig. 1b) from 1 to 5 μm, had an inverse correlation with the freezing rate, G.R °C s^{-1} obtained:

$$\lambda_2 = 100.(G.\ R)^{-0.33}.$$

3.2. *Laser processing*

The depth of melt, transformed or superficial melt with transformed zone, in the laser-processed iron, each bear a log-linear relationship with energy intensity. The miminum energy intensity to initiate transformation or melting, termed 'threshold energy', was 1.1 J mm^3 and 12 J mm^{-3}, respectively (Fig. 2). Energy intensity required to obtain a given melt depth by Nd–YAG pulsed laser was considerably smaller by an order of magnitude than that for CO_2 CW laser (Fig. 3a).

The hardness at the surface of the lased tracks increased logarithmically with energy intensity–maximum hardness attained was 45 Rc for Nd–YAG laser and 60 Rc for CO_2 CW laser (Fig. 3b). The microhardness of rapidly solidified melt zone consisting of ultrafine ledeburite was 700 to 900 $Hv_{0.2}$.

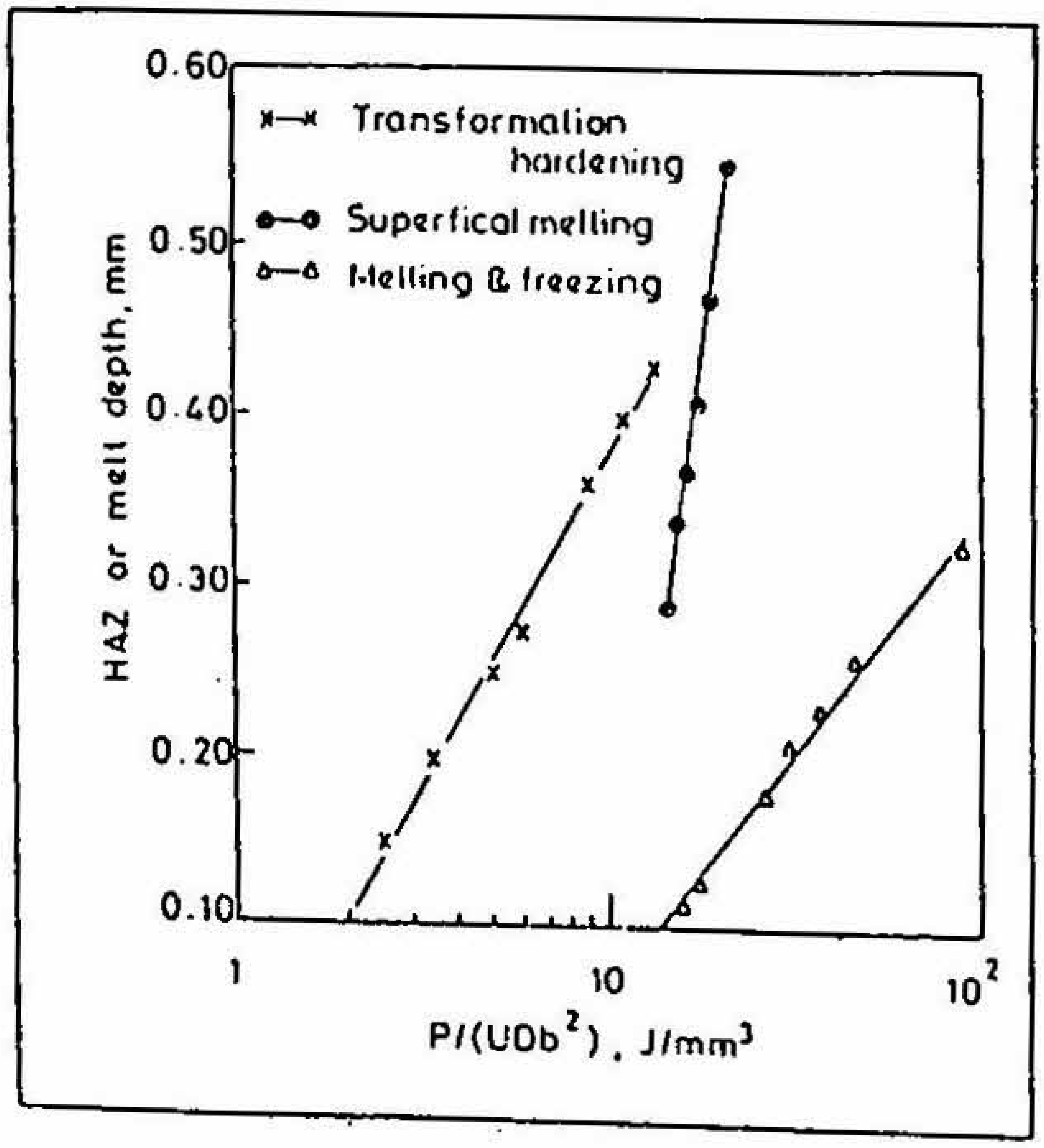

FIG. 2. Specific energy for hardening and melting.

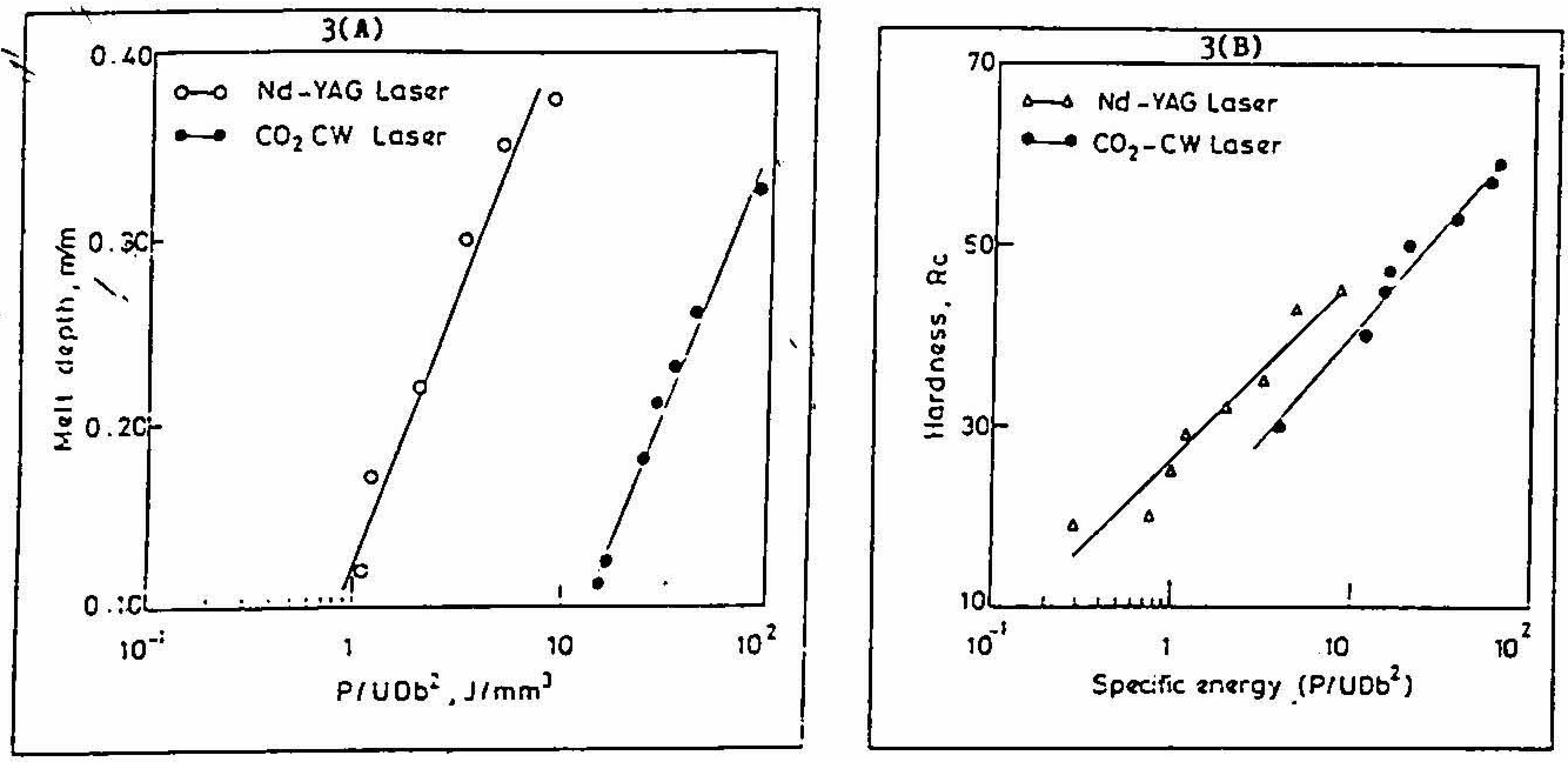

FIG. 3. Comparison of pulsed Nd-YAG and CW CO_2 high-power lasers.

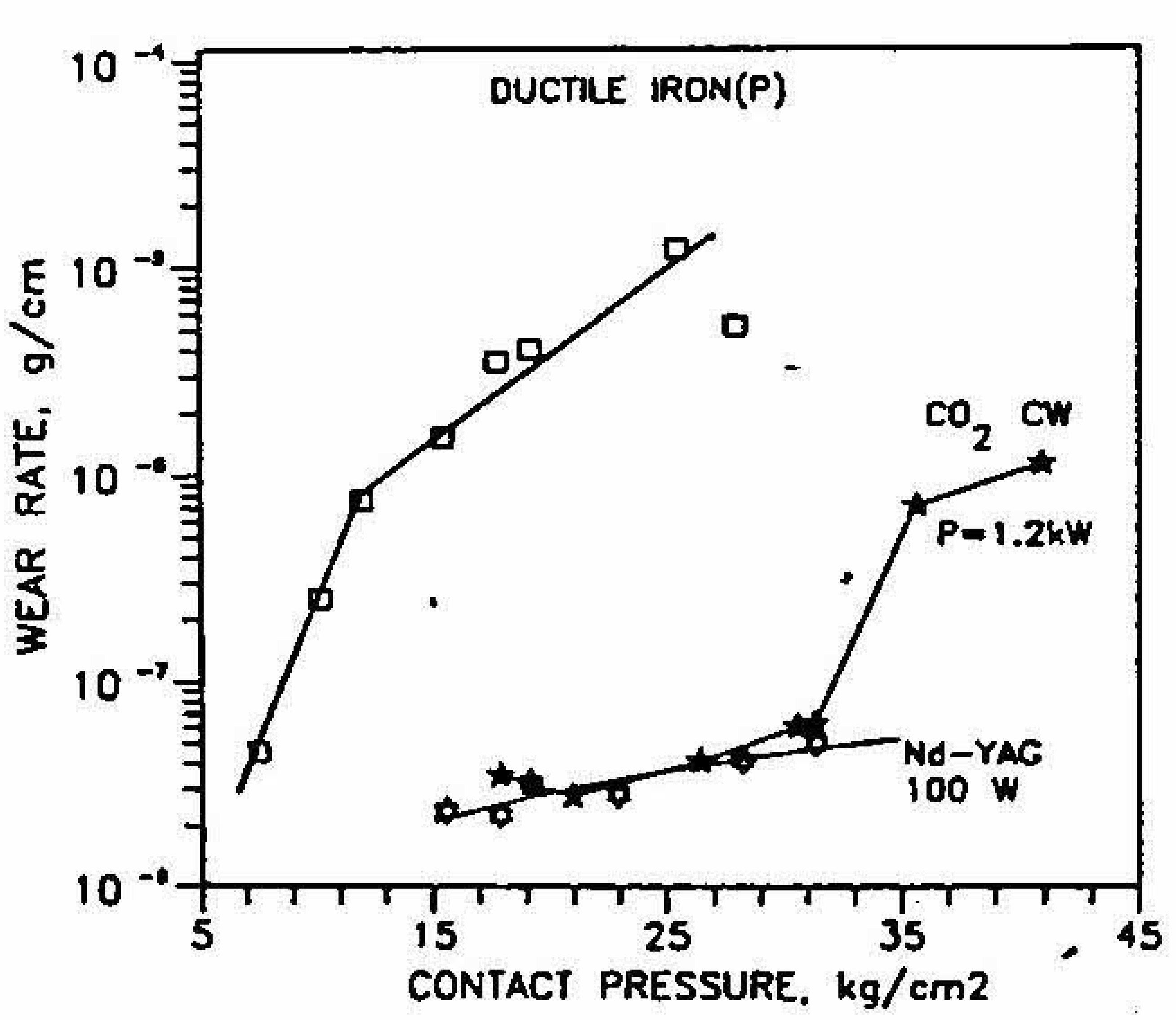

FIG. 4a. Wear-laser-treated ductile iron, sliding. speed–7.5 m/s

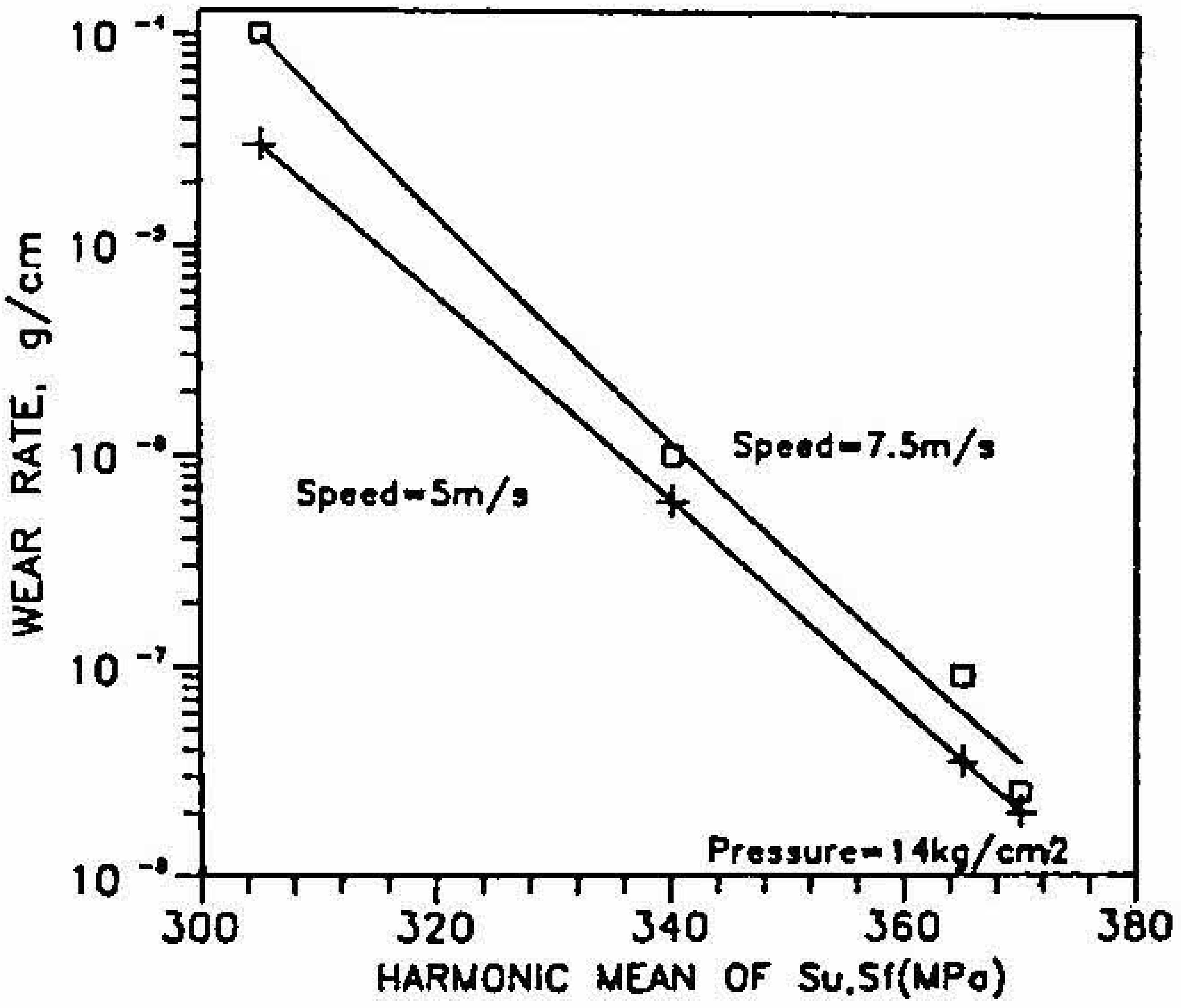

FIG. 4b. Wear rate *vs* harmonic mean of fatigue and tensile strength

3.3. *Wear and friction*

Dry sliding wear and friction of cylindrical pin specimens rubbing over a hardened steel disc (62–64 Rc) at high speeds (5 and 7.5 m s^{-1}) have been determined over a length of 5 to 6 km. The wear rate, friction coefficient (μ) and transition pressure of laser-treated samples were compared with those of the substrate and a chilled white iron from the same material. In laser-treated iron, subjected to a pressure of 30 kg cm^{-2}, wear rate was less than 10^{-7} g cm^{-1} (Fig. 4a). This was in the mild regime characterised largely by oxidative type of wear compared to severe metallic wear in ductile iron substrate at pressure higher than 8 kg cm^{-2}. Mild to severe wear, transition pressure has been determined for laser-processed ductile iron at 32 to 33 kg cm^{-2} at 7.5 m s^{-1} sliding speed, compared to 6 to 8 kg cm^{-2} for untreated ductile iron and 20 kg cm^{-2} for chilled iron.

Friction coefficient of ductile iron rubbing on a steel disc at 5 m s^{-1} was 0.2 to 0.23, for chilled iron, 0.3 to 0.4 and for laser-melted samples, 0.24 to 0.27 and laser-hardened, 0.15 to 0.2. Wear resistance of a material bears a direct relationship with harmonic mean of its uniaxial tension and rotating bending fatigue strength (Fig. 4b).

The predominant effect of laser melt treatment is not only the retention of the regime of mild equilibrium wear but also four-fold increment in the transition pressure for mild to severe wear. This could be attributed to the structural stability of interdendritic network of cementite in the ledeburite eutectic having high hardness and enhanced resistance to plastic flow.

3.4. *Cavitation erosion*

Cavitation erosion of ductile iron by ultrasonic vibratory testing at 20 kHz and 25 µm amplitude, decreased significantly on laser surface processing. Mean depth of penetration rate, MDPR, for ductile iron in water, slurry of SiC (220 grit/65 µm/grain size), synthetic sea water, and 0.01N H_2SO_4 were 11, 23, 40, and 86 µm/h respectively. Corresponding values for laser-processed ductile irons in the same order were 10, 3, 6 and 12 µm/h. Resistance to cavitation erosion improved by nearly a factor of 7. Cavitation erosion rate decreased with increasing pH of the medium (Fig. 5).

3.5. *Corrosion*

Potentio-dynamic polarisation studies of ductile iron have shown a marked improvement in corrosion resistance in dilute sulphuric acid on laser surface treatment. The corrosion current density, I_{corr} of ductile iron in 0.01N and 0.1N H_2SO_4 were 250 and 525 mA cm^{-2}, respectively; in laser-treated iron reduced to 100 and 200 $mAcm^{-2}$, respectively. Laser melting effectively reduced the corrosion rates in acid media by nearly 40%. On the other hand, its improvement in synthetic sea water was marginal.

4. Conclusions

Laser surface processing of ductile iron enhances surface hardness, resistance to wear, corrosion and cavitation erosion, useful in engineering applications. Processing conditions for obtaining specified structure, melt depth, micro and macro hardness have been determined and structure–property correlations have been drawn from this investigation. Pulsed Nd–YAG laser has been successfully applied in laser surface treatment of ductile iron and compared with processing by CO_2 CW laser.

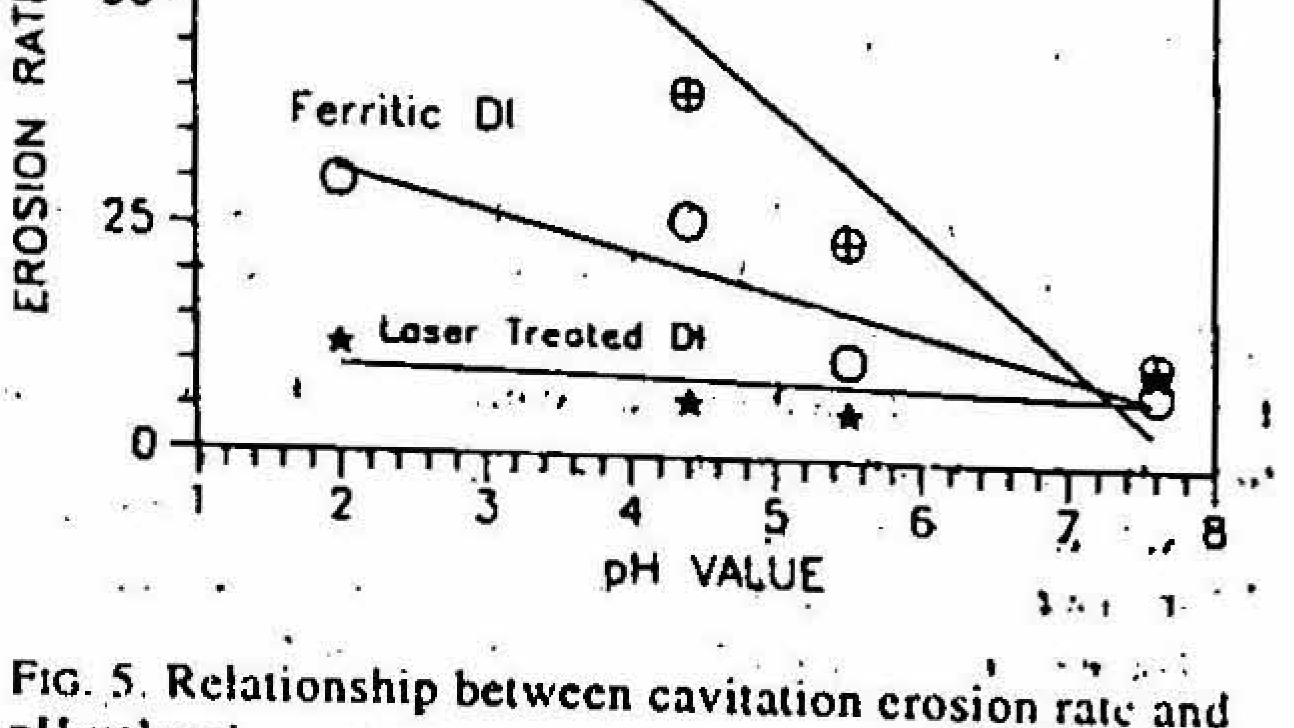

FIG. 5. Relationship between cavitation erosion rate and pH value.

References

1. SINGH, H. B., *et al.*	Fatigue resistance of laser heat-treated 1045 carbon steel, *Metal. Trans. A*, 1981, **12**, 138–140.
2. BLARASON, A., *et al.*	Development of a laser surface melting process for improvement of the wear resistance of grey cast iron, *Wear*, 1983, **86**, 313–325.
3. BERGMANN, H. W.	Current status of laser melting of cast iron, *Surface Engng*, 1985, **1**, 137–155.
4. TOMLINSON, W. J. AND TALKS, M. G.	Cavitation erosion of laser surface melted phosphoric grey irons, *Wear*, 1989, **129**, 215–222.
5. RAWERS, J., *et al.*	Surface and corrosion study of laser-processed zirconium alloys, *Corrosion*, 1991, **47**, 769–777.

Thesis Abstract (M.Sc. (Engng))

Development of parallel algorithms for power system transients by Asha Nataraj

Research supervisors: K. Parthasarathy and D. Thukaram

Department: Electrical Engineering

1. Introduction

The design of robust EHV/UHV AC/DC power system for its economic and reliable operation requires an accurate predetermination of overvoltage/overcurrent magnitudes and waveshapes. The causes for these are varied and many, *viz.*, switching operations, faults, lightning surges and other various intended or unintended disturbances (transitory in nature). These play a vital role in determining the basic insulation level (for proper insulation coordination) of the system and accordingly deciding proper protection schemes.

The estimation of the maximum overvoltage/overcurrent experienced in a system is a very slow and tedious process. It involves an exhaustive study of the system, subject to various disturbances. Added to this are factors such as sensitivity of these transients to various system parameters, adoption of more sophisticated techniques for the study, incorporation of more detailed modelling of the system components, complexity of the system network and the time span of each study[1].

Real-time security operations and control of power systems due to certain problems relating to transients and speeding up of planning and design process emphasise the need for real-time simulation of transients phenomena. Currently, real-time simulation of transient analysis is fulfilled by transient network analysers (TNA) and HVDC simulators which rely largely on reduced scale modelling of system components. Though economical and suitable for certain problems, it suffers from physical and technical limitations, *viz.*, inflexibility in system size representation, inaccurate simulation of lightly damped transients, time to set up system models, etc[2,3]. Under these circumstances, intense efforts are under way to develop reliable and economic alternatives to TNA.

Digital simulation of electromagnetic transients phenomena of power systems, with reliable mathematical models and solution techniques, has been extremely popular due to flexibility and versatility in the simulation process[4]. This simulation is however done offline since computation time of an event turns out to be many times longer than the actual event time. In recent years, much attention has been focussed on the methods of faster and more efficient techniques.

Cost-effective powerful computers of high processing speed and performance are required for the purpose. As the device switching speed approaches a limit, the required processing speed can only be obtained through simultaneous, identical or different operations on a number of operands, processes or jobs. Rapid advances in VLSI technology, substantial reduction in the chip cost, and easy availability of parallel computers commercially has made the application of parallel processing technique the most rewarding alternative. Further, abundant inherent parallelism in the sequential context of the transient solution forms an attractive basis for development of efficient parallel algorithms.

One of the approaches towards parallel processing has been multiprocessing using multiple instruction multiple data (MIMD) machines. The approach involves computation of sections of independent instructions on different processors. This technique has been employed as a test-bed for evaluating the performance of the parallel algorithms developed. Great speed gains have been obtained using this technique although some limitations remain, looking at the entire problem globally involving both MIMD machine and the problem under study.

Electromagnetic transient analysis involves the evaluation of the node voltages and line currents of the system, which is subjected to various disturbances. The simulation, based on time domain formulation, is highly amenable to parallel processing. The problem can be seen as a set of differential equations, which by the application of discretisation method, such as trapezoidal rule, is transformed into a unique algebraic problem at each time step. The number of time steps for which the simulation has to be carried out depends on the time step width and the type of disturbance under study.

Nowhere are the potential pay-offs from parallel processing greater than for solution of transient analysis described by differential equations. The parallel solution of linear algebraic equations reduces the solution time by permitting faster solutions within each time step. Even greater gains are possible by looking at the entire problems globally and achieving parallelism in the computation of the past history terms of all the system components by thorough consideration of all plausible options to provide optimum performance of the EMTP on shared MIMD system.

2. Objectives of the work

The main objective of this work has been to exploit the maximum degree of parallelism that the problem offers suitable for MIMD architecture. It discusses all possible independent tasks that can be executed concurrently and a thorough investigation of the best option to be chosen for the given system configuration and the type of disturbance under study. The issues regarding overheads generated due to algorithm, communication, synchronisation and also computation/communication ratio to obtain optimum performance of the algorithm have been examined.

3. System modelling

The algorithm developed for transient analysis has a great deal of flexibility in studying any general power system network configuration rigorously. It provides facilities for modelling lumped and distributed elements. The basic solution methods have been extended to include features to simulate nonlinearities, saturation effect and to start from any nonzero initial conditions. The program can be employed to evaluate all types of transients. Parallelism has been exploited in each of the system components in the computation of its currents, node voltages, etc.

Further modelling and parallelisation of advanced power system components have been considered. These include incorporation of:

(i) Frequency dependency of long transmission lines using Fourier transforms[4].

(ii) Detailed synchronous machine modelling to study machine dynamics under transient conditions.

(iii) Zinc oxide gapless lightning arrester (which has highly nonlinear characteristics).

Table I
Speed up *vs* no of processors

Electromagnetic transients program					
		No of processors			
		1	2	3	4
Without frequency	Inverse	1.00	1.84	2.55	3.1
Dependency	Lu	1.00	1.72	2.18	2.65
With frequency	Inverse	1.00	1.7	2.4	2.95
Dependency	Lu	1.00	1.6	2.0	2.45

4. Parallel algorithms and solution techniques

Parallelism has also been exploited in the computation of precalculated weighting functions using inverse modified discrete Fourier transforms (IMDFT) and inverse fast Fourier transforms (IFFT).

Compensation method has been adopted to incorporate the nonlinear characteristics of the arrester. This results in an iterative process within each time step. Concurrency existing in this technique has been investigated.

The effect of different solution techniques, *i.e.*, LU decomposition, inverse and its variants (with sparsity consideration) on the performance of the parallel algorithm with varying number of processors has also been examined.

The parallel algorithm developed has been successfully implemented on MULTIMICRO multiprocessor system developed at the Department. This system belongs to tightly coupled MIMD class of parallel architectures.

5. System studies and results

The systems considered for evaluation of the transients and the performance factors (speed up and efficiency) of the algorithm were a typical 400 KV equivalent practical Indian Power System network comprising 34 nodes. The performance of the parallel algorithm for electromagnetic transient analysis as a whole has been very encouraging (Fig. 1) with speed up of 3.1 for four processors (Table I).

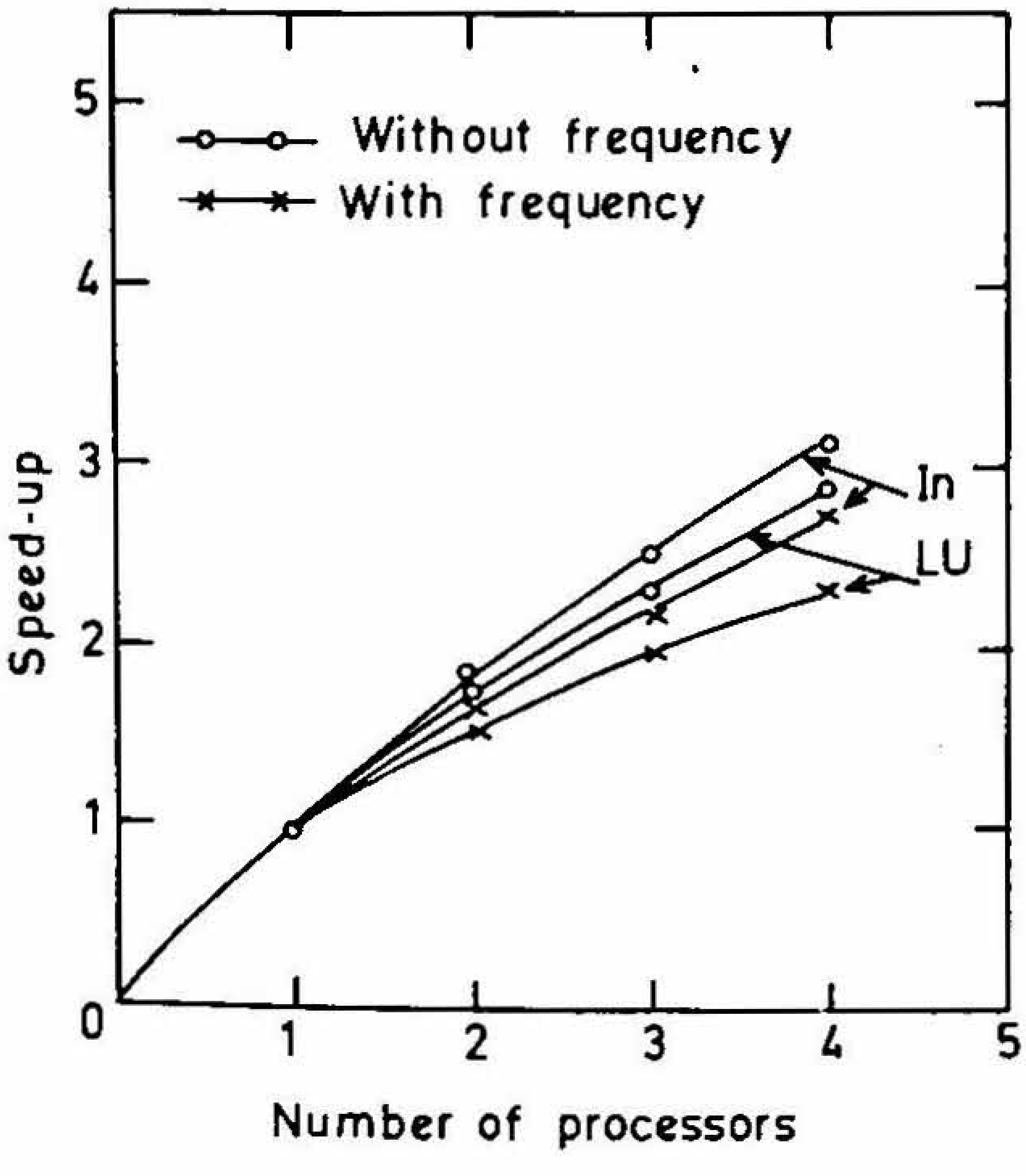

FIG. 1. Electromagnetic transients program.

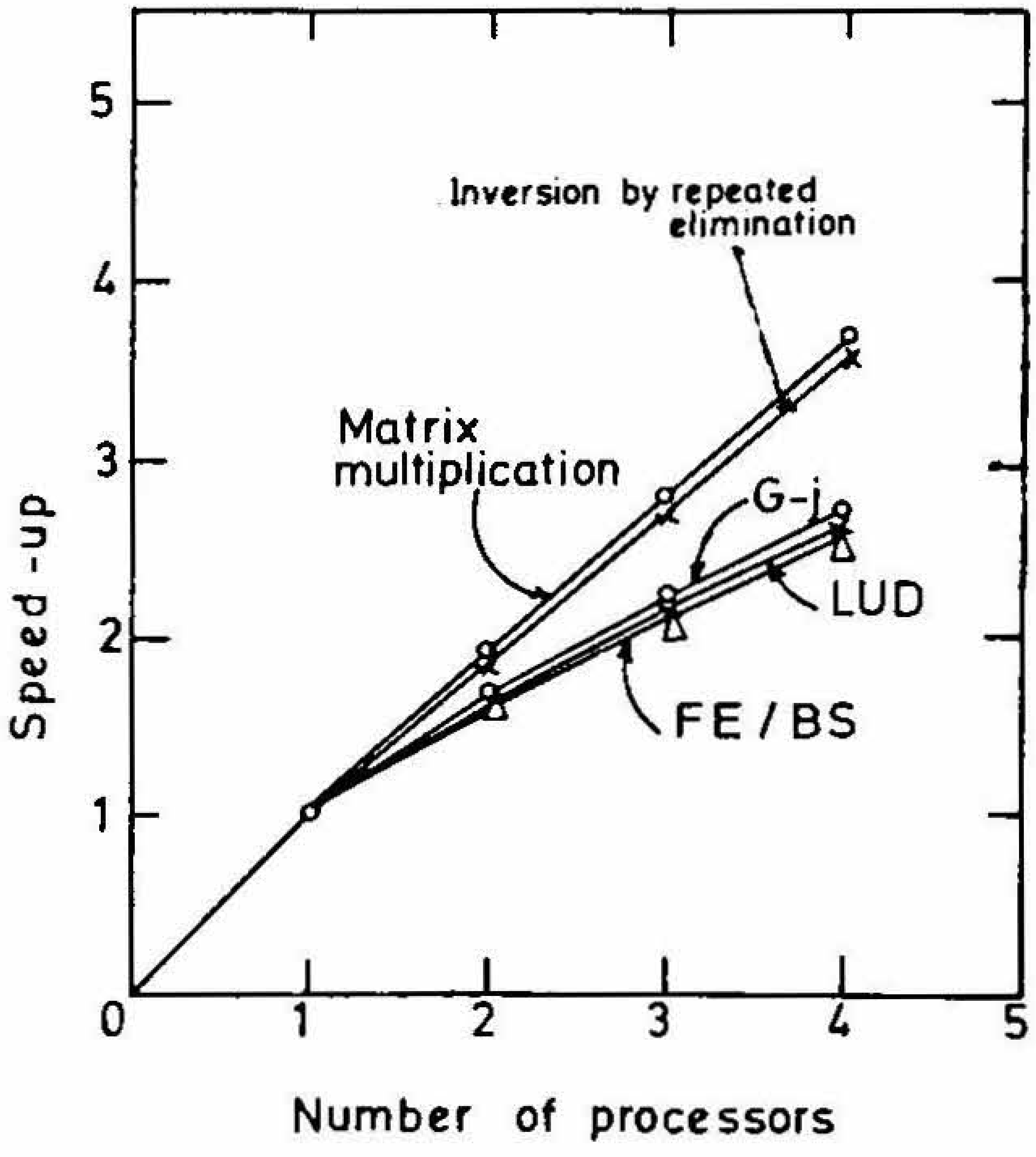

FIG. 2. Solution techniques.

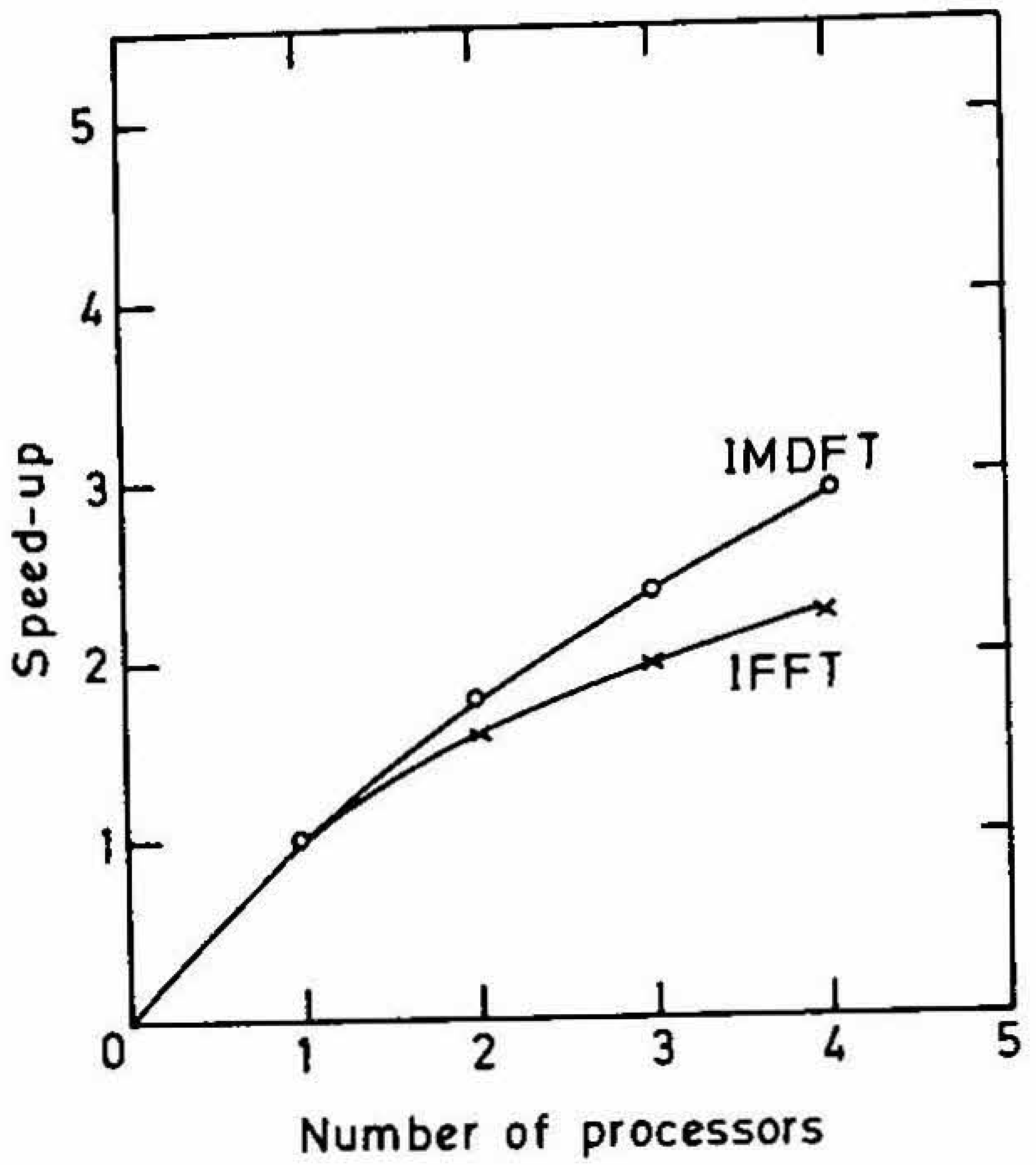

FIG. 3. Weighting functions.

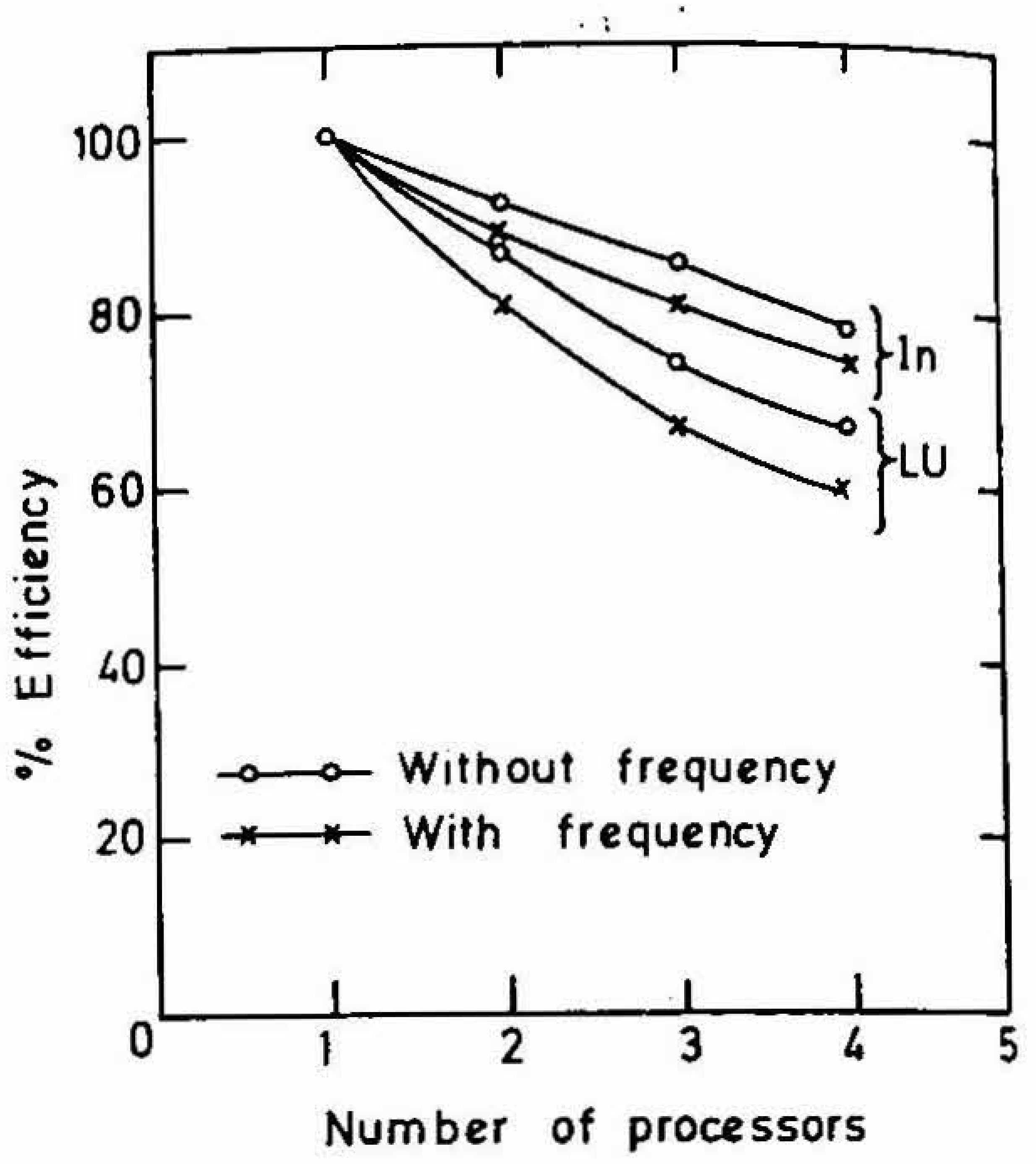

FIG. 4. Electromagnetic transient program.

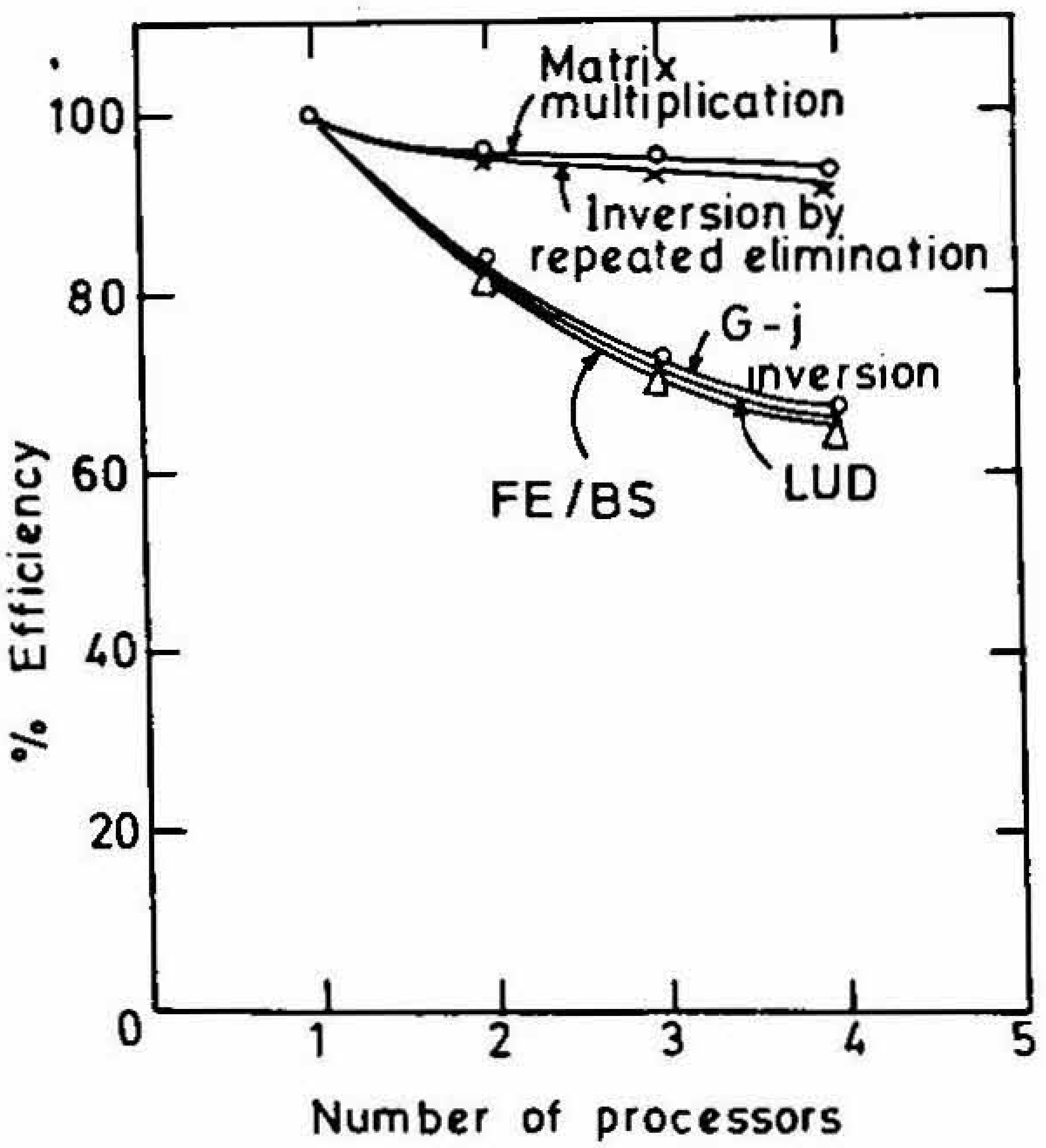

FIG. 5. Solution techniques.

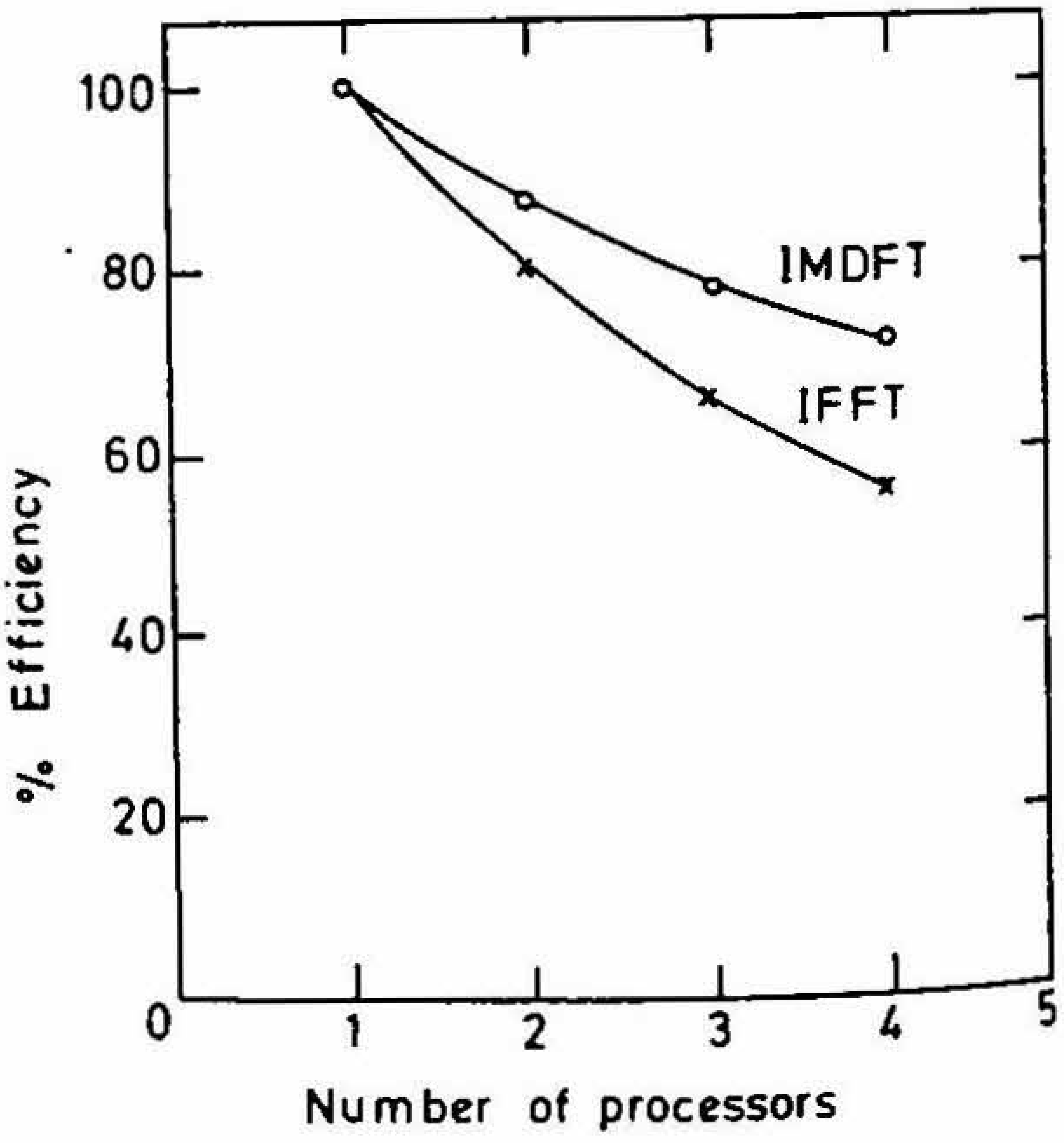

FIG. 6. Weighting functions.

Coming to the effect of solution technique on the performance of the algorithm as a whole, the results indicate that inversion with repeated elimination is better suited for parallel processing compared to LU decom position and conventional inverse methods because of the near linear speed ups exhibited by them and also of matrix-vector multiplication which has to be carried out at every time step.

The study results indicate that computation of weighting function using IMDFT is better suited for parallelisation since its performance is relatively good and also it helps in accurate representation of variation of line parameters with frequency. The speed up for the above are shown in Figs 1–6.

6. Conclusions

The performance of parallel algorithms for electromagnetic transient analysis with MIMD architecture shows that real-time simulation is possible by simple upgradation of processor and bus technologies.

References

1. DOMMEL, H. W.	Nonlinear and time-varying elements in digital simulation of electromagnetic transients, *IEEE Trans.*, 1971, **PAS-90**, 2561–2567.
2. DOMMEL, H. W. AND MEYER, S. W.	Computation of electromagnetic transients, *Proc. IEEE*, 1974, **62**, 983–993.
3. DOMMEL, H. W.	Digital computer solution of electromagnetic transients in single and multiphase networks, *IEEE Trans.*, 1969, **PAS-88**, 388–399.
4.	*IEEE tutorial course; Digital simulation of electrical transient phenomena*, Sponsored by IEEE Power Engineering Society, 1980.
5. DOMMEL, H. W. AND MEYER, S. W.	Numerical modelling of frequency-dependent transmission-line parameters in an electromagnetic transients program, *IEEE Trans.*, 1974, **PAS-93**, 1401–1409.

Thesis Abstract (M.Sc. (Engng))

Analysis and control of an omni-directional platform by Sunil Joseph

Research supervisor: Ashitava Ghosal
Department: Mechanical Engineering

1. Introduction

This work deals with the analysis, design, fabrication and testing of a three-wheeled omni-directional platform.

An omni-directional platform is based on the concept of an omni-directional wheel (Fig. 1) which, unlike a one-degree-of-freedom wheel, has two degrees of freedom[1,2]. An omni-wheel has barrels on its periphery which can freely rotate about an axis perpendicular to the axis of rotation of the wheel itself. Thus the wheel can rotate about its axis and can also 'slide' in a direction along the axis of rotation. There are several advantages of a mobile platform based on such wheels, the main one being high manoeuverability. Unlike a platform based on regular wheels, a mobile platform with omni-wheels has, theoretically, a zero turning radius.

2. Kinematics and dynamics

Figure 2 shows an omni-directional platform having three omni-wheels, of the wheel, $\theta_i, i = 1, 2, 3$ to the linear and angular velocity of the platform, v_1, v_2, $\dot{\psi}$ of the platform. With the assumption of *no slip*, between the wheel and the ground, we can write[3],

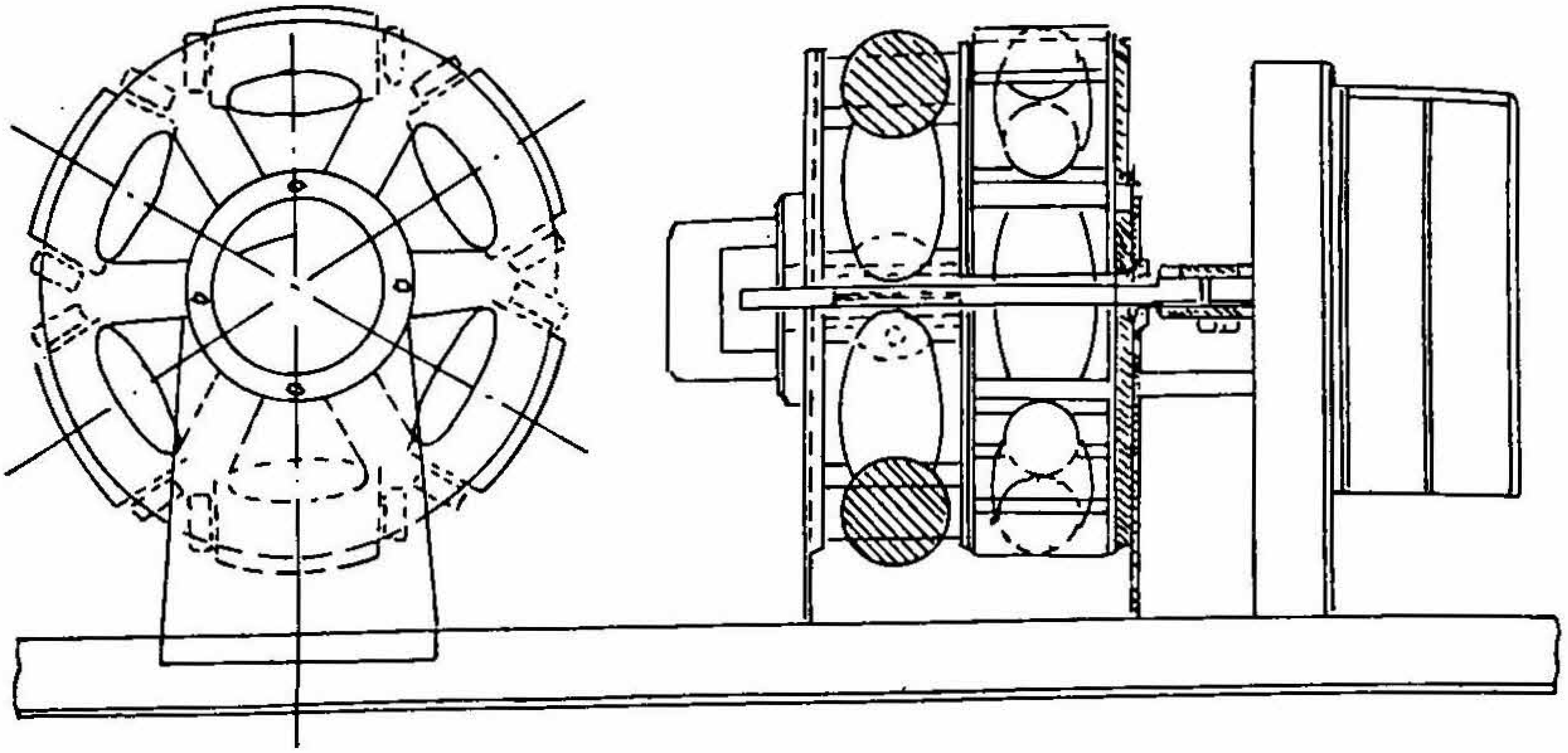

FIG. 1. Assembly drawing of WMR.

$$\begin{bmatrix}\dot{\theta}_1\\ \dot{\theta}_2\\ \dot{\theta}_3\end{bmatrix}=\frac{1}{r}\begin{bmatrix}0 & 1 & R_1\\ -\frac{\sqrt{3}}{2} & -\frac{1}{2} & R_2\\ \frac{\sqrt{3}}{2} & -\frac{1}{2} & R_3\end{bmatrix}\begin{bmatrix}v_1\\ v_2\\ \dot{\psi}\end{bmatrix}=[R]\begin{bmatrix}v_1\\ v_2\\ \dot{\psi}\end{bmatrix} \tag{1}$$

where r is the radius of the wheel, and R_i, $i = 1, 2, 3$, is the distance of the wheels from the centre of the platform. One can also obtain a relationship, $\dot{\sigma} = [S]V$ where $\dot{\sigma}$ is the vector $(\dot{\sigma}_1, \dot{\sigma}_2, \dot{\sigma}_3)^T$ of the sliding velocities and V denotes $(v_1, v_2, \dot{\psi})^T$. We can make the following observation from the above two relationships:

1) The platform has three degrees of freedom denoted by v_1, v_2 and $\dot{\psi}$. The six variables in $\dot{\theta}$ and $\dot{\sigma}$ are related to v_1, v_2 and $\dot{\psi}$ and are not all independent. They are constrained by the relation $\dot{\sigma} = [S]\,[R]^{-1}\dot{\theta}$.

2) The matrix $[R]$ is invertible and V can be written in terms of $\dot{\theta}$. This also implies that the motion of the platform can be controlled by controlling the wheel rotations. Further, the matrix $[S]$ is singular and hence V cannot be obtained from $\dot{\sigma}$. This also implies that the sliding motion of the platform cannot be controlled.

The omni-directional platform is a non-holonomic system and the dynamics equations of motion were derived using the Gibb's Apples[4] formulation. The equations of motion can be written as:

$$[R]^T\begin{bmatrix}\Gamma_1\\ \Gamma_2\\ \Gamma_3\end{bmatrix}=M\begin{bmatrix}\dot{v}_1\\ \dot{v}_2\\ \ddot{\psi}\end{bmatrix}+\dot{\psi}[Q]\begin{bmatrix}\dot{v}_1\\ \dot{v}_2\\ \dot{v}_3\end{bmatrix}$$

where $(\Gamma_1, \Gamma_2, \Gamma_3)^T$ are the torques at the wheels, and $[M]$ is a positive definite matrix and $[Q]$, a skew symmetric matrix.

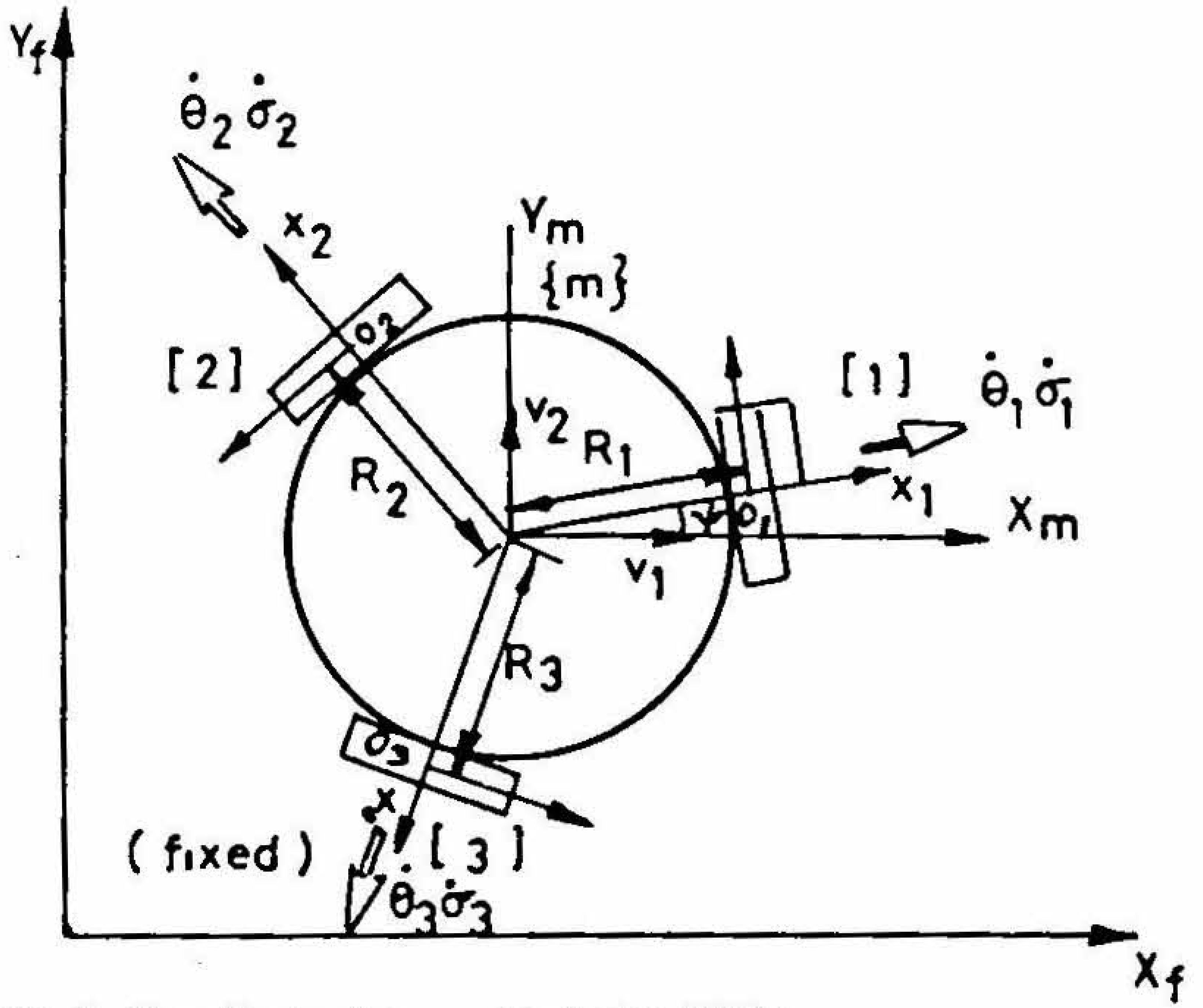

FIG. 2. Coordinates frames attached to WMR.

3. Design and fabrication

Three omni-wheels were designed and fabricated. On the periphery of the wheel, there are six barrels. The radius of curvature of each wheel is 10 cm. Since the radius of both the curvature and the wheel are the same, the barrels touch the ground with point contact, unlike the line contact in conventional wheels. The barrels are free to rotate on shafts which are fixed to the spokes of the wheel. This arrangement allows the wheel to rotate about its axis and also to slide along the same axis, thereby allowing the wheel to have two degrees of freedom.

As the barrels have to be supported at the ends, there are some regions on the periphery of the wheel where there are no barrels. To obviate this problem, two layers with angular separation of 30° were used in the design. This ensures that at least one barrel is always in contact with the ground. Figure 1 shows an engineering drawing of the omni-directional wheel.

The barrels were made of polypropylene by using a special form tool. The form tool was used to ensure a radius of curvature of 10 cm of the barrel. The barrels were covered with rubber tubes to prevent slip in the direction of wheel rotation. The entire platform was designed to carry a load of 100 kg. In the worst case, one barrel in each wheel will be in contact with the ground and hence will be able to bear a third in mind. The shaft was made of mild steel and has a diameter of 0.8 cm. It was observed that the friction between the mild steel shaft and polypropylene was negligible, and the performance was satisfactory.

The three wheels are driven by three independent DC servo-motors (the barrels are not actuated and can rotate freely). A digital control system has been designed and implemented to drive the motors. The angular rotations of the motors are measured by 500 pulse encoders. The errors and the rate of change of errors between the desired and measured (estimated) motor rotations and the speeds are then used to compute the pulse width of a PWM amplifier, thereby varying the input voltage to the motor. This is done according to the familiar PID control algorithm.

The control algorithm is written in assembly language and runs on an 8086/8087 processor. The desired motion commands, based on kinematics, are computed on a PC/AT and then downloaded using a serial link. The measured rotations of the motor are also saved on the 8086/8087 processor system and then transferred to the PC/AT for analysis and display.

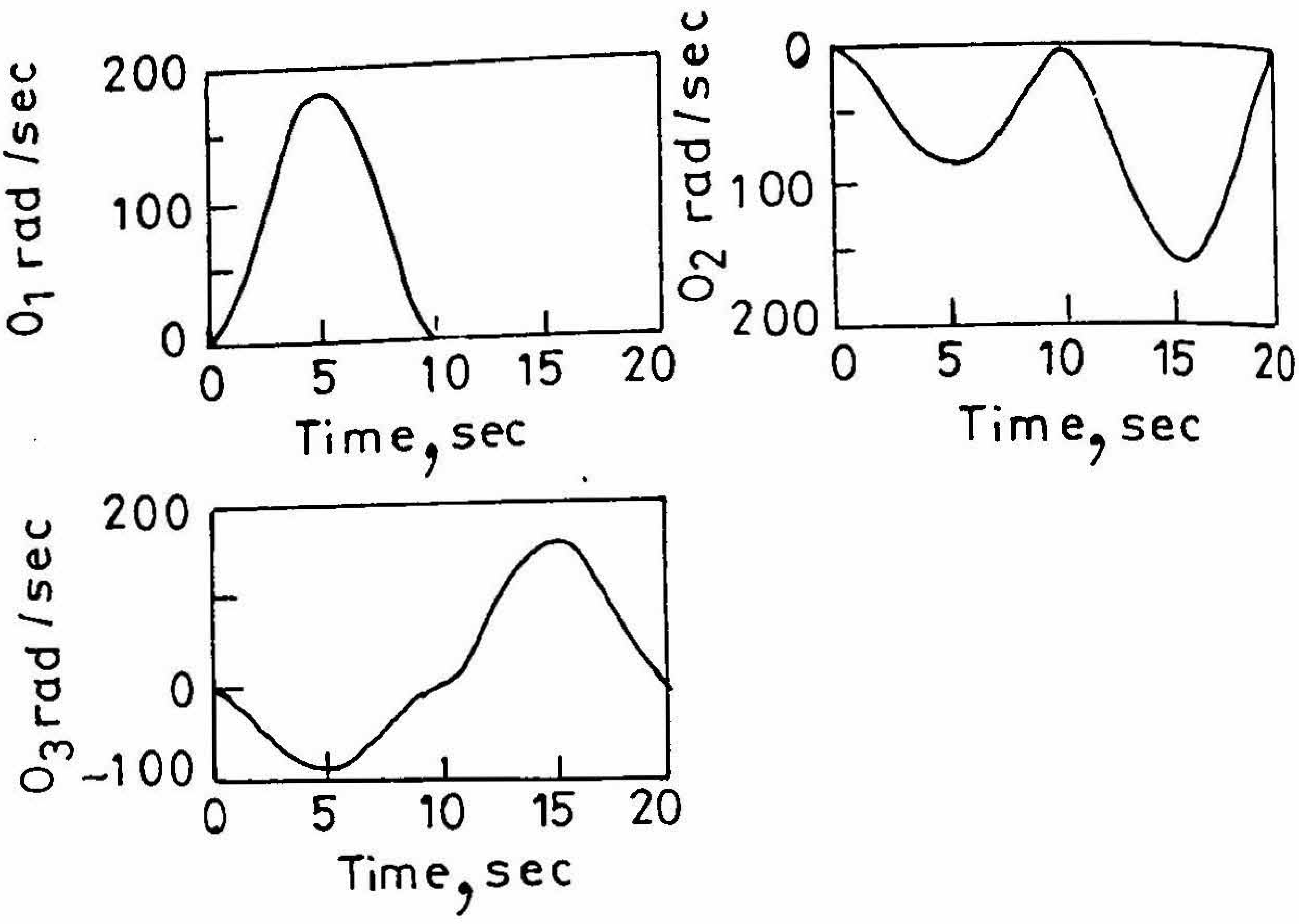

FIG. 3. Right-angle turn simulation.

Table I
Results

Sl no.	Target	K_p	K_d	K_i	Risetime (ms)	Overshoot
1	500	65	15	.1	160	10
2	500	55	25	.1	180	5
3	500	75	10	.1	150	25
4	250	65	10	.1	100	14
5	250	70	25	.1	80	10
6	250	75	15	.1	79	2
7	120	85	10	.1	60	10
8	120	65	25	.1	100	–5

4. Simulation and testing

The omni-directional platform can execute motions such as right-angled turn or rotate about a point. The desired values of the wheel angular velocities can be derived from the kinematic equation (1). Figure 3 shows the plot of angular velocities of the wheels as a function of time for the right-angled turn.

Partial testing of this entire system was carried out. Table I shows the performance of the control system in achieving desired rotations of the wheel.

References

1. Alexander, J. C. and Maddocks, J. H.	On the kinematics of wheeled mobile robots. In *Autonomous robot vehicles* (J. Cox, ed.), pp. 4–25, 1990, Springer Verlag.
2. Muir, P. F. and Neuman, C. P.	*Kinematics of wheeled mobile robots*, Technical Report, CMU-RI-TR86-12, pp. 1–128.
3. Augollo, J., Cardona, S. and Vivancos, J.	Kinematics of vehicles with directionally sliding wheels, *Mech. Mach. Theory*, 1987, 22, 295–300.
4. Augollo, J., Cardona, S. and Vivancos, J.	Dynamics of vehicles with directionally sliding wheels, *Mech. Mach. Theory*, 1989, 24, 53–60.

Thesis Abstract (M.Sc. (Engng))

Experimental studies on friction angle between soils and construction materials by R. G. Robinson

Research supervisors: M. M. Allam and K. S. Subba Rao

Department: Civil Engineering

1. Introduction

Friction between soils and structures, usually expressed in terms of a coefficient of friction (μ) of friction angle (δ), is an important parameter in the design of a variety of geotechnical structures like pile foundations, retaining walls, reinforced earth, foundations subjected to horizontal thrust, etc. Thus underestimation of friction causes an error on the unsafe side in case of the negative skin-friction problem. A reliable estimation of skin friction between soils and structures thus becomes important.

The present-day method is to fix arbitrarily a value for (δ) as a fraction of the angle of internal friction (ϕ), purely based on material roughness. That the friction is dependent not only on material roughness but also on soil particle characteristics has been recently demonstrated[1,3]. This work is an attempt to further strengthen that concept and to enable a rational assessment of interface friction. A parameter, normalized roughness (R_n), as suggested by Kishida and Uesugi[1] was used in this work.

2. Materials and methods

The conventional direct shear apparatus was modified and used to determine the friction angle between soils and plates representing materials of different surface roughness. Two series of tests were carried out, one with the soil moving over the plate (soil-over-plate tests) and the other with the plate moving over the soil (plate-over-soil tests). Sands of different size (D_{50} varying from 0.036 to 2.20 mm) and uniformity coefficient (C_u ranging from 1.3 to 8.3) and silt have been used with plates of different material (stainless steel, mild steel and mortar surfaces) of different surface roughness. The raining technique was used for preparing sand samples. The tests were carried out under two normal stresses of 0.7 kg/cm^2 and 1.4 kg/cm^2 at a strain rate of 0.25 mm/min.

3. Results and discussion

The test results of soil-over-plate tests show that the coefficient of friction μ or (δ/ϕ) is found to exhibit a hyperbolic relationship in the normalized roughness (R_n). A relationship in the form of $(\delta/\phi) = f(R_n)$ more comprehensively descirbes the skin friction between soils and construction materials whereas studying $\mu = f(Rn)$ limits its utility for a particular state of the soil. The relationship between (δ/ϕ) and R is found to be independent of soil density and gradation.

Analysis of test results from plate-over-soil tests shows that for rough interfaces (higher Rn values), the values (δ/ϕ) from the plate-over-soil case are as much as 30% lower than those obtained from the soil-over-plate case; whereas for smooth interfaces (lesser R_n values) both the values are the same. It was also found that the residual coefficient of friction μ_r obtained from soil-over-plate case is practically the same as the μ values corresponding to the plate-over-soil case. Thus the effect of moving the plate over the soil is to remove the dilation component of friction angle.

4. Conclusions

1. In the soil-over-plate-case,

(*a*) The relation between (δ/ϕ) and R_n follows a rectangular hyperbola,

$$(\delta / \phi) = \left[\frac{R_n}{A + BR_n}\right]$$

where, $A = 9.75 \times 10^{-3}$ and $B = 1.04$.

(*b*) The residual coefficient of friction follows the relation,

$$\mu_r\left[\frac{R_n}{a_r + b_r R_n}\right]$$

where $a_r = 8.51 \times 10^{-3}$ and $b_r = 1.444$.

2. The (δ/ϕ) from plate-over-soil case also follows a hyperbolic relationship R_n as,

$$(\delta / \phi) = \left[\frac{R_n}{A' + B' R_n}\right]$$

where $A' = 6.83 \times 10^{-3}$ and $B' = 1.368$.

References

1. KISHIDA, H. AND UESUGI, M. Tests on the interface between sand steel in the simple shear apparatus, *Geotechnique*, 1987, **37**, 45–52.

2. UESUGI, M. AND KISHIDA, H. Frictional resistance at yield between dry sand mild steel. *Soils Found.*, 1986, **26**, 139–149.

3. UESUGI, M., KISHIDA, H. AND UCHIKAWA, Y. Friction between dry sand and concrete under monotonic and repeated loading, *Soils Found.*, 1990, **30**, 115–128.

Thesis Abstract (M.Sc. (Engng))

Al_2O_3/Al Composites from Al–Zn alloys: Growth and infiltration mechanisms by

H. R. Muralidhar
Research supervisor: Vikram Jayaram
Department: Metallurgy

1. Introduction

Limitations of the conventional processing routes to fabricate ceramic matrix composite components like the stability of the reinforcements and matrix materials at the processing temperature, cost, size of the component, etc., have been overcome by the development of a novel technique called directed melt oxidation (DIMOX)[1,2]. The attractiveness here comes from the fact that this is a comparatively low-temperature process utilizing no external pressure and that near net shapes can be made in an one-step operation. The key to this process is the high temperature oxidation of molten alloys to form a composite microstructure of interconnected ceramic oxide and metal. Preformed porous ceramic bodies can be infiltrated by this composite mixture to form dense ceramic matrix composites.

In the case of Al_2O_3-based composites, formed from the oxidation of Al alloys, the alloying element plays the critical role in promoting the growth of the composite. While it is clear that the formation of the passivating aluminium oxide on the melt surface is suppressed either by the formation of a thermodynamically stable solute oxide or due to the vapour pressure of the solute element, it is not definite which of these two effects play the dominating role in sustaining the growth of the composite[3-5]. It is also believed that the presence of Mg in the Al is a must for composite growth[3]. The present study is divided into two parts. The first part seeks to demonstrate the role of the solute vapour pressure in the growth of the composite by choosing zinc as the alloying element. The nature of infiltration and growth of the composite within in Al_2O_3 particulate preform was investigated in the second part.

2. Results and discussion

2.1. *Growth of Al_2O_3/Al composite from Al–Zn alloys*

The oxidation behaviour of an Al–Zn binary alloy was studied at different holding temperatures and zinc concentrations by TGA. Though the morphology of the surface oxide and growth rates varied at different temperatures, the oxidation behaviour of the alloy is essentially the same. The growth of the composite follows three stages, wherein the initial slow weight gain stage is associated with the formation and thickening of ZnO all over the surface of the melt. The second stage, which is the period of maximum growth rate, is linked to the constant presence of this ZnO on the surface and its contact with Al. During the end of this stage, certain perturbations form on the surface that lead to localized growth. As the third stage is entered, the growth rate falls off. During this stage, the surface was predominantly Al_2O_3 and was devoid of ZnO except at a few localized regions. The growth follows a pattern of cyclic formation and disappearance of ZnO on the surface, which suggests a reaction of the type

$$2Al + 3ZnO = Al_2O_3 + 3Zn$$

wherein the ZnO is contact with Al is not thermodynamically stable and gets reduced to form Al_2O_3 and the Zn released from the reaction vaporizes and forms ZnO on the surface only to be reduced again by the melt. Thus the growth of the composite is sustained by this cyclic reduction and formation of ZnO on the surface and the oxygen supply for the aluminium oxidation is maintained by this reaction and not by the direct interaction of Al with the atmosphere.

Increase in temperature and Zn concentration and small additions of Mg to the binary Al–Zn alloy prolongs the period of maximum growth rate.

2.2. *Infiltration of Al_2O_3/Al composite into an Al_2O_3 preform*

The exact nature of infiltration and growth of an Al_2O_3/Al composite into an inert preform was studied by keeping Al_2O_3/ particulate preform in contact with an Al–Zn alloy melt surface at 1050°C. It was observed that the growth rate through a preform is higher than that for plain composite growth due to the extra surfaces now available for oxidation. Uninfiltrated regions of the preform above the growth front revealed the presence of ZnO in the form of a coating on the Al_2O_3 particles and the Al_2O_3 from the reaction was in contact with and crystallographically epitaxial with the preform particle. This suggests that the Zn vapour oxidizes on the Al_2O_3 particle to form a ZnO coating and the metal climbs up the particle surface by reacting with the ZnO, which is governed by the negative change in interfacial free energy for the reaction Al + ZnO. The growth of the composite takes place from the particle surface laterally filling the pore spaces. Non-uniform presence of ZnO in the preform leads to some regions being uninfiltrated.

3. Conclusions

This study has demonstrated that composites can be grown from an Al–Zn binary alloy and that Mg is not essential for sustaining the growth. The importance of the solute vapour pressure and its wettability by the melt in controlling the growth of the composite is also realized.

Growth rate of the composite within a preform is much higher than that for plain composite growth. The filtration of the metal is by a process of reaction-induced wetting and the growth of the composite takes place essentially from the particle surface.

References

1. NEWKIRK, M. S., URQUHART, A. W. AND ZWICKER, H. R. *J. Mater. Res.*, 1986, **1**, 81–89.
2. NEWKIRK, M. S., *et al.* *Ceram. Engng Sci. Proc.*, 1987, **8**, 879–882.
3. SINDEL, M., TRAVITZKY, N. A. AND CLAUSSEN, N. *J. Am. Ceram. Soc.*, 1990, **73**, 2615–2618.
4. NAGELBERG, A. S. *Solid St. Ionics*, 1989, **32/33**, 783–788.
5. SALAS, O., *et al.* *J. Mater. Res.*, 1991, **6**, 64–81.

Thesis Abstract (M.Sc. (Engng))

Selective flotation of serpentine from magnesite by G. Srinivasa Rao

Research supervisors: U. B. Nayak and R. M. Mallya
Department: Metallurgy

1. Introduction

Magnesite is an important raw material for the manufacture of basic refractories. Since the manufacture of magnesia from sea water is a very capital-intensive process and also since it requires limestone and dolomite of high purity having very low silica content which are relatively scarce, users still prefer natural magnesite for refractory applications[1]. Good-quality natural magnesite is also scarce in India. Indian magnesite contains considerable amounts of silica and fluxing agents. Some of the Indian magnesite deposits of siliceous variety contain silica in the form of serpentine, that too, in a finely disseminated form, thus making them more complex for upgradation. The separation of magnesite from serpentine is difficult owing to its similar surface characteristics as well as chemical and electrokinetic properties. The problem is further complicated by the influence of dissolved mineral species on the flotation properties of each other.

In the light of the above, the present work was aimed to carry out some fundamental studies on pure serpentine and magnesite using a modified Hallimond tube to understand the flotation behaviour of these two minerals with a cationic collector. Flotation experiments were conducted using *n*-dodecylammonium chloride as a collector reagent with a view to float serpentine away from magnesite.

2. Experimental materials and methods

Hand-picked pure variety of serpentine and magnesite were taken and analyzed chemically as well as mineralogically. Both the minerals were ground individually in a porcelain ball mill and the material was sieved to get a required size. Flotation studies were carried out with –200 + 300 # size fraction material whereas zeta potential studies were conducted with –400 # materials[3,4].

To carry out flotation experiments, a modified Hallimond tube microflotation set up was fabricated and assembled. Zeta potential studies were made using a zeta-meter system 3.0, commercially available electrophoresis apparatus.

3. Results and discussion

Based on the flotation recoveries obtained at different pH values for different collector concentrations, the important process parameters, *viz.*, pH and collector concentration were optimized at 10.0 and 2.71×10^{-4} M, respectively. The variation of zeta potential with pH has indicated the point of zero charge for serpentine as 5.8 and for magnesite as 7.8. From the zeta potential studies and flotation recoveries under optimum conditions, it was concluded that the collector mechanism involved in both the systems, *i.e.*, dodecylamine-serpentine and dodecylamine-magnesite, is an electrostatic adsorption between negatively charged mineral surface and positively charged aminium ions. The lower flotation recoveries of serpentine in the presence of magnesium chloride and magnesite supernatants have indicated the influence of magnesium ions on serpentine flotation by decreasing its flotation recoveries. This could be due to the limited availability of negative mineral surface for the adsorption of aminium collector ions. To enhance the selectivity with respect to flotation between serpentine and magnesite, the effect of different inorganic (sodium silicate, ferrous sulphate, sodium carbonate and sodium hexameta phosphate) and organic (starch) modifiers, individually and in combination, on the flotation of these two minerals was studied. It was found that starch acted as an effective depressant for magnesite without affecting the flotation recoveries of serpentine and it was also found that the depressing effect of starch on magnesite was still more prominent in the presence of sodium carbonate. Serpentine could be selectively floated from magnesite in the presence of sodium carbonate, starch and sodium silicate over a pH range 9.0–10.5. Under optimized monomineralic conditions serpentine could be separated from magnesite from 1:1 synthetic mixture of these two minerals obtaining the selectivity indices varying between 7.18 and 14.5 with a maximum at pH 10.0. These results have indicated the possibility of separation of serpentine from magnesite under the above optimized conditions.

References

1. *Report on beneficiation of magnesite from Salem area, Tamil Nadu, India*, Regional Research Laboratory, Bhubaneswar, 1978.

2. SMITH, R. W. AND TRIVEDI, T. Variation of point of zero charge of oxide minerals as a function of aging time in water, *Trans. AIME*, 1976, 255, 69–74.

3. PREDALI, J. J. AND CASES, J. M. Zeta potential of magnesium carbonates in inorganic electrolytes, *J. Colloid Interface Sci.*, 1973, 45, 449–458.

4. HANNA, H. S. AND SOMASUNDARAN, P. Flotation of salt-type minerals. In *Flotation, A. M. Gaudin Memorial*, Vol. 1, (Fuerstenan, M. C., ed.), 1976, pp. 197–272, AIME.

Thesis Abstract (M.Sc. (Engng))

Multichannel data acquisition system for medium scale metallurgical industries by

K. Ravichandran
Research supervisors: M. V. Lele and K. R. Srinivasan
Department: Instrumentation and Services Unit

1. Introduction

Data acquisition systems play a vital role in providing critical information in various applications involving close monitoring and control of multiple interrelated parameters in process control industries. Heat treatment is one of the important stages in any metallurgical industry, as information and control of the temperature distribution inside heat treatment furnaces has a direct impact on the characteristics of the resultant product. Applications of data acquisition systems vary from simple to complex systems involving physical/electrical parameters.

This work concerns the design and development of a dedicated multichannel data acquisition system for temperature distribution measurement for a class of furnaces commonly used in heat-treatment plants. The design methodologies involving component selection, electrical noise rejection, man–machine interface and suitability to work in industrial environment are the contributions made in this work to ensure higher accuracy and reliability. The total system hardware has been designed using the modular approach as it provides flexibility for easier adaptability to other applications and serviceability. This unit has been made to cover a temperature range of 0–1200°C using a K-type thermocouple. The performance of the system has been tested in a medium-scale metallurgical industry and the results were found to be satisfactory.

2. Overview of the work

Conventional data acquisition (Fig. 1) consists of a multiplexer, analog-to-digital converter signal conditioner and microcomputer.

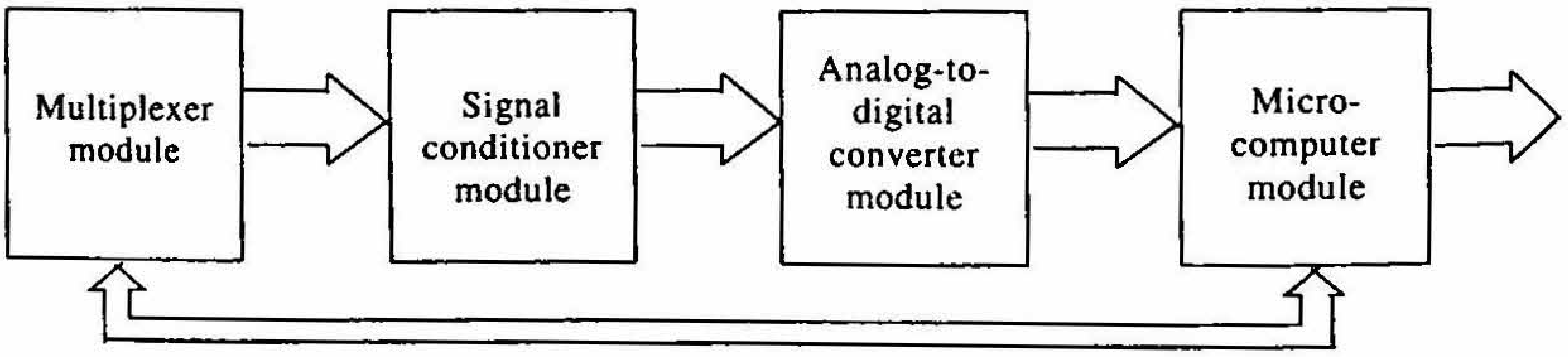

FIG. 1. Block diagram of general data acquisition system.

This unit also contains all the modules of a general DAS. Some of the important features of the selected modules are:

2.1. *Multiplexer module* is based on reed relays as they provide a very low ON resistance and very high OFF resistance. The very low on resistance in a multiplexer is best suited in applications involving thermocouples.

2.2. *Signal conditioner module* utilizes a dedicated special-purpose amplifier incorporation features like ice-point compensation embedded into the integrated circuit suitable for K-type thermocouples.

2.3. *Analog to digital converter.* The digitizer module is based on dual slope analog to digital conversion technique with a resolution of ±one count in 20,000 counts. The dual slope ADC also has an inherent characteristic of rejecting line frequency noise which is prominent in an industrial environment.

2.4. *Microcomputer module* is based on an 8-bit microcomputer with associated peripherals including a real-time clock, battery-powered random access memory to save important data acquisition user-fed data in the case of a power failure. User function selection and associated parameter entry have been achieved through a dedicated keyboard and the information feedback of the same obtained through a display unit.

2.5. *Power supply module*. Special care has been taken in designing the power supply module, which is the primary source of ground loop noise normally associated with analog and digital circuitry, by providing individual onboard regulator for each module and independent common point return to minimize noise and also to avoid spot heating in the system.

2.6. *General*. Considering the industrial environment, the system is provided with surge suppressers, snubber network and industrial-grade components have been used to improve the overall reliability of the system and also to achieve the desired accuracy over the entire industrial temperature range. Engineering practices like humisealing of printed circuit boards after cleaning with isopropyl alcohol to protect against relative humidity variations reflecting on the system performance and accumulation of dust and other foreign particles which may deteriorate the overall performance have been incorporated. After the fabrication of the unit, it was subjected to tests like soak test for 120 h, elevated temperature test, by keeping the unit at 70°C for 48 h, temperature cycling between –25 and 70°C for half an hour at each temperature and found the performance satisfactory. The unit engineering was done keeping in view the easy serviceability and expandability. The printed circuit boards were standardized in such a way that the user can have spare cards to reduce the downtime which is very essential in process control industries.

3. Results

This unit was installed in a medium-scale metallurgical industry, involved in the casting of iron and carrying out heat-treatment operation on the cast material and the performance was found to be satisfactory and reliable.

References

1. *Data acquisition block*, Vol. II: *Module systems*, 1984, Analog Devices.
2. *Linear design seminar*, Oct. 1987.
3. BOSSHART, T. M. *Printed circuit boards: Design and technology*, 1983, Tata McGraw-Hill.
4. BROWN, B. *The handbook of linear IC application*, 1986.
5. *Data logger ups efficiency at ammonia plant*, I&CS, p. 81, May 1983.

Thesis Abstract (Ph.D.)

Studies on transfer RNAs of Cucumber (*Cucumis sativus*) by M. Puttaraju

Research supervisors: C. Jayabaskaran, T. M. Jacob and K. P. Gopinathan
Department: Biochemistry

1. Introduction

Transfer ribonucleic acids (*t*RNAs) are multifunctional macromolecules that play a pivotal role in protein biosynthesis. Besides translating the genetic information, specific *t*RNAs are also involved in various other cellular functions[1]. One of the characteristic structural aspects of *t*RNAs is that a significant portion of the nucleotides are modified. Because of its well-characterized nature and obvious biological importance, the study of *t*RNAs has been of interest ever since its discovery. In the present investigation, we are reporting a systematic study of modified nucleotides and the effect of light on nucleotide modifications of the *t*RNA of the economically important plant, ***Cucumis sativus***. Some preliminary studies on the structure and organization of the *t*RNA genes in this plant are also reported.

2. Results and discussion

Analysis of modified nucleotides of total *t*RNA isolated from cucumber cotyledons by chromatographic, electrophoretic and immunological methods revealed the presence of modified nucleotides such as m^{1}Ap, m^{2}Gp, m^{5}Gp, m^{5}Cp, m^{2}Ap, TP, ψp, Dp, i^{6}Ap, io^{6}Ap and dinucleotides CmpCp, AmpAp, GmpGp, CmpGp/GmpCp, GmpAp/AmpGp, CmpAp/AmpCp and m^{1}AmpUp.

Studies on the incorporation of [^{35}S] label into the *t*RNAs of cucumber cotyledons showed the presence of five species of thionucleotides and they were identified as 5-methylaminomethyl-2-thiouridine (mnm^{5}s^{2}Up), 2-methylthioisopentenyl adenosine (ms^{2}i^{6}A), 2-methylthioribosyl zeatin (ms^{2}io^{6}Ap), 5-methyl-2-thiouridine (m^{5}s^{2}Up) and N[N-(9-β-D-ribofuranosyl-2-methylthiopurine-2-yl) carbamoyl] threonine (ms^{2}t^{6}Ap).

The effect of light on nucleotide modifications was evaluated using cucumber cotyledons grown under light and in complete darkness^2. Transfer RNAs from light-grown tissue had slightly higher levels of 2'-O-methyl dinucleotides. On the other hand, *t*RNA from light-grown cotyledon showed the complete absence of 2-methylguanosine (m^{2}Gp) and a decrease in the relative proportions of ribothymidine (Tp) and the cytokinin active ribonucleosides (i^{6}Ap and io^{6}Ap). The relative amount of mnm^{5}s^{2}Up was more in the light-grown cotyledon *t*RNA whereas it was reverse with respect to m^{5}s^{2}Up. From these results it appears that light has both positive and negative effects on nucleotide modification in cucumber cotyledon *t*RNA.

Cucumber total cytoplasmic *t*RNA on fractionation by 2D-PAGE was resolved into 56 spots; of these 32 have been identified as *t*RNAs corresponding to the 15 amino acids by aminoacylation using both hypocotyl and cotyledon enzymes. There are four isoaccepting *t*RNAs for Leu; three each for Lys and Ser; two each for Ala, Arg, Gly, Ile, Met, Phe, Pro, Thr, Tyr and Val; one each for Asp and His. The *t*RNAs specific for Asn, Gln, Glu and Cys could not be identified due to the instability of the aminoacyl *t*RNA synthetases prepared from both hypocotyls and cotyledons.

In order to determine the primary structure, *t*RNA$^{\text{Leu}}$ was purified to homogeneity by using RPC-5 column chromatography and 2D-PAGE. The complete nucleotide sequence was determined by post-labelling techniques. For this, about 0.5 ug of *t*RNA$^{\text{Leu}}$ was partially hydrolysed with formamide and the fragments were end labelled. The 5'end-labelled fragments were separated on a 15% denaturing gel. Each one of the bands was eluted and hydrolyzed with nuclease PI. The labelled 5'-end nucleotides were analyzed by one-dimensional TLC and the nucleotides were identified by their chromatographic mobilities^3. Like other plant cytoplasmic *t*RNAs$^{\text{Leu}}$, cucumber cytoplasmic *t*RNA$^{\text{Leu}}$ is 87 nucleotide long and could be folded into the classical clover leaf secondary structure with all the invariant and semi-invariant nucleotides at their respective loci. It has a 15-nucleotide-long extra loop and contains 15 minor bases: m^{2}G, m^{5}C, D, acp^{3}U, m_2^2G, m^{1}G, ψ, Um, T and m^{1}A and an unidentified nucleotide N which occurs at the wobble position of the anticodon. The identity of all the modified nucleotides was also confirmed by total base composition analysis.

With a view to understand the structure and organization of *t*RNA genes, a DNA library was prepared in pUC 18 using total cell DNA digested with BamHI. The clones were identified with 3'end-labelled total *t*RNA and a clone pCsB 60 with 1 kb insert DNA was used for further studies. A partial restriction map of the insert was established and the complete nucleotide sequence was determined. Comparison of the sequence obtained with the reported sequences indicated the presence of 3'-half of the *t*RNA$^{\text{Ile}}$ (exon 2) and 5'-half of the *t*RNA$^{\text{Ala}}$ (exon 1) genes. Besides, it showed strong sequence homology to the corresponding 1 kb region of the chloroplast *r*DNA spacer of several higher plants. The presence of two different *t*RNA genes was confirmed by analyzing the hybrid-selected *t*RNAs, and Southern hybridization of EcoRI-digested chloroplast DNA with cloned DNA probe further confirmed that the insert DNA was from the chloroplast.

References

1. Bjork, G. R., Ericson, J. U., Gustafsson, C. E. D., Hagervall, T. G., Jonsson, Y. H. and Wikstrom, P. M. — *A. Rev. Biochem.*, 1987, **56**, 263-287.
2. Puttaraju, M. and Jayabaskaran, C. — *J. Biosci.*, 1988, **13**, 367–378.
3. Nishimura, S., Shindo-Okada, N. and Crain, P. P. — *Methods in enzymology*, 1987, Vol. 155, pp.373–396.

Thesis Abstract (Ph.D.)

Synthetic investigations on n-substituted 4- and 5-nitro-1H-imidazoles by A. K. S. Bhujanga Rao

Research supervisors: K. M. Madyastha and C. Gundu Rao (Reckitt & Colman of India Ltd)
Department: Organic Chemistry

1. Introduction

N-substituted products of 4(5)-nitroimidazoles are of great utility as chemotherapeutic agents. Metronidazole and tinidazole belonging to the 5-nitro series have widely been used in the treatment of protozoal infections like trichomoniasis. The isomeric 4-nitroimidazoles are gaining pharmacological significance as immunosuppressants, aldehyde dehydrogenase inhibitors, radiosensitizers and radiotherapy synergists. In the present work, the synthetic and mechanistic aspects of biologically important 4-nitro and 5-nitroimidazoles have been investigated.

2. Experimental methods

Alkylation and acylation reactions on 4(5)-nitroimidazoles were carried out in acidic and basic media over a range of temperatures. The Michael addition of 4(5)-nitroimidazoles and the base-catalyzed isomerization of 5-nitroimidazoles were studied in a variety of protic and polar aprotic solvents. To investigate the applications of flouride ion to the chemistry of nitroimidazoles, potassium flouride was used in the free anhydrous form and also as a supported reagent KF-Al_2O_3. Halogenation of 4(5)-nitroimidazoles and 1-alkyl-4-nitroimidazoles was carried out employing two new systems Br_2-DMF-$KHCO_3$ and KI-HNO_3-AcoH. Acyl transfer reactions of N-acyl-4-nitroimidazoles were carried out with N- and S-nucleophiles on $CHCl_3$ and THF.

The structure elucidation and unambiguous assignment of orientations were based on solvent-induced ^1H NMR shifts, C NMR and mass spectral fragmentation studies. Computation of isomer ratios was carried out by using HPLC and ^1H NMR.

3. Results and discussion

Alkylations of 4(5)-nitroimidazoles (**1**) were studied in acidic and basic media to synthesize either of the two possible isomers **2** and **3** in high regioselectivity. Alkylation in acidic media with reactive alkylating agents results in the predominant formation of 5-nitro isomers (**2**) at lower temperatures (75°C) and 4-nitro isomers (**3**) at higher temperatures (140°C). With unreactive alkyl halides, only 5-nitro isomers were produced irrespective of the temperature. The mechanism was shown to involve quaternization of the initially formed N-alkyl-5-nitroimidazoles followed by preferential dealkylation to yield thermodynamically more stable 4-nitroimidazoles (Scheme 1). Reactions of **1** with alkyl halides in DMF-K_2CO_3 resulted in very good yields of N-alkyl-4-nitroimidazoles in excellent regioselectivity[1]. Alkylations with propargyl bromide resulted in the formation of N-allenyl-4-nitroimidazoles with DMF-K_2CO_3 and N-propargyl-4-nitroimidazoles with acetone-K_2CO_3[2]. The latter could be isomerized to allenic compounds in KF–MeCN.

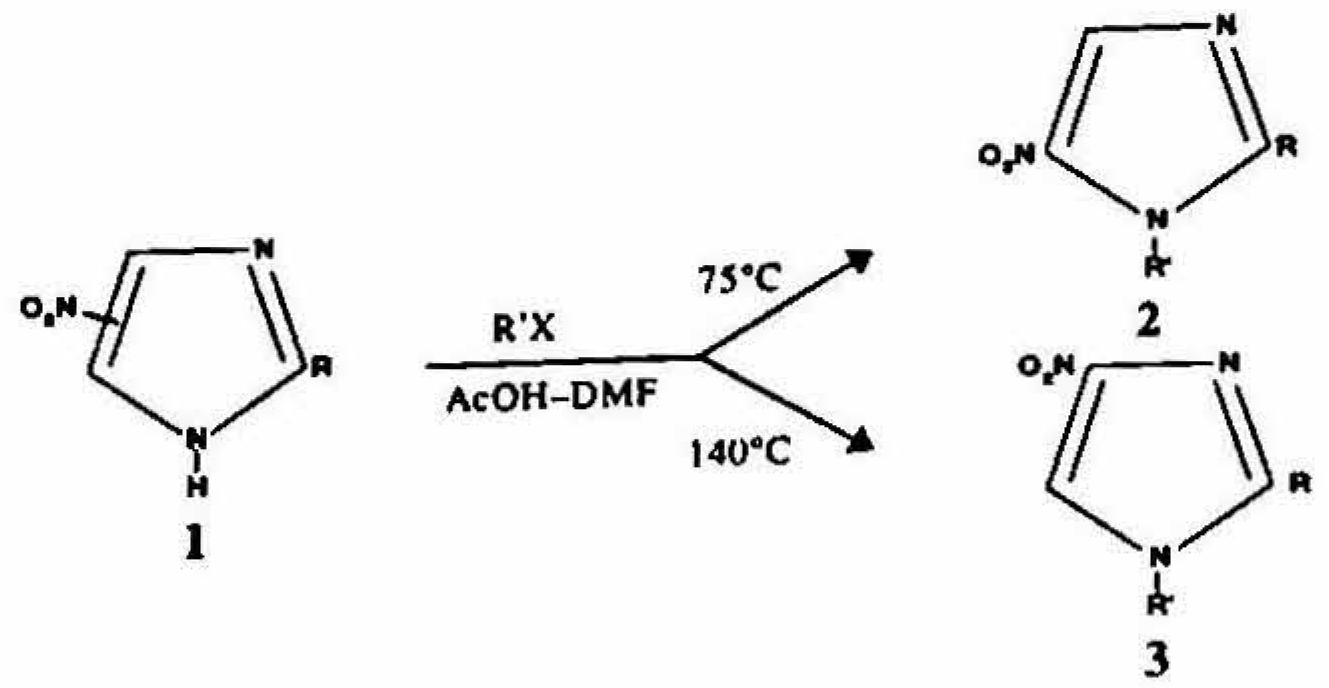

SCHEME 1.

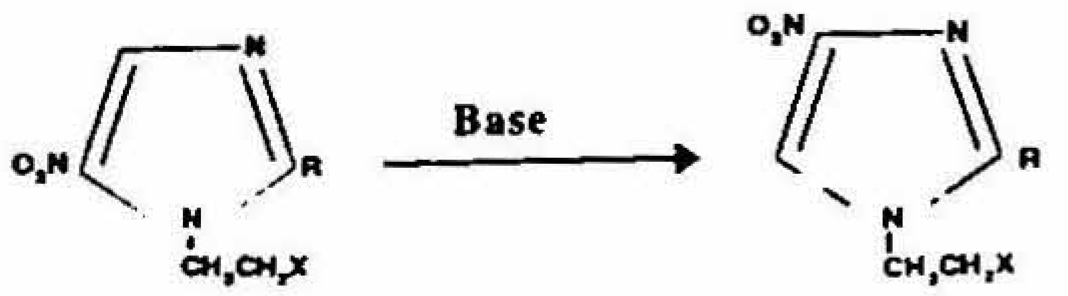

R	X
H	SO$_2$Et
Me	SO$_2$Et, SO$_2$ Bu^n
	SO$_2$Ph, CN

SCHEME 2.

The regiochemistry of addition of 4(5)-nitroimidazoles to Michael acceptors was studied under a variety of conditions employing acidic and basic catalysts. Only 4-nitroimidazoles were isolated under all conditions. The best yields were obtained in DMSO-Py at 135–140°C and the procedure provides a high-yielding method for the synthesis of 4-nitroimidazoles having a functionalized side chain on N$_1$[3]. The method was further improved using anh.KF in MeCN, almost quantitative yields being realized in short durations[4].

The base-catalyzed rearrangement of a group of N-alkyl-5-nitroimidazoles was studied with respect to the nature of the side chain on N$_1$, base strength, concentration of base and temperature (Scheme 2). The mechanism of the isomerization reaction was shown to involve cleavage of the side chain on N$_1$ and realkylation at the more nucleophilic N$_3$ to give thermodynamically more stable 4-nitro isomers[5]. These isomerization reactions were found to be very facile with KF-Al$_2$O$_3$[6]. The synthesis and isolation of very reactive N-acyl-2-methyl-4-nitroimidazoles and their potential application as facile acyl transfer agents were studied[7]. These nitroimidazoles were found to be much better acyl transfer agents than simple N-acyl imidazoles.

A class of pharmacologically important 1,2-dialkyl-4-nitro-5-bromoimidazoles were synthesized from the corresponding 4-nitro analogue employing a new brominating system Br$_2$-DMF-KHCO$_3$[8]. The mild conditions of the reaction allow brominating to be carried out in the presence of acid- and base-sensitive functionalities. Methods for nuclear iodination of 4-nitroimidazoles were investigated. A novel reagent KI-HNO$_3$-AcOH was used for the synthesis of a series of new 1,2-dialkyl-4-nitro-5-iodoimidazoles and 1-alkyl-4-nitro-2,5-diiodoimidazoles with potential radiosensitizing properties[9]. The synthesis of hitherto inaccessible 4(5)-cyclic amino-5(4)-nitroimidazoles was achieved by a two-step sequence from 4-nitro-5-haloimidazoles having cyanoethyl or sulfonylethyl side chains on N$_1$[10].

References

1. BHUJANGA RAO, A. K. S., GUNDU RAO, C. AND SINGH, B. B. *Synth. Commun.*, 1991, **21**, 427–433 and the references cited therein.

2. BHUJANGA RAO, A. K. S., GUNDU RAO, C. AND SINGH, B. B. *J. Chem. Res.* (*S*), 1993, 506–507.

2. BHUJANGA RAO, A. K. S., GUNDU RAO, C. AND SINGH, B. B. — *J. Chem. Res. (S)*, 1993, 506–507.
3. BHUJANGA RAO, A. K. S., GUNDU RAO, C. AND SINGH, B. B. — *J. Org. Chem.*, 1990, 55, 3702–3704.
4. BHUJANGA RAO, A. K. S., GUNDU RAO, C. AND SINGH, B. B. — *J. Chem. Res. (S)*, 1991, 350–351.
5. BHUJANGA RAO, A. K. S., PRASAD, R. S. AND SINGH, B. B. — *J. Chem. Soc., Perkin Trans. I*, 1989, 1352–1353.
6. BHUJANGA RAO, A. K. S., GUNDU RAO, C. AND SINGH, B. B. — *Synth. Commun.*, 1991, 21, 443–448.
7. BHUJANGA RAO, A. K. S., GUNDU RAO, C. AND SINGH, B. B. — *J. Chem. Res. (S)*, 1992, 196–197.
8. BHUJANGA RAO, A. K. S., GUNDU RAO, C. AND SINGH, B. B. — *J. Org. Chem.* 1992, 57, 3240–3242.
9. BHUJANGA RAO, A. K. S., GUNDU RAO, C. AND SINGH, B. B. — *Synth. Commun.*, 1993, 23, 341–351 and 353–366.

Thesis Abstract (Ph.D.)

Chemistry of spironaphthalenones–synthesis and reaction of oxygen and nitrogen heterocycles by P. V. P. Pragna Charyulu

Research supervisor: T. R. Kasturi
Department: Organic Chemistry

1. Introduction

High-potential quinones like 2,3-dichloro-5, 6-dicyano benzoquinone(DDQ)/*o*-chloranil have been mainly used to bring about dehydrogenations. However, in recent years, DDQ has been used as a reagent in organic synthesis[1-3]. DDQ has also been used as a reagent for the synthesis of several hetero aromatic compounds[4-6]. In the present study, oxidation of several spironaphthalenones (**1**) with DDQ has been studied and the interesting products obtained have been characterized. Further reactions of these compounds have also been studied.

2. Results and discussion

Oxidation of spironaphthalenone **1a** was carried out by refluxing with DDQ in benzene for 8 h. This resulted in the isolation of three compounds designated as A, B and C. Compound A has been assigned tropone structure **3a**, while compound B has been shown to be the DDHQ esters **4a** (*cis–cis* & *trans–trans* isomers). Compound C was shown to be polymeric material. The generality of spironaphthalenones (**1b–i**) with DDQ, when the corresponding compounds **3b–i** and **4b–i** were obtained in good yields. When the same reaction was carried out with 1'-aryl substituted spironaphthalenones **2j–m**, only the correspon-ding DDHQ esters **4j–m** were obtained. 1'-[3-nitrophenyl]-spironaphthalenone **2n** failed to undergo any oxidation. The oxatropone **3a** and DDHQ ester **4a** have been synthesized by an unambiguous route start-ing from the corresponding acid chloride. The mechanism of formation of these products has been rationalized.

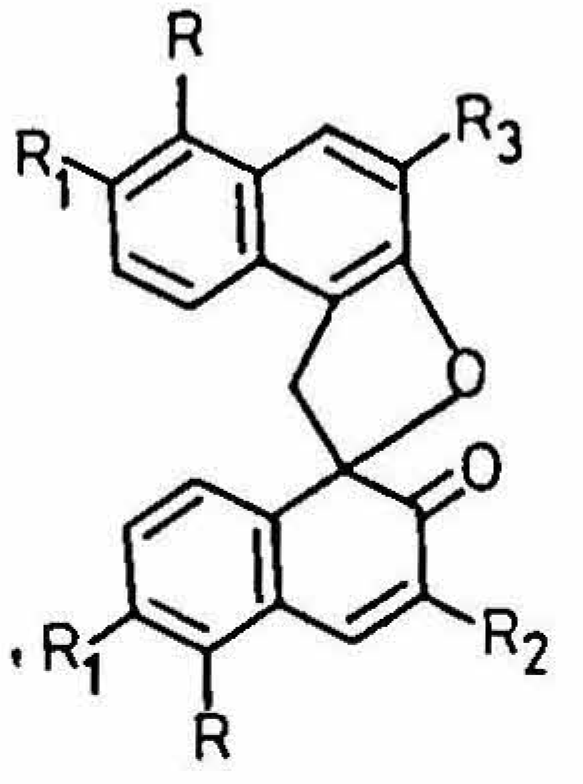

1a-i

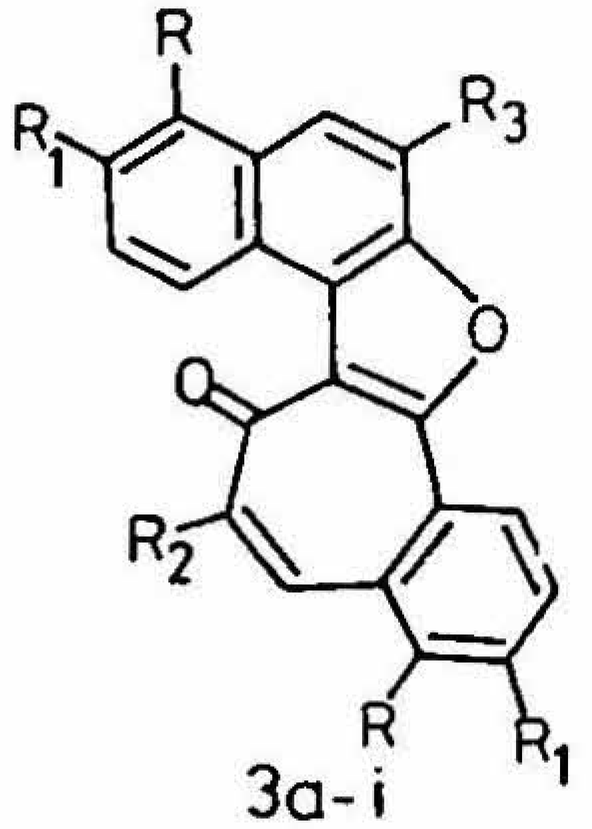

3a-i

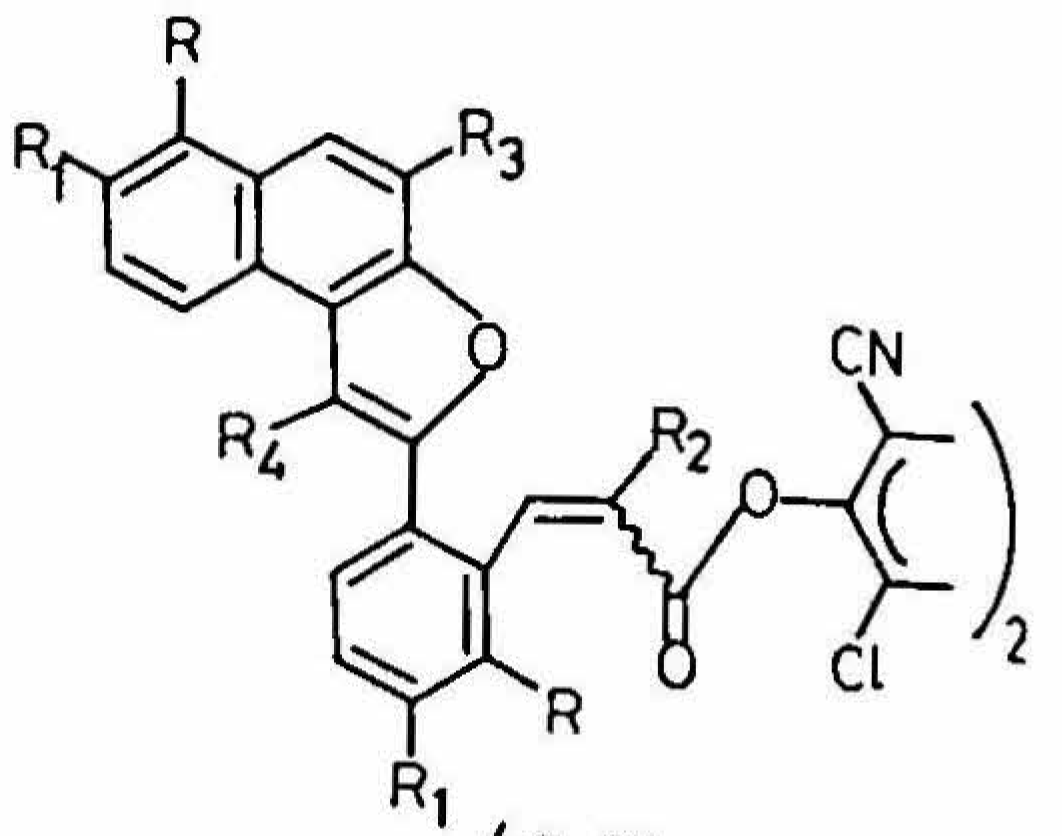

4a-m

(a) $R = R_1 = R_2 = R_3 = H$
(b) $R = R_2 = R_3 = H$; $R_1 = OCH_3$
(c) $R = R_2 = R_3 = H$; $R_1 = Br$
(d) $R = R_2 = R_3 = H$; $R_1 = t$-Bu
(e) $R = R_2 = R_3 = H$; $R_1 = -C_6H_{10}(CH_3)$
(f) $R_1 = R_2 = R_3 = H$; $R = CH_3$
(g) $R = R_1 = R_3 = H$; $R_2 = CH_3$
(h) $R = R_1 = R_2 = H$; $R_3 = CH_3$
(i) $R_1 = R_2 = R_3 = H$; $R = NO_2$
(j) $R = R_1 = R_2 = R_3 = H$; $R_4 = -Ph$
(k) $R = R_1 = R_2 = R_3 = H$; $R_4 = -Ph(2\text{-}OMe)$
(l) $R_1 = Br$; $R = R_2 = R_3 = H$; $R_4 = -Ph$
(m) $R_1 = Br$; $R = R_2 = R_3 = H$; $R_4 = -Ph(2\text{-}OMe)$

2j-n

(j) $R = R_1 = H$
(k) $R = H$; $R_1 = 2\text{-}OCH_3$
(l) $R = Br$; $R_1 = H$
(m) $R = Br$; $R_1 = 2\text{-}OCH_3$
(n) $R = H$; $R_1 = 3\text{-}NO_2$

The DDHQ ester **4a** obtained in the above oxidation, undergoes facile reduction with $NaBH_4$ at r.t. to give the corresponding alcohol **5a**. This reaction has been generalized by reaction with DDHQ esters **4e** and **4k**. The tetrachloro catechol esters, prepared by oxidation of spironaphthalenone with *o*-chloranil, also behaved similarly.

DDHQ esters (**4a–d**), on heating with Zn/AcOH, gives the cycloheptatriene derivatives **6a–d** along with the saturated acids **7a–d**. The cycloheptatriene derivatives on oxidation with CrO_3 gave the corresponding tropone derivatives.

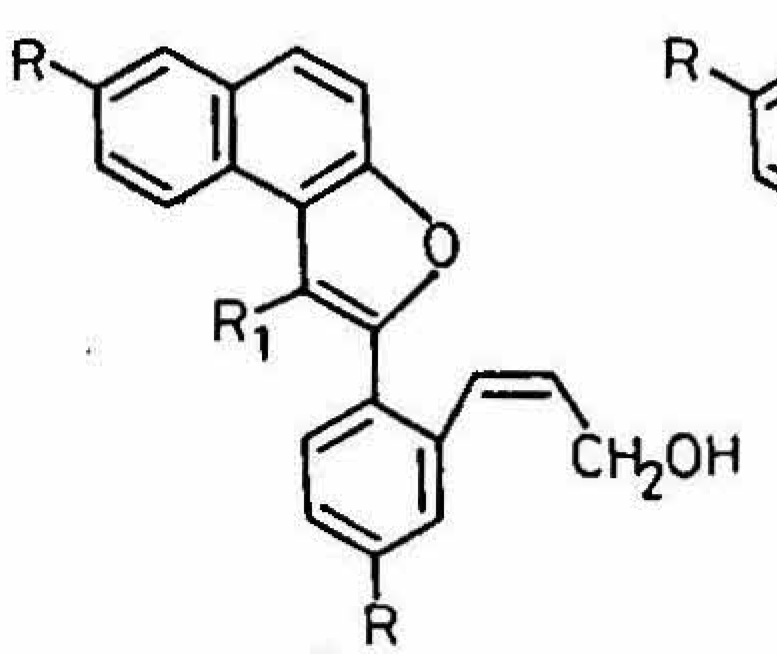

5

6a-d

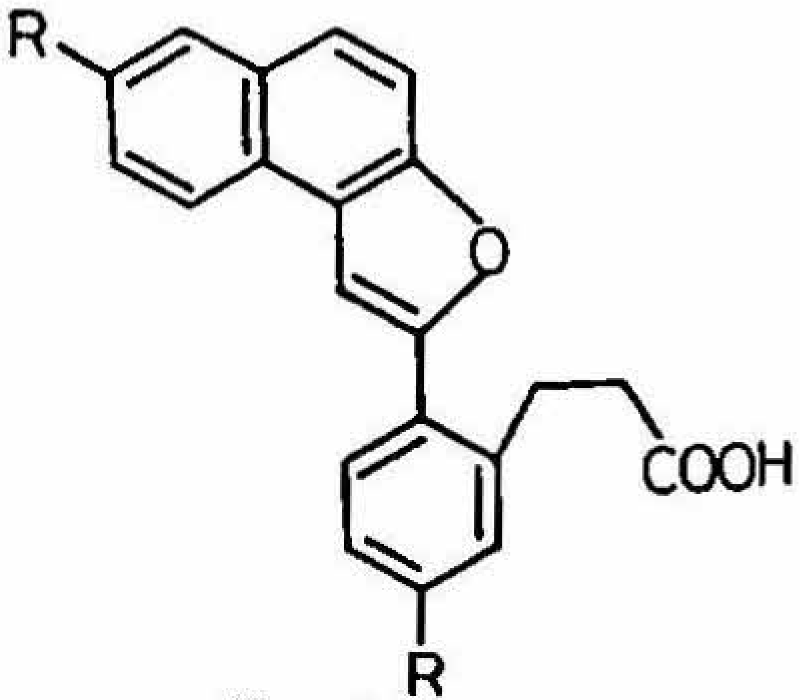

7a-d

(a) $R = R_1 = H$; (k) $R = H$; $R_1 = -Ph(2\text{-}OMe)$
(e) $R = -C_6H_{10}(CH_3)$; $R_1 = H$

(a) $R = H$
(b) $R = -OMe$
(c) $R = Br$
(d) $R = t$-Bu

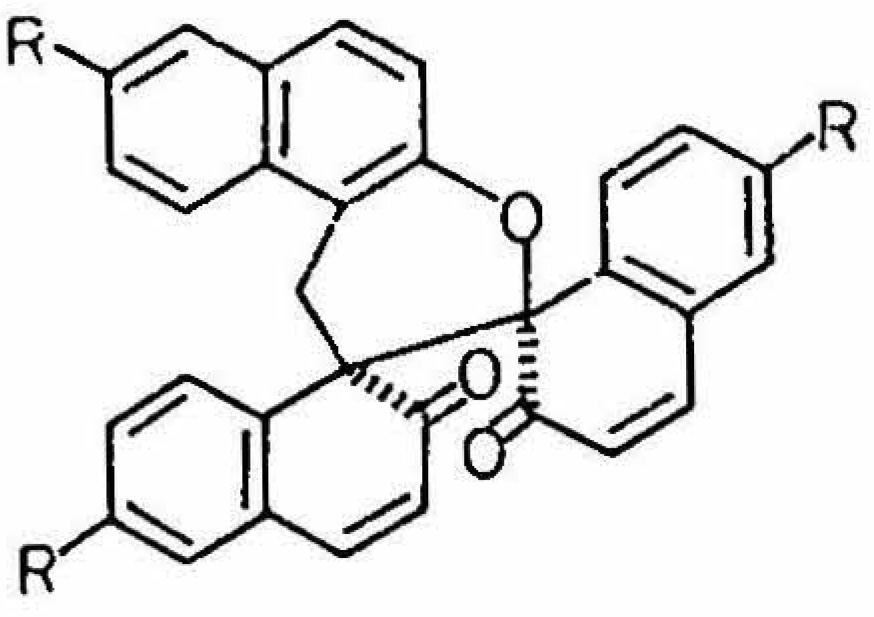

8a-c

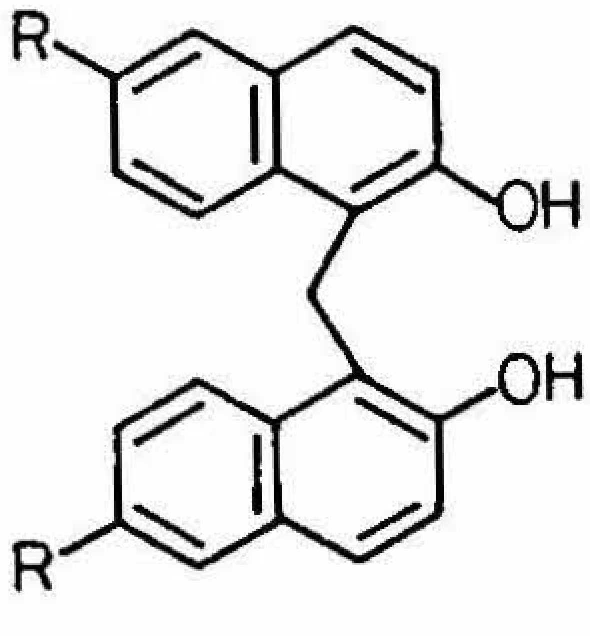

9a-c

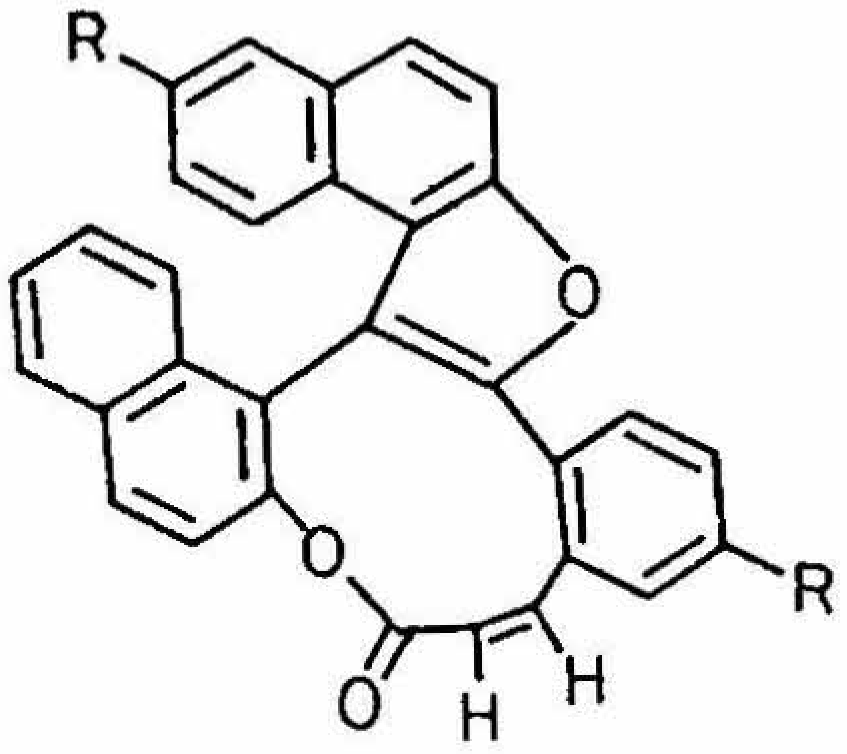

10a-C

(a) R = H; (b) R = *t*-Bu; (c) R = Br.

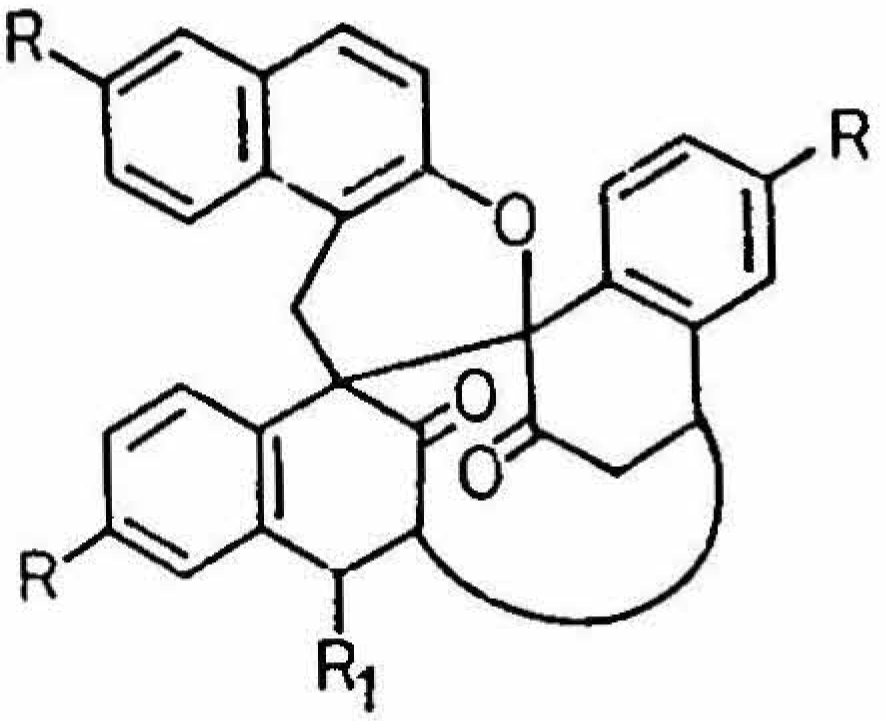

11a-e

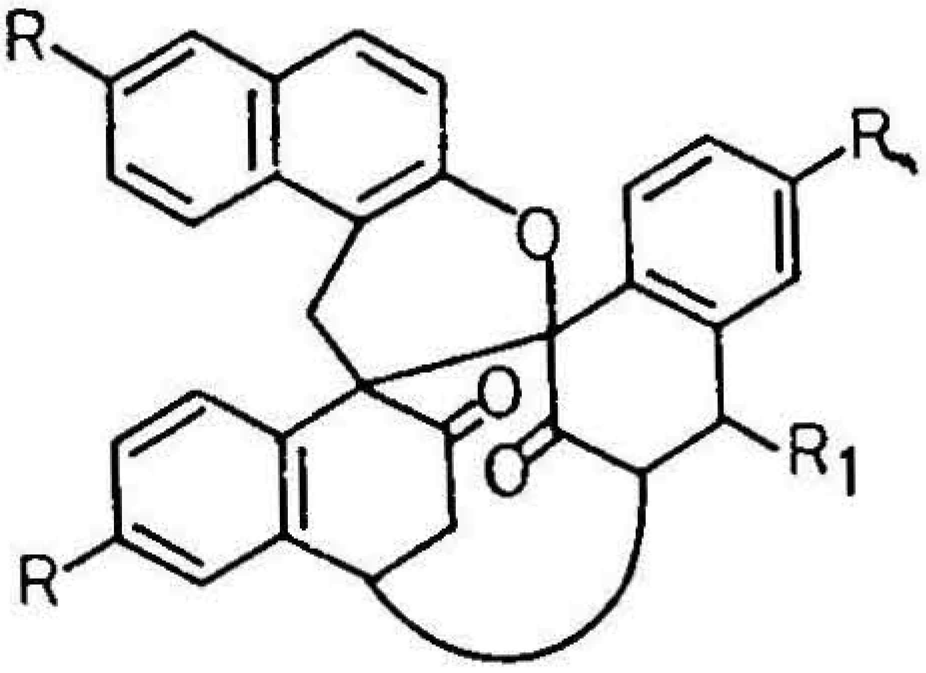

12a-e

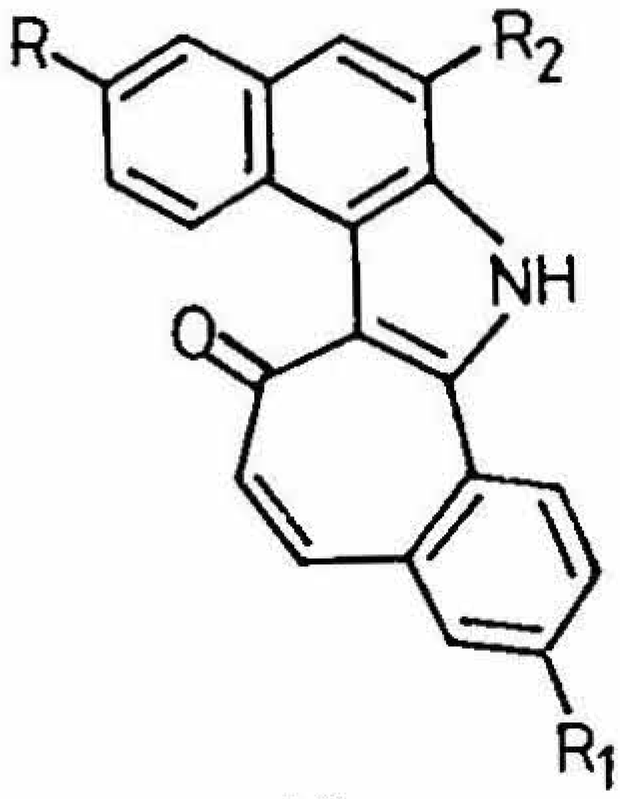

13a-c

(a) R = H; $R_1 = OCH_3$
(b) R = Br; $R_1 = OCH_3$
(c) R = *t*-Bu; $R_1 = OCH_3$
(d) R = H; $R_1 = -CH(CN)COOCH_3$
(e) R = H; $R_1 = -CH(CN)COOCH_2CH_3$

(a) $R = R_1 = R_2 = H$
(b) $R = R_1 =$ *t*-Bu; $R_2 = H$
(c) R = H; $R_1 = Br$; $R_2 = CH_3$

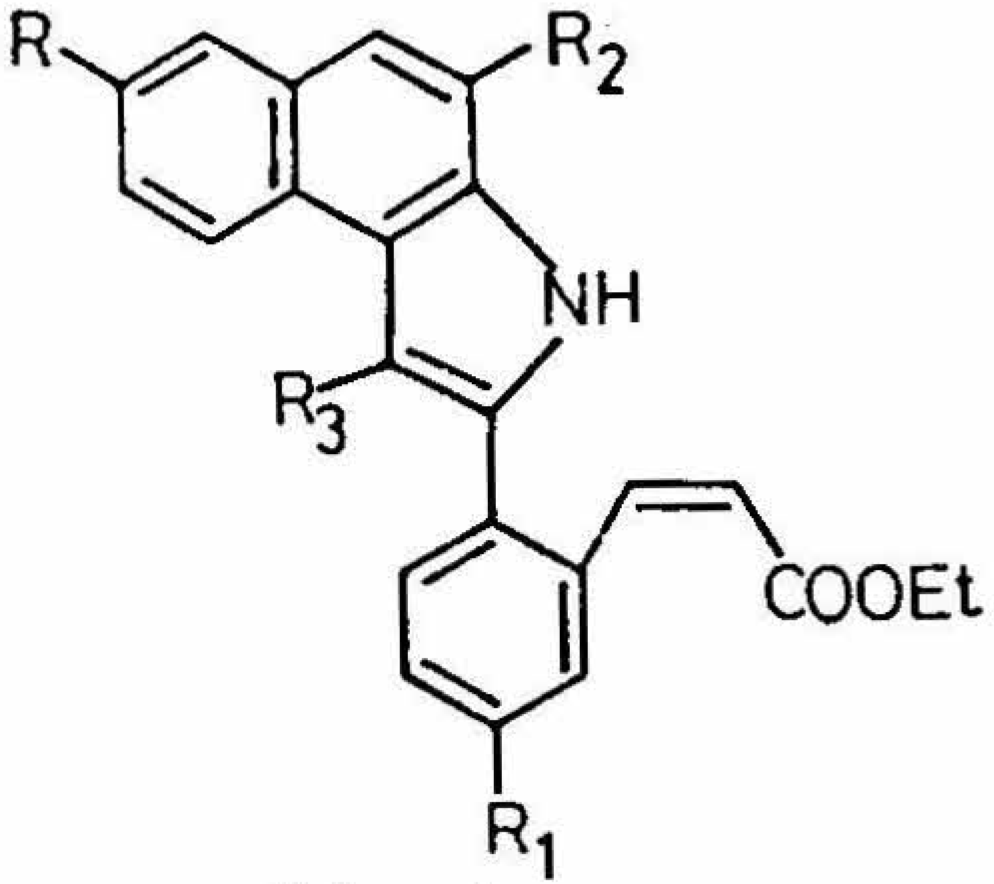

14a-d

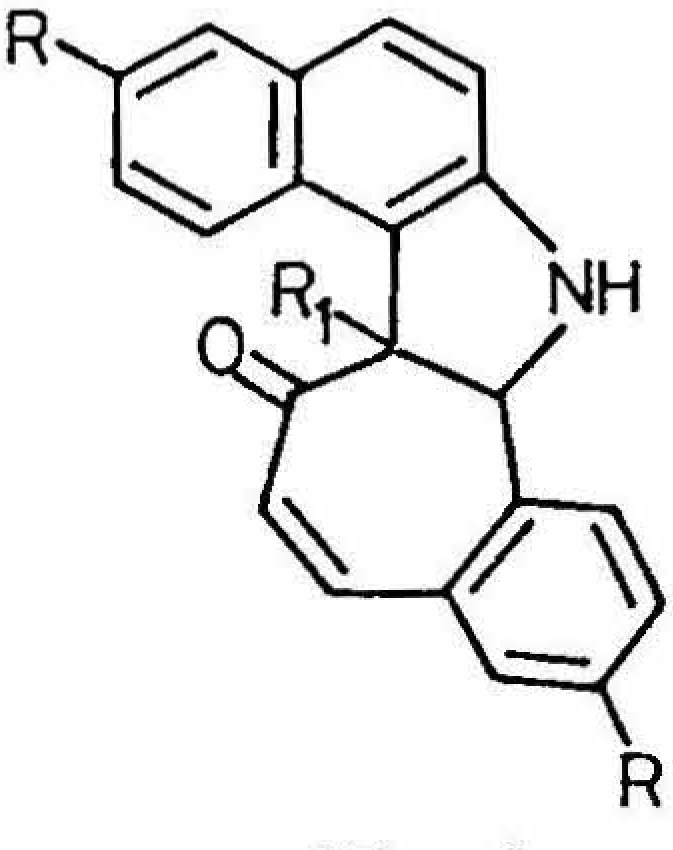

15a-f

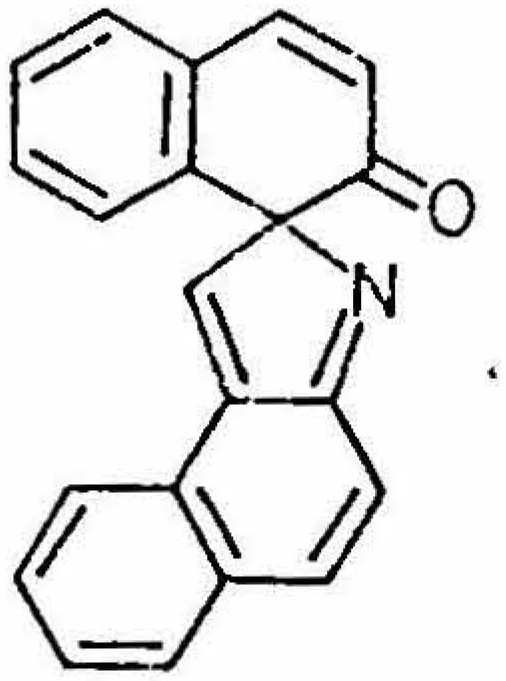

16

(a) $R = R_1 = R_2 = H$; $R_3 = -Ph$
(b) $R = R_1 = R_2 = H$; $R_3 = -Ph(2{-}OMe)$
(c) R = Br; $R_1 = R_2 = H$; $R_3 = -Ph$
(d) R = Br; $R_1 = R_2 = H$; $R_3 = -Ph(2{-}OMe)$

DDQ oxidation of dispironaphthalenone **8a–c**, obtained in the oxidation of bisnaphthol **9a–c** with KOBr, resulted in the formation of macrocyclic lactone **10a–c**, the structure of which was established by spectroscopic methods and confirmed further by X-ray crystal structure analysis. Attempts have been made to synthesize analogus lactones.

Cage compounds play an important role in the development of host–guest chemistry. A series of cage compounds **11a–e** and **12a–e** have been synthesized by novel intermolecular Tandem Michael reaction of dispironaphthalenones **8a–c** with different oxygen and carbon nucleophiles.

Dean and coworkers[7] have suggested the anhydro oxime structure **13a** for the product obtained in the reaction of spironaphthalenone **1a** with $NH_2OH.HCl$ in THF/EtOH. They have also suggested a mechanism for this transformation. The generality of this reaction has been studied by carrying out the reaction with spironaphthalenones **1a–c**, when the corresponding tropones, **13a–c** were obtained. When the reaction of 3-, 4'-, 5'-substituted spironaphthalenones were carried out, they gave isomeric pyrrolotropones, as evident from the NMR data.

The reaction of 1'-aryl substituted spironaphthalenones(**2j–m**) with $NH_2OH.HCl$ gave pyrroloesters **14a–d** instead of the expected dihydrotropones **15**. Based on these observations, an alternate mechanism involving the intermediacy of the isopyrrole derivative **16**, has been proposed to explain the formation of either pyrrolo tropones **13** or pyrroloester **14** in this reaction.

Results obtained in the oxidation of 1-[2-benzyloxy]-2-naphthol with different oxidizing agents are presented in the Appendix.

References

1. TURNER, A. B.	*Synthetic reagents* (J. S. Pizey, ed.), 1977, Vol. 4, pp. 193–225, Halstead–Wiley.
2. BEEKER, H. D., BJORK, A. AND ALDER, E.	*J. Org. Chem.*, 1980, 45, 1596–1598.
3. ZIMMERMAN, S. C. AND WU, W.	*J. Am. Chem. Soc.*, 1989, 111, 8054–8058; *J. Org. Chem.*, 1990, 55, 4789–4792.
4. KASTURI, T. R. AND JAYARAM, S. K.	*Indian J. Chem. B*, 1988, 27, 714–717.
5. KASTURI, T. R., JAYARAM, S. K AND LATA MATHEW	*Indian J. Chem. B*, 1990, 29, 628–631.
6. KASTURI, T. R. AND JAYARAM, S. K.	*Indian J. Chem. B*, 1991, 30, 539–544.
7. DEAN, F. M., FLETCHER, C. AND LOCKSLEY, H. D.	*J. Chem. Soc.*, 1964, 5096–5099.

Thesis Abstract (Ph.D.)

Electrochemical studies of sealed lead-acid battery electrode reactions by

S. Venugopalan
Research supervisors: S. Sathyanarayana and B. L. Agrawal
Department: Inorganic and Physical Chemistry

1. Introduction

In the area of secondary batteries lead-acid battery occupies a pre-eminent position as a long-life, low-cost battery. Modern trend is to operate this battery as a sealed unit. Conventional grid alloys for the positive electrode induce antimony position[1] of the negative electrodes which eventually lead to failure of sealed batteries by excessive hydrogen evolution. Hence either Sb-free or low-antimonial lead alloy grids are recommended for sealed cells[2]. One of the approaches to solve the problem of antimony poisoning resulting in high hydrogen gassing is to have an additive in the electrolyte. The addition of H_3PO_4 or its salts either to the electrolyte or to the positive active material aimed at increasing the life time, especially, with non-antimonial grids is known[3]. Although literature contains data on the effect of H_3PO_4 on the positive electrode, surprisingly, there is hardly any detailed study reported on its effects on the performance of the negative (Pb/$PbSO_4$) electrode. Moreover, re-optimization of the concentration of H_3PO_4 additive is required because of the use of higher than normal concentration of H_2SO_4 in the sealed system. The literature is lacking in this respect. In the present study, the effect of H_3PO_4 additive to the H_2SO_4 electrolyte has been investigated with a view to understand the mechanism of action of it on the kinetics of electrode processes at PB, PB-Ca-Sn and Pb-Sb-Se alloy grid materials both in the presence as well as in the absence of dissolved Sb(III).

2. Experimental

The techniques/instrumental methods used are electrochemical polarization measurements in three electrode configuration in the Tafel as well as in the linear domains, galvanostatic potential-time transients, open circuit potential-time transients, electrical conductivity measurements, potentiometry, UV spectrophotometry, atomic absorption spectroscopy and gasometry.

Electrochemical polarization measurements in three electrode configuration were carried out in the cathodic Tafel domain for pure Pb(99.97%), Pb-0.08 Ca-0.3 Sn, and Pb-2 Sb-0,05 Se alloys in H_2SO_4 in the range [3-10 M] at five levels of H_3PO_4 [0, 10, 20, 30 and 40 $g.l^{-1}$] and each with three levels of Sb(III) [0, 1 and 10 mg l^{-1}].

3. Results and conclusions

It is well documented in the literature[4] that cathodic polarization of Pb in H_2SO_4 gives rise to hysteresis of the polarization curve originally attributed to adsorption–desorption of SO_4^{2-} ions. In this study, it is demonstrated that the initial rise in the polarization curve is due to the establishment of a limiting current for Pb deposition which will lead to a hysteresis between forward and reverse sweeps of polarization. By controlling the Pb ion concentration in the electrolyte, it has been possible to identify a domain to provide highly reproducible, steady-state, hysteresis-free Tafel line for HER on Pb and Pb-alloys in H_2SO_4 solutions. A typical Tafel plot for smooth Pb electrode in 5.298 M H_2SO_4 containing different amounts of H_3PO_4 additive is shown Fig. 1. Since there was no significant change in the Tafel slopes, it has been inferred that the mechanism of HER on lead and lead-alloys is unaffected by the addition of H_3PO_4 to the electrolyte. In this work it has been unambiguously established that H_3PO_4 additive increases the overpotential for hydrogen evolution reaction on pure lead as well as on lead-alloy electrodes. It has been shown that the increase in the overpotential for HER due to H_3PO_4 additive shows a maxima at 20 $g.l^{-1}$. The presence of dissolved Sb(III) was found to decrease the overpotential for HER. H_3PO_4 additive was found to suppress this adverse effect of dissolved Sb(III) on the overpotential for HER on Pb and Pb-alloys and this effect of H_3PO_4 additive of partially offsetting the adverse influence of Sb(III) was also found to be optimal at 20 $g.l^{-1}$. All these effects of H_3PO_4 additive were in fact of a general nature with respect to H_2SO_4 concentration and lead-alloy electrodes. Since the corrosion of lead

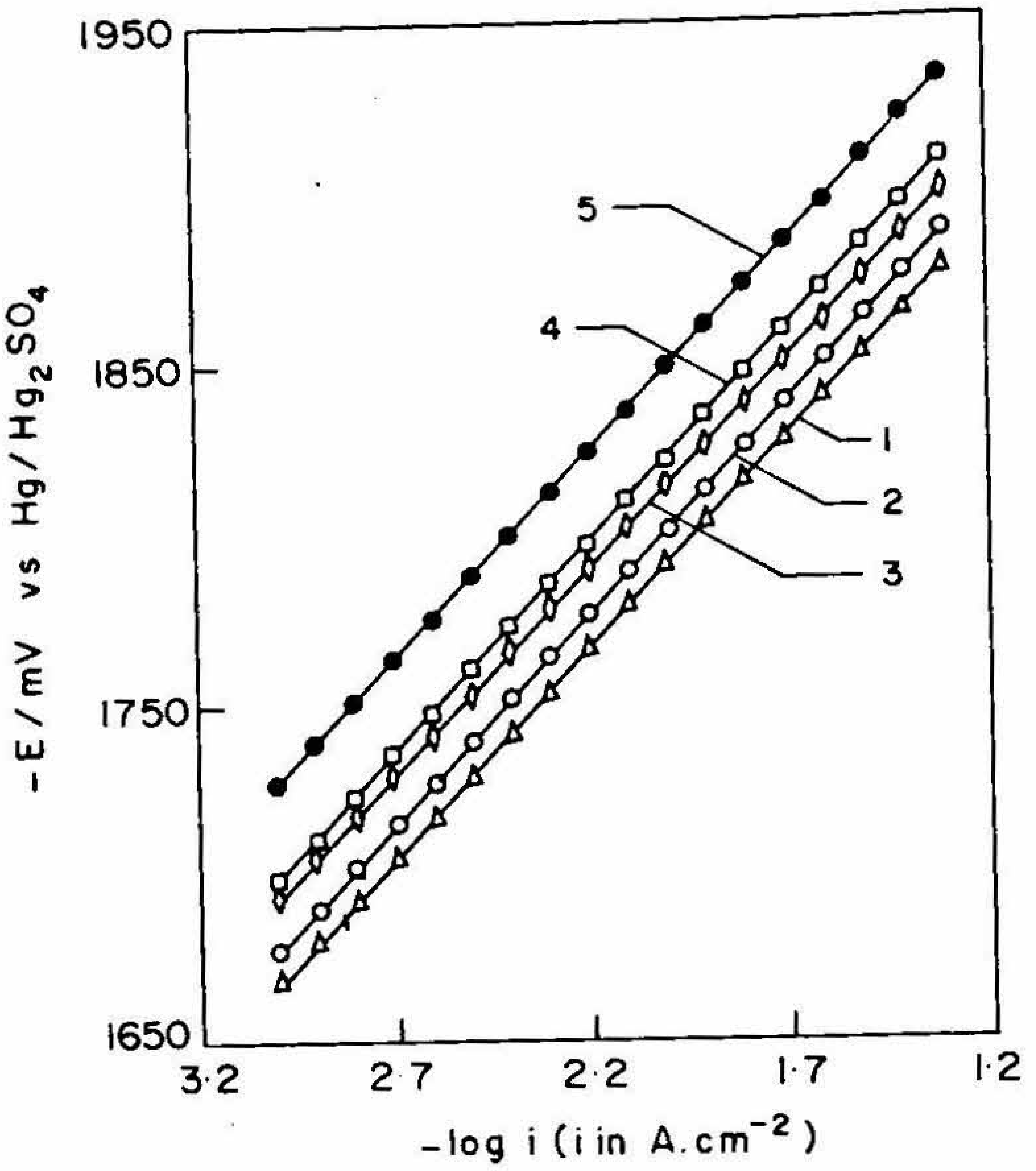

FIG. 1. Tafel plots for HER on smooth, pure Pb electrode in H_2SO_4 (5.3 M) with different concentrations of H_3PO_4, g.l^{-1}: (1) 0, (2) 40, (3) 30, (4) 10, (5) 20. E_{cor} = −968 ± 2mV *vs* Hg/Hg_2SO_4 for all the curves.

and lead alloys in H_3PO_4 electrolyte is controlled by the kinetics of HER, the increase in the overpotential for HER results in a reduction in the corrosion rate of these alloys. It was found (through steady-state, galvanostatic, cathodic polarization in the low-overpotential region, of smooth pure lead electrode in H_2 saturated, $PbSO_4$ saturated, well stirred H_2SO_4 with and without H_3PO_4 additive) that the kinetics of $Pb/PbSO_4$ reaction is unaffected in the presence of small quantities of H_3PO_4. Measurement of specific conductance of H_2SO_4 solutions showed a slight, nearly linear decrease with an increase in the concentration of H_3PO_4 in solution. The open-circuit potential-time transients and galvano-static cathodic polarization potential-time transients with and without H_3PO_4 additive suggested strong adsorption of H_3PO_4 molecules and $H_2PO_4^-$ ions on active sites of corrosion which was in accordance with Garche *et al.*[5] and Morris *et al.*[6]. The results have been interpreted with a theoretical model based on adsorption of H_3PO_4 in the double layer. It can be concluded from this investigation that H_3PO_4 additive to the electrolyte of the sealed lead acid battery (SLA) would minimize the present limitations and might improve the performance of SLA significantly.

References

1. BAGSHAW, N. E.	*J. Power Sources*, 1991, 33, 3-11.
2. FOLLENKAMP, A. F.	*J. Power Sources*, 1991, 36, 567-585.
3. VOSS, E.	*J. Power Sources*, 1988, 24, 171-184.
4. HAYES, M. AND KUHN, A. T.	In *The electrochemistry of lead*, (A. T. Kuhn, ed), pp. 201-203, 1979, Academic Press.

5. GARCHE, J., DORING, H. AND WIESENER, K. — *J. Power Sources*, 1991, 33, 213-220.

6. MORRIS, G. A., MITCHELL, P. J., HAMPSON, N. A. AND DYSON, J. I. — *Power Sources 12, Int. Power Sources Symp. Committee*, (T. Keily and B. W. Baxter, eds), Leatherhead, UK, 1989, pp. 61–75.

Thesis Abstract (Ph. D.)

Theoretical studies of the α- and β-cleavage processes in organic photochemistry by

Sumathy Raman

Research supervisor: A. K. Chandra

Department: Inorganic and Physical Chemistry

1. Introduction

A qualitative understanding of the chemical reaction and the ability to predict the branching between the energetically allowed product channels are the points of interest in the area of chemical reaction dynamics. Carbonyl compounds on irradiation with ultraviolet light undergo a variety of chemical reactions such as α-cleavages, β-cleavages, γ-hydrogen abstraction, cyclo addition and molecular rearrangements, etc[1]. The major photoreaction is the Norrish Type I process. The n,π^* excitation of the carbonyl group leads to a vacancy in the n-orbital. The overlap of this n-orbital with the α-carbon σ bond results in the weakening of the α-carbon carbonyl carbon bond. This was a useful phenomenological concept in early stages. Later on, correlation diagrams such as Salem's correlation diagrams[2] and natural orbital correlation diagrams[3] are used to understand this photochemical reaction. Nagashima *et al.*[4] in 1988 considered the force responsible for converting the reactant to product structure to explain the mechanism of this process. All these studies fail to reveal the existence of barriers on the potential energy surface (PES). Kinetic data on α-cleavage processes are scarce. The reported values of the activation barriers[5] obtained from studies of their temperature dependence are of doubtful validity since the accompanying photophysical processes are also temperature dependent. Therefore, the object of the present investigation is to obtain a mechanistic picture of the α-cleavage and β-cleavage processes. All unsymmetric ketones are characterized by two different α-bonds. In the present work, we address the question of selectivity of the α-cleavage process of one of the two σ bonds adjacent to the carbonyl chromophore by considering the third derivative of energy with respect to the reaction coordinate at the starting point of the reaction, *i.e.*, the anharmonicity at the starting point. Besides this, the effect of an α-substituent on the rate of the α-cleavage process as well as on the photochemical primary process is also dealt with.

2. Method of computation[6, 7]

For large systems semi-empirical methods (MINDO/3) with configuration interaction (CI) have been employed while for a few small systems, *ab initio* calculations were carried out at the single configuration level to obtain the PES in the lowest triplet state. All possible configurations arising from the highest six occupied MOs and the lowest six unoccupied MOs were taken into consideration. First, in a single configuration level, the geometry optimizations were carried out as a function of elongation of the σ bond lengths adjacent to the chromophore. The molecular orbitals were then used to construct the singly and doubly excited configurations which are mixed by CI. The energy of the ground state was redetermined after mixing with the doubly excited configurations. The vertical excitation energies are then calculated at each value of the elongated bond length and then added to the corresponding ground state energies to obtain the potential energy surface for the excited states. The wavefunction of the excited states is a linear combination of several starting configurations having the same symmetry and multiplicity.

All *ab initio* calculations were carried out with the Gaussian86 program. For open shell systems the unrestricted Hartree-Fock(UHF) method was adopted at the three different levels of computation, namely, 3-21G, 6-31G*, 6-31g*/MP2. Geometry optimizations were carried out using the analytical first derivatives of energy with respect to nuclear displacements (Berny optimization). Computed energies and gradients were utilized effectively in one of the several multiparameter geometry optimization procedures to obtain equilibrium structures. The number of negative eigenvalues of the Hessian matrix is characteristic of the nature of the stationary point. Vibrational frequencies and zero point energies were obtained by the harmonic approximation from the analytical second derivatives at the UHF/6-31g* level.

3. Results and conclusion

The MINDO/3-CI PES for the type I process in acetaldehyde, trimethyl acetaldehyde, *t*-butyl methyl ketone and acetyl chloride are already reported[6]. The process from the ground state is a homolytic-bound rupture and is expected to be more costly than the molecular fragmentation from the lowest excited states. The hei-ght of the diabatic activation barrier is estimated from the point of crossing to the energy of the verti-cally excited state of the molecule. The $^{1,3}(n,\pi^*)$ state (A")surface crosses with the (n, σ^*) surface (A') as the α-bond is elongated. The crossing is avoided through vibronic coupling $< n, \pi^* | \mathrm{dv/dQ} | n, \sigma^* >$ where dV/dQ is the nuclear electron potential operator and Q is the nuclear coordinate of A" symmetry. The transition density on the carbonyl carbon is an order of magnitude larger than on the heteroatoms of the chromophore. Therefore, the reaction coordinate (R) on the triplet state involves the symmetric stretch of the α-bond (X) as well as the perpendicular motion of the carbonyl carbon (Y). The first derivative dE/dR is not adequate for discrimination as the second and third differentials are non-vanishing for the Y component of R. Although d^2E/dR^2 is not discriminative d^3E/dR^3 (anharmonicity) is different for different alpha bonds. Force method using Heilman-Feynman theorem and finite difference method were employed to estimate the anharmonicity.

Ab initio studies on formyl flouride[7] reveal that HFCO can decompose rapidly into H + FCO with high internal energies. Molecular elimination is the dominant process in the ground state. Importance of tunneling depends on the wavelength of excitation. The transition state structure reveals that H-swings off perpendicular to the FCO plane. Decomposition to F + HCO is difficult on the excited surface. The triatomic radical FCO$^{\cdot}$ decomposes into F and CO from the high vibrational levels of C–F stretch. Calculations suggest the formation of rationally excited CO molecule.

Substitution of a heteroatom with lone pair of electrons in the alpha position introduces change in the primary process in unsubstituted ketones[8]. Non-alkyl substituents adjacent to the carbonyl group which are excited by direct adsorption of light or energy transfer introduce the new process, namely, β-cleavage. β-cleavage is a homolytic process leading to free radicals. The barrier for the β-cleavage process arises from the avoided crossing to $n_S\pi^*_{CO}\left(\sigma^*_{C-S}\right)$ with $\sigma_{C-S}\pi^*_{CO}\left(\sigma^*_{C-S}\right)$ state.

References

1. Turro, N. J. — *Modern molecular photochemistry*, 1978, Benjamin/Cummings, California.
2. Dauben, W. G., Salem, L. and Turro, N. J. — *Acc. Chem. Res.*, 1975, 8, 41–54.
3. Bigot, B., Devaquet, A. and Turro, N. J. — *J. Am. Chem. Soc.*, 1981, 103, 6–12.
4. Nagaoka, G. *et al.* — *J. Phys. Chem.*, 1988, 92, 166–171.
5. Mirbach, M. F., Mirbach, M. J., Liu, K. and Turro, N. J. — *J. Photochem.*, 1978, 8, 299–306.
6. Chandra, A. K. and Sumathi, R. — *J. Photochem. Photobiol.*, 1990, 52, 213–234.
7. Sumathi, R. and Chandra, A. K. — *Chem. Phys.*, 1992, 165, 257–263.
8. Sumathi, R. and Chandra, A. K. — *J. Chem. Soc., Perkin Trans. II*, 1992, 291–294.

Thesis Abstract (Ph. D.)

Transition metal organometallic chemistry of 1,3,2 λ^3, 4λ^3-diazadiphosphetidines by

V. Sreenivasa Reddy
Research supervisor: S. S. Krishnamurthy
Department: Inorganic and Physical Chemistry

1. Introduction

The four-membered 1,3,2 λ^3, 4λ^3-diazadiphosphetidines (cyclodiphosphazanes), $[RNPX]_2$ possess two trivalent phosphorus centres in close proximity and offers interesting possibilities as ligands. Cyclodiphosphazanes can exist in *cis* and *trans* isomeric forms (**I** and **II**) which are interconvertible in solution[1,2]. Studies on the coordination chemistry of cyclodiphosphazanes reported to date are mainly concerned with the complexes of the platinum metals and rhenium with ligands, *cis*-$[Bu^tNP(X)]_2$ (X = Cl, F or Me), whereas reactions with metal carbonyls have been less well investigated[3-5]. Despite the fact that the cyclodiphosphazanes can also act as potentially bidentate ligands, the coordination chemistry of this system has received a little attention owing to the complexity of the reactions and difficulty of characterization of the products. The present investigation is concerned with the synthesis of organo-transition metal complexes of cyclodiphosphazanes and a study of different coordination behaviours of *cis*- and *trans*-isomers towards Group 6 metal carbonyl moieties.

2. Experimental

All the reactions were carried out in dry N_2 atmosphere using standard Schlenk-type glassware[6]. All the operations such as distillation of the solvents, filtration of the solutions and chromatographic purifications were performed under dry N_2 atmosphere. Air-sensitive solids were handled inside a glove bag or glove box filled with dry N_2. Solvents were purified by conventional procedures[7] and were purged with dry N_2 prior to use.

The transition metal precursors such as *cis*-$[M(CO)_4C_7H_8)]$ (M = Cr, Mo or W), *cis*-$\{M(CO)_4(NHC_5H_{10})_2]$ (M = Mo or W), *cis*-$[Mo(CO)_4(NHC_5H_{10})P(OMe)_3]$, $[Mo(Cp)(CO)_3]_2$, and *cis*-$[MCl_2COD]$ (pd and Pt) were prepared by published procedures.

Melting points of the compounds were determined on a Reichart-Kofler microheating stage fitted with a polarizing microscope. Elemental analyses were performed on a Heraeus CHN-O-Rapid analyzer and some of the analyses were obtained from the City University, London, UK. Infrared spectra were recorded on a Perkin-Elmer model 781 or a Hitachi-270-50 spectrometers. NMR spectra were recorded on Bruker ACF-200, Bruker WH-270 and Bruker AMX-400 spectrometers, in $CDCl_3$ or CD_2Cl_2 solvents. ^1H and ^{13}C chemical shifts were measured with reference to the internal standard, Me_4Si. The ^{31}p chemical shifts were measured with reference to the external standard, *viz*., 85% H_3PO_4, under proton decoupled conditions. Positive chemical shifts are downfield of the standard. The X-ray diffraction data were collected using an Enraf–Nonius CAD-4 diffractometer (Mo Kα, = 0.71069 Å) equipped with a graphite monochromator.

3. Results and discussion

The *p*-methyl phenoxy- and trifluoroethoxy- substituted cyclodiphosphazanes $[PhNP(OR)]_2$ (R = Ch_2CF_3 or C_6H_4Me-*p*) have been chosen for the purpose of present investigation because these substituents impart hydrolytic and thermal stability to many phosphorus derivatives. The geometrical isomerism of these cyclodiphosphazanes has been studied by ^{31}P NMR spectroscopy.

The reactions of cyclodiphosphazane, $[PhNP(OC_6H_4Me$-*p*$)]_2$ (3:1 mixture of *cis* and *trans* isomers) with $[M(CO)_4NBD]$ (M = Cr, Mo or W; NBD = norbornadiene) give the mononuclear complexes of the type *cis*-$[M(CO)_4\{$*cis*-$[PhNP(OC_6H_4Me$-*p*$)]_2\}_2]$(**III**), whereas analogous reactions with $[M(CO)_4(NHC_5H_{10})\ (A)]$ (M = Mo, A = $P(OMe)_3$; M = W, A = NHC_5H_{10}) yield the complexes of the type *cis*-$[\{M(CO)_4(A)\}\ \{$*cis*-$[PhNP(OC_6H_4Me$-*p*$)]_2\}]$ (**IV**) in which the cyclodiphosphazane (in its *cis*-form) is coordinated in η^1-fashion. In contrast, the *trans*-cyclodiphosphazane, $[PhNP(OCH_2CF_3)]_2$ reacts with $[M(CO)_4(NHC_5H_{10})(A)]$ (M = Mo or

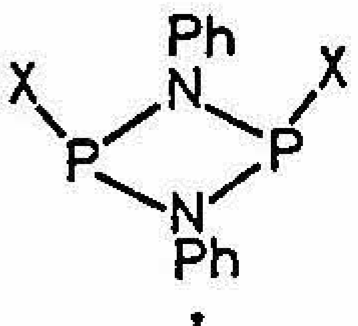

I

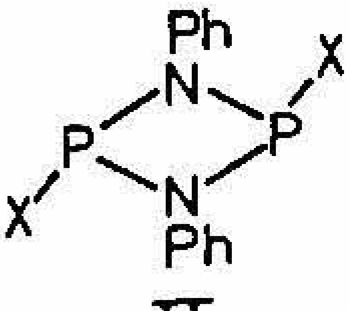

II

$X = OC_6H_4Me$-p or $X = OCH_2CF_3$

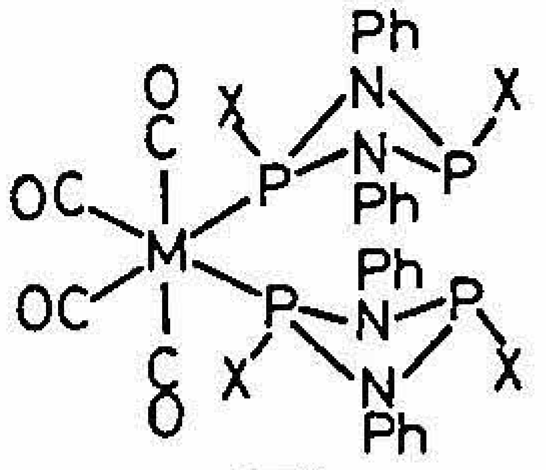

III

$M = Cr, Mo, W$

$X = OC_6H_4Me$

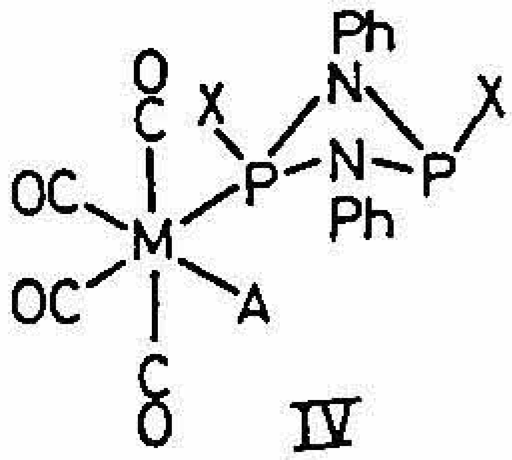

IV

$X = OC_6H_4Me$

a $M = Mo$, $A = P(OMe)_3$

b $M = W$; $A = NHC_5H_{10}$

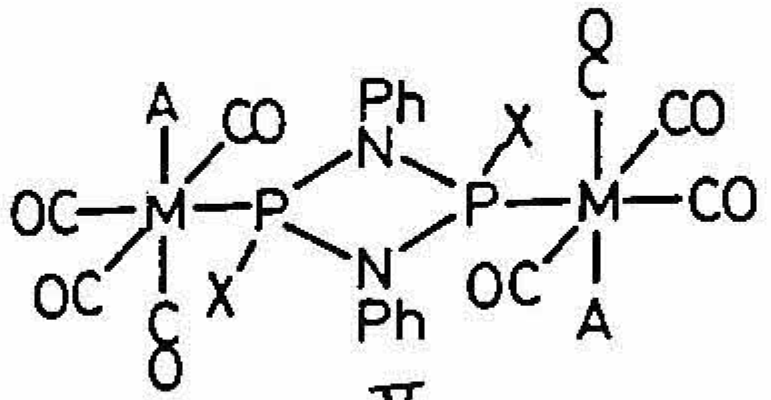

V

$X = OCH_2CF_3$

a $M = Mo, W$; $A = NHC_5H_{10}$

b $M = Mo$; $A = P(OMe)_3$

c $M = Mo$; $A = [PhNP(OCH_2CF_3)]_2$

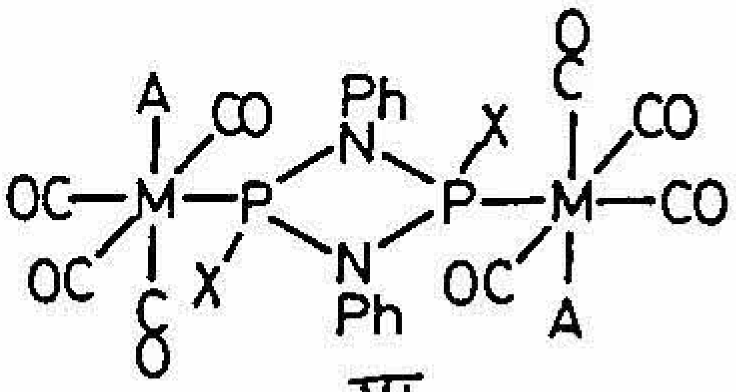

VI

$X = OC_6H_4Me$-p

$M = Mo$; $A = P(OMe)_3$

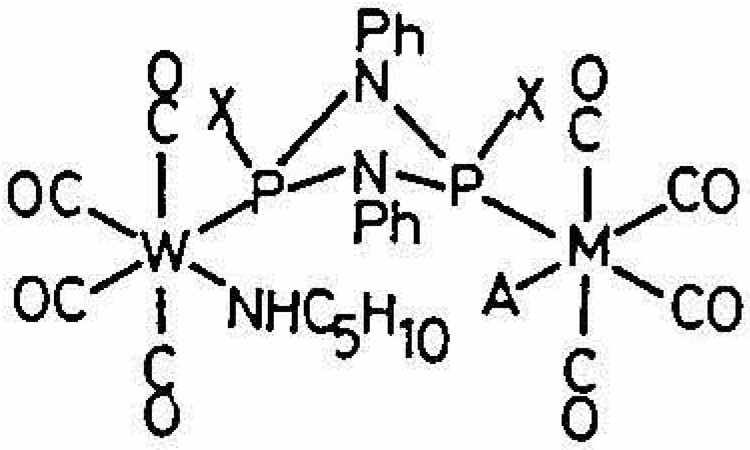

VII

$X = OC_6H_4Me$

$M = W$; $A = NHC_5H_{10}$

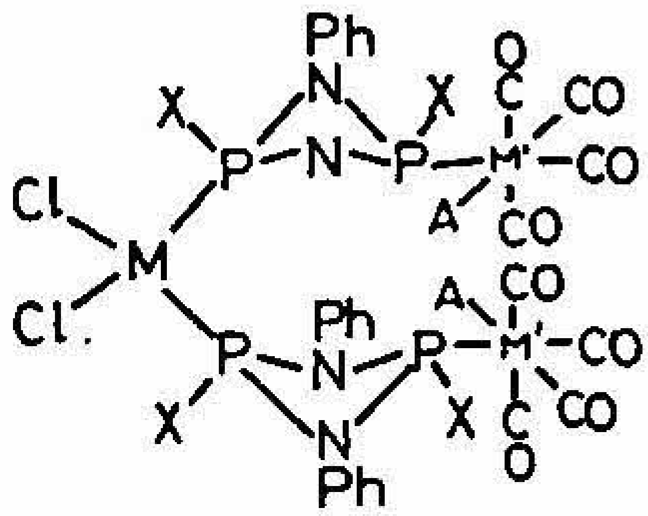

VIII

$X = OC_6H_4Me$

$M = Pt$ or Pd

$M' = Mo$, $A = P(OMe)_3$

$M' = W$; $A = NHC_5H_{10}$

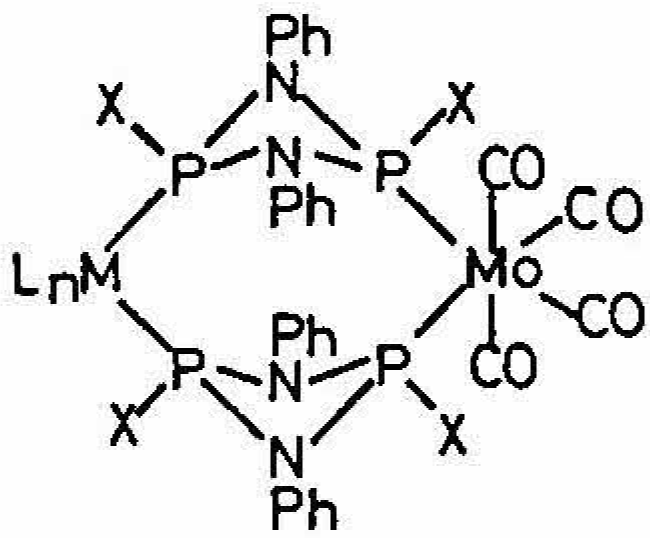

IX

$X = OC_6H_4Me$ or OCH_2CF_3 ; $ML_n = Mo(CO)_4$

$X = OC_6H_4Me$; $ML_n = PdCl_2$ or $PtCl_2$

$\mathrm{W, A = NHC_5H_{10}; M = Mo, A = P(OMe)_3)}$ or with $[\mathrm{Mo(CO)_4NBD}]$ to give dinuclear complexes of the type $[\{\mathrm{M(CO)_4(A)}\}_2\{\mu\text{-}\textit{trans}\text{-}[\mathrm{PhNP(OCH_2CF_3)}]_2\}]$(**Va**, **b** and $[\mathrm{Mo_2(CO)_8}\{\textit{trans}\text{-}[\mathrm{PhNP(OCH_2CF_3)}]_2\}_3]$(**Vc**), respectively. The ^{31}P NMR chemical shifts of **Vc** indicates the presence of both bridging as well as η^1-coordinated cyclodiphosphazane ligands. Isomerization of $\textit{cis}\text{-}[\mathrm{Mo(CO)_4}\{\textit{cis}\text{-}[\mathrm{PhNP(OC_6H_4Me}\text{-}p)]_2\}_2]$ to $\textit{cis}\text{-}[\mathrm{Mo(CO)_4}\{\textit{trans}\text{-}[\mathrm{PhNP(OC_6H_4Me}\text{-}p)]_2\}_2]$ in boiling benzene has been established by ^{31}P NMR spectroscopy. The reaction of the cyclodiphosphazane, $[\mathrm{PhNP(OC_6H_4Me}\text{-}p)]_2$ with $\textit{fac}\text{-}[\mathrm{M(CO)_3(NCMe)_3}]$ (M = Mo or W) and $[\mathrm{Mo(CO)_4(\eta^3\text{-}C_7H_7}]$ have also been investigated.

The mononuclear complexes of the type **III** and **IV** possess one or two uncoordinated phosphorus centres and hence these are good starting materials for the synthesis of both homo- and heterobimetallic complexes as well as trinuclear complexes. The mononuclear complexes $\textit{cis}\text{-}[\mathrm{Mo(CO)_4(A)}\{\textit{cis}\text{-}[\mathrm{PhNP(OC_6H_4Me}\text{-}p)]_2\}]$($\mathrm{M = Mo, A = P(OMe)_3; M = W, A = NHC_5H_{10}}$) react with $\textit{cis}\text{-}[\mathrm{Mo(CO)_4(A)(NHC_5H_{10})}]$ to afford either homo-bimetallic complexes of the type $[\{\mathrm{M(CO)_4(A)}\}_2\{\mu\text{-}[\mathrm{PhNP(OC_6H_4Me}\text{-}p)]_2\}]$ or the heterobimetallic complex$[\mathrm{(OC)_4(MeO)_3PMo}\{\textit{cis}\text{-}[\mathrm{PhNP(OC_6H_4Me}\text{-}p)]_2\}\mathrm{W(CO)_4(NHC_5H_{10})}]$. In the dimolybdenum complex (**VI**) the cyclodiphosphazane has changed its configuration to *trans* form whereas in ditungsten complex and heterobimetallic complex (**VII**) the cyclodiphosphazane retains its *cis* configuration as revealed by X-ray crystal structures. Formation of the dinuclear complex (**VI**) takes place *via* the *cis* isomer $[\{\mathrm{Mo(CO)_4(A)}\}_2\{\mu\text{-}\textit{cis}\text{-}[\mathrm{PhNP(OC_6H_4Me}\text{-}p)]_2\}]$ as confirmed by ^{31}P NMR spectroscopy. The mononuclear complexes (**IV**) react with $\textit{cis}\text{-}[\mathrm{MCl_2(COD)}]$(M = Pd or Pt) to give the trinuclear complexes of the type $\textit{cis}\text{-}[\mathrm{MCl_2}\{\textit{cis}\text{-}\mathrm{M'(CO)_4(A)}\{\textit{cis}\text{-}[\mathrm{PhNP(OC_6H_4Me}\text{-}p)]_2\}\}_2]$ (**VIII**).

The mononuclear complexes, $\textit{cis}\text{-}[\mathrm{Mo(CO)_4}\{\textit{cis}\text{-}[\mathrm{PhNP(OR)}]_2\}_2]$ (**III**), react with $[\mathrm{Mo(CO)_4NBD}]$ or with $[\mathrm{Mo(CO)_4(NHC_5H_{10})_2}]$ to give the dinuclear complexes of the type $[\mathrm{Mo_2(CO)_8}\{\mu\text{-}\textit{cis}\text{-}[\mathrm{PhNP(OR)}]_2\}_2]$ (**IX**, $\mathrm{ML_n = Mo(CO)_4}$), whereas the reaction with $\textit{cis}\text{-}\{\mathrm{MCl_2COD}]$ gives the hetero-bimetallic complexes of the type $[\mathrm{(OC)_4Mo}\{\mu\text{-}\textit{cis}\text{-}[\mathrm{PhNP(OC_6H_4Me}\text{-}p)]_2\}_2\mathrm{MCl_2}]$ (**IX**, $\mathrm{ML_n = PdCl_2}$ or $\mathrm{PtCl_2}$). In these complexes two metal moieties are bridged by two cyclodiphoshazane ligands. In contrast, $\textit{cis}\text{-}[\mathrm{Mo(CO)_4}\{\textit{cis}\text{-}[\mathrm{PhNP(OC_6H_4Me}\text{-}p)]_2\}_2]$(**III**) reacts with $[\mathrm{W(CO)_4(NHC_5H_{10})_2}]$ to give the dimolybdenum complex **IX** ($\mathrm{ML_n = Mo(CO)_4}$) along with the mononuclear tungsten complex $\textit{cis}\text{-}[\mathrm{W(CO)_4(NHC_5H_{10})}\{\textit{cis}\text{-}[\mathrm{PhNP(OC_6H_4Me}\text{-}p)]_2\}]$ (**IVb**). A possible mechanism is proposed for the observed reaction patterns.

It has been demonstrated that *cis*- and *trans*-cyclodiphosphazanes behave differently in their coordination behaviour towards Group 6 metal carbonyl moieties. The mononuclear complexes which possess one or two uncoordinated phosphorus centres have proven to be good synthons for homo- and hetero-dinuclear as well as trinuclear complexes. A combination of X-ray crystallographic studies and Phosphorus-31 NMR spectroscopy has helped in unravelling the complexity of the reactions of cyclodiphosphazanes with metal carbonyls.

References

1. Keat, R. *Top. Cur. Chem.*, 1982, **102**, 89–116.
2. Chem, H. J., Haltiwanger, R. C., Hill, T. G., Thompson, M. L., Coons, D. E. and Norman, A. D. *Inorg. Chem.*, 1985, 24, 4725–4730.
3. Burckett St. Laurent, J. C. T. R., Hitchcock, P. B. and Nixon, J. F. *J. Organomet. Chem.*, 1984, 262, 379–389.
4. Burckett St. Laurent, J. C. T. R., Hitchcock, P. B. and Nixon, J. F. *J. Organomet. Chem.*, 1983, 249, 243–254.
5. Scherer, O. J., Anselmann, R. and Sheldrick, W. S. *J. Organomet. Chem.*, 1984, 263, C26–C29.
6. Shriver, D. F. and Drezdzon. *The manipulation of air-sensitive compounds*, 2nd edn, 1986, Wiley-Interscience.
7. Perrin, D. D. and Armarego, W. L. F. *Purification of laboratory chemicals*, 3rd edn., 1988, Pergamon Press.

Thesis Abstract (Ph.D.)

Regulation of fibroin gene expression in *Bombyx mori* by Rahul V. Gopalakrishnan

Research supervisor: K. P. Gopinathan
Department: Molecular and Cellular Biology

1. Introduction

The silkworm, *Bombyx mori*, has been exploited as a convenient model system for the study of eukaryotic gene expression and its control[1]. The genes investigated include chorion genes, certain *t*RNA genes (alanyl and glycyl), the actin genes and the genes encoding the cocoon proteins; the silk fibre protein, fibroin, the glue proteins, sericin(s) and P_{25} the fibroin light chain component.

The silk glands which are modified salivary glands are the site of synthesis of the silk proteins and the synthesis of silk proteins are regulated in a tissue-specific manner. The expression of these genes is also regulated in a developmental stage-specific manner confined to the larval stages and the maximal expression is achieved during the 5th instar of development just prior to the production of the silk cocoon. Previous work from other laboratories has demonstrated that the tissue-specific expression of the fibroin gene is regulated at the transcriptional level[2]. Moreover work from our own laboratory has shown in addition that the developmental stage, specific expression of fibroin is also regulated post-transcriptionally presumably at the level of translation due to the nonavailability of sufficient amounts of cognate *t*RNAs[3]. The present study was undertaken to identify the *cis*-acting DNA sequence elements and the *trans*-activating proteins that were involved in the transcriptional regulation of fibroin gene expression.

2. Results and discussion

The basic premise of the investigation was that specific protein–nucleic acid interactions at these regulatory regions are primarily responsible for regulation of expression. The studies were confined to a region of the fibroin gene covering the 5' flanking sequences up to 800 nucleotides from the transcription start site of the gene. The experimental approach involved the making of DNA constructs harbouring sequence elements which have various segments of these regions and the *in vitro* transcription of these constructs to define their roles. To carry out the *in vitro* transcription a method for the preparation of nuclear extracts from homologous silkgland tissue was developed. The extracts were active for the transcription of both RNA polymerase II and polymerase III transcribed genes. Deletion subclones were constructed from the full-length genomic clone pFb29. A schematic representation of pFb29 and the subclones constructed from it is shown in Fig. 1. These subclones spanned various areas of the fibroin upstream and were used for transcriptional studies and DNA–protein interaction analyses.

Conditions for optimal transcription of exogenously added fibroin templates *in vitro* were standardized using the direct incorporation of labelled NTPs. Incubation for 1 h at 25°C with template concentrations between 1–2 µg gave the best results. The extracts were completely dependent on externally added templates for transcription. The fibroin gene constructs containing the sequences between +66 and –233 was transcribed best *in vitro* and the sequences between –95 and –233 caused an enhancement in transcriptional levels (Fig. 2). The sequences upstream of –233 appeared to contain a negative regulatory element. RNA synthesis by heterologous nuclear extracts derived from the MSG and ovarian tissues (which do not express fibroin *in vivo*) showed transcriptional activity for the fibroin templates but at much lower levels than the homologous PSG extracts. The sequence required for highest *in vitro* transcription were similar in PSG, MSG and ovarian extracts.

Run-off transcription analysis showed that a transcript of an authentic size (transcription initiation occurred at the correct transcription start site) was produced in the presence of exogenously added fibroin template. S1 nuclease analysis with three fibroin upstream deletion subclones (pF94, pF233 and pF540) indicated that pF233 (harbouring sequences up to –233) was transcribed best and sequences between –233 and –540 (pF540) when present, exerted a negative effect on transcription. The latter result suggested the presence of a negative-regulatory element in this region. Based on these results it was concluded that the homologous transcription extracts were able to faithfully transcribe exogenously added DNA in a template-dependent manner and were able to distinguish between different DNA elements reflecting their roles in fibroin gene expression.

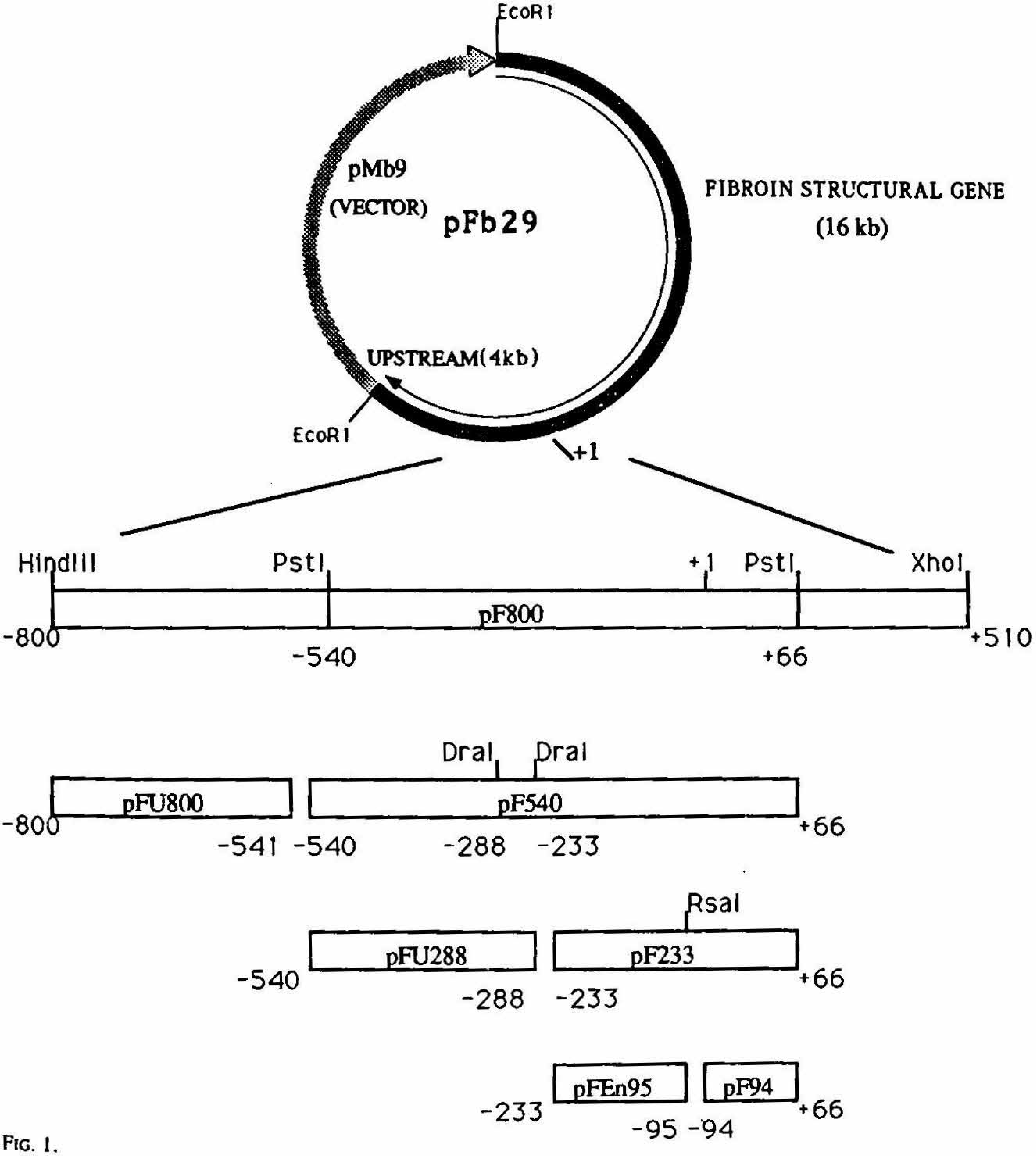

FIG. 1.

The studies were therefore extended to characterize the protein–DNA interactions at these elements. These studies were carried out using gel retardation, South Western, UV crosslinking and footprinting analyses.

The results indicated that the same or similar factor(s) were binding to the sequence elements in all the three probes used in the analysis spanning 300bp of the fibroin upstream. Retardation chase experiments and the relative strength of binding indicated that the common factor(s) bound more strongly to the region downstream of –94 compared to sequence between –95 and –233. The single complex formed with probe pFU288 was not chased out on competition with sequences between –233 and +66 showing that the proteins binding in this region (between –288 and –540) were different. The factor binding to this probe could be responsible for

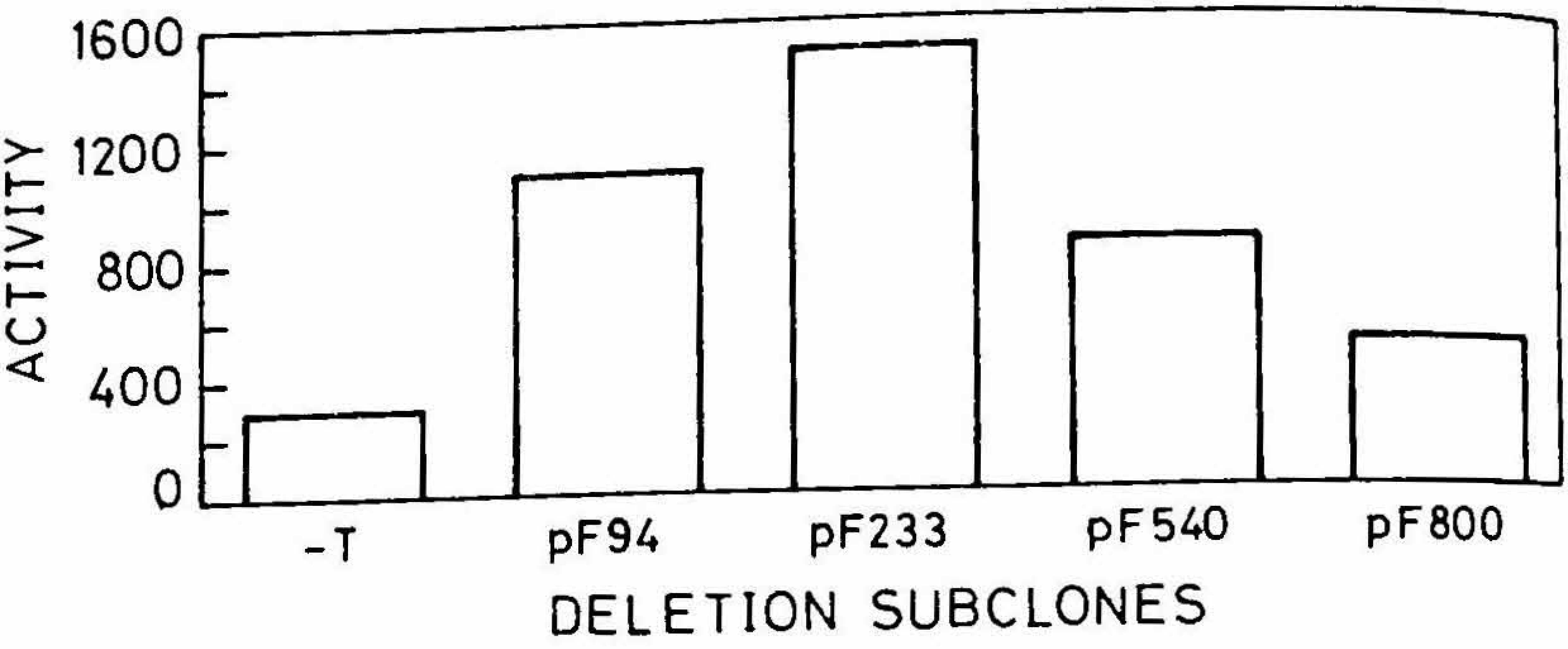

PSG Extract
–T = NO TEMPLATE ADDED
ACTIVITY MONITORED AS CPM INCORPORATED
1000 cpm = 0.1 pmole

FIG. 2. Fibrion transcription. Transcription of deletion subclones.

the negative influence on fibroin transcription seen *in vitro*. Gel retardation carried out indicated that the protein-binding patterns with MSG or PSG nuclear extracts were similar for a given probe. However, the patterns of binding with the ovarian extracts were different from either PSG or MSG patterns obtained. Attempts were made to fractionate PSG nuclear extracts on a heparin sepharose column to characterize factors interacting with fibroin gene probes.

Footprinting of specific sequences involved in protein binding was carried out. For this purpose the chemical nuclease, copper–phenanthroline was utilized. The results from these studies indicated that the sequences between –94 and +66 were extensively protected over a large area by PSG nuclear extracts suggesting large areas of protein binding. The footprinting of sequences between –233 and –95 showed that there were three major areas of protection between –229 and –221, –216 and –195, and –178 and –157. Footprinting analysis of the –540 to –288 region did not show any protection. A computer-aided homology search was carried out between the sequences protected in different upstream regions. A given transcription factor should recognise and bind to a specific sequence or set of closely related sequences. The homology search would therefore predict the sites of those factors which bound both the non-overlapping probes pF94 and pFEn95 in gel retardation assays.

3. Conclusion

The protein–DNA interaction studies showed that many complex interactions occurred between the upstream sequences of the fibroin gene and protein factors present in the nuclear extracts, while the transcriptional analysis delineated the positive or negative role of various upstream regions.

References

1. SUZUKI, V. *Results and problems in cell differentiation*, Vol. 8, pp. 1–44, 1977.
2. MAEKAWA, H. AND SUZUKI, Y. *Dev. Biol.*, 1980, 78, 394–406.
3. PATEL, C. V. AND GOPINATHAN, K. P. *Indian J. Biochem. Biophys.*, 1991, 28, 521–530.

Thesis Abstract (Ph.D.)

Molecular characterization of genes and promoters of mycobacteriophage I3 by

G. R. Ramesh
Research supervisor: K. P. Gopinathan
Department: Microbiology and Cell Biology

1. Introduction

Although more than 250 mycobacteriophages have been isolated, only limited information is available on the molecular aspects of their biology. Except for phage L5, not much is known about the genome organization or the genes of mycobacteriophages. Mycobacteriophage I3, isolated in our laboratory[1,2], is one of the few transducing mycobacteriophages and resembles phage L5 in some aspects. However, Phage I3 is unique among mycobacteriophages in having a contractile tail. Besides, the 135 kbp linear genomic DNA of phage I3 harbors the presence of 6–7 random single-strand gaps of 6–10 nucleotides each on each strand[3,4]. Although phage I3 is one of the best characterized mycobacteriophages in terms of physiology and genome organization, the molecular aspects of its biology are still unclear. The present work describes the molecular analysis of the genes and promoters of the phage I3.

2. Results and discussion

The number of sites for various restriction enzymes in I3 DNA was determined. In general, the number of sites for enzymes with AT-rich recognition sequence were few and GC-rich recognition sequence restriction sites were more. This is a reflection of the high GC content (68%) of the DNA. The large DNA fragments generated by the BamHI and HindIII enzymes were resolved by a combination of conventional and pulsed field gel electrophoresis. The computed restriction map for these two enzymes is presented in Fig. 1.

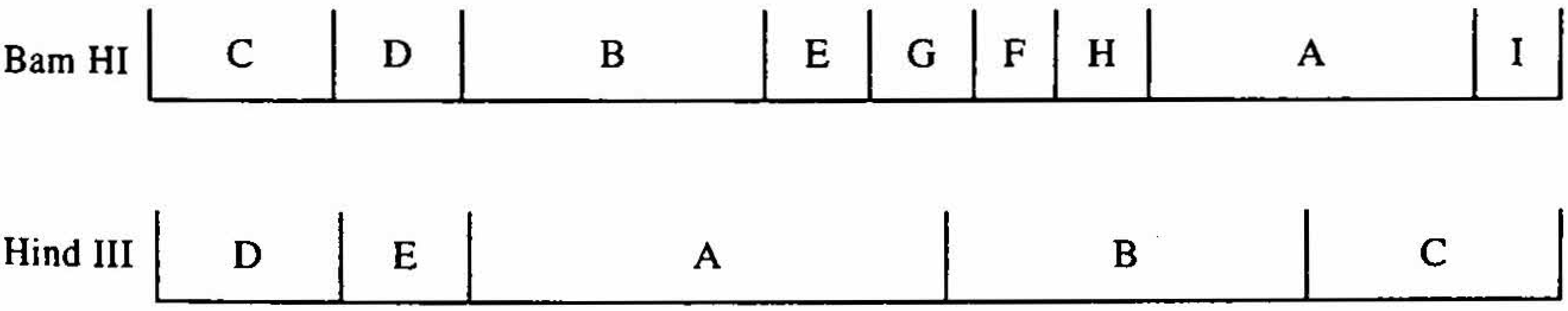

FIG. 1. Restriction map of phage I3 DNA.

The structural proteins of phage I3 were resolved on SDS–polyacrylamide gels and analysed by silver nitrate and coomassie blue staining. Immunoprecipitation and immunoblotting techniques were also used to determine and confirm the number of structural proteins in phage I3 to be 36. This is the largest number of proteins reported for any mycobacteriophage. The presence of very large-sized proteins (> 200 kD) indicated that these could be crosslinked multimeric forms of the low molecular weight proteins. Similar observation has been reported in the mycobacteriophage L5[5].

A genomic library of phage I3 DNA was constructed in *E. coli* vector and screened for the expression of I3 structural protein genes using antisera raised against the phage structural proteins. A recombinant expressing the 17 kD structural protein of phage I3 was identified, analysed and the DNA sequence of the gene was determined. The gene had its own initiation and termination signals to regulate transcription and translation. The promoter sequence identified in the upstream sequence of the gene showed a very high degree of homology in the –35 region to those in *E. coli* while the –10 region was totally different. The deduced amino acid sequence showed an unusual richness of proline residues (16%) and a characteristic codon bias for a G or C in the 3rd position. Similar biased codon usage has been reported in GC-rich organisms like *Streptomyces*[6] and mycobacteria[7].

Table I

Potential transcriptional regulatory sequences in mycobacterial genes

	-35	-10
E. coli	TTGACA	TATAAT
M. Tuberculosis		
32kD antigen	TTGAGA	AAGAAT
35kD antigen	TCGACA	TAAATT
BCG 64kD antigen	TTGCCG	TTTCAT
BCG alpha antigen	TCGACA	TATGTT
BCG 23kD antigen	TCGTCG	TATGTT
BCG 18kD antigen	TTGAGG	TACAGG
M. Leprae		
65kD antigen	TTGACA	TAAAAA
18kD antigen	TTGTCT	TATATC
SOD	TGGGCG	GATTAT
36kD antigen	TTTCCT	TACGTT
16S *r*RNA gene	TTGACT	ATTAAT
S. coelicolor dag A	TTGTCA	TAGCAT
Phage I3 consensus	TCGACA	C/TNATCT

Note: Promoters from heat shock genes are not included. The list contains only those genes where complete published sequences were available.

Phage I3 promoters were analysed by cloning the I3 DNA restriction fragments in the promoter selection vector pKK 232–8. The recombinants were screened on plates containing increasing concentrations of the selective antibiotic. Accordingly, the clones were classified into low-, medium- and high-resistance conferring groups. This also reflected the relative strengths of the cloned promoters. Enzyme extracts prepared from four clones showing high resistance were assayed for both endogenous promoter activity and the reported gene activity under the control of the cloned promoter. The results indicated that two of these cloned promoters were of equal strength to the endogenous promoter while the other two showed half the strength. DNA sequence analysis of these promoters showed considerable homology to the –35 regions of the promoters of *E. coli* and mycobacteria but differed completely in the –10 regions. A probable consensus for the I3 promoters has been proposed and a comparison of the promoter sequences of mycobacteria is presented in Table I.

The 70 kD structural protein gene of the phage I3 was cloned and expressed in the expression vector pKK 223–3. The expression of the gene has been confirmed by immuno dot blot and Western blot techniques. The complete nucleotide sequence of the 2.3 kbp insert was determined by generating unidirectional nested deletions using exonuclease III followed by DNA sequencing. The possibility of the 70 kD protein gene being part of an operon was indicated upon analysis of the DNA sequence. The deduced protein sequence revealed the abundance of valine, alanine, proline, threonine, glycine and asparagine residues. The characteristic codon bias of GC-rich organisms for a G or C at the 3rd position was also observed.

References

1. Sundar Raj, C. V. and Ramakrishnan, T. *Nature*, 1970, **228**, 280–281.

2. Saroja, D. and Gopinathan, K. P. *Antimicrob. Agents/Chemother.*, 1973, 4, 643–645.
3. Reddy, A. B. and Gopinathan, K. P. *Gene*, 1986, 44, 227–234.
4. Reddy, A. B. and Gopinathan, K. P. *FEMS Microbiol. Lett.*, 1986, 37, 163–167.
5. Sarkis, G. and Hatfull, G. F. *Mol. Microbiol.*, 1993, 7, 395–405.
6. Buttner, M. J., Fearnley, I. M. and Bibb, M. J. *Mol Gen. Genet.*, 1987, 209, 101–109.
7. Dale, J. W. and Patki, A. In *Molecular biology of the mycobacteria* (McFadden, J., ed.), 1990, p. 173, Academic Press.

Thesis Abstract (Ph.D.)

Transcriptional regulation of *t*RNA^{Gly} genes in the silk worm *Bombyx mori* by

Reshma Taneja
Research supervisor: K. P. Gopinathan
Department: Molecular and Cellular Biology

1. Introduction

The posterior silk gland (PSG) of the silkworm *Bombyx mori* is a highly specialized tissue involved in the synthesis of large amounts of the silk protein fibroin. There is a functional adaptation in PSG during the Vth larval instar to gear the system for the specialized function. A hallmark of this is the change in the contents of the *t*RNA populations highly favourable to synthesize fibroin, which has a prominent codon bias. Fibroin has an unusual amino acid composition of 46% glycine, 28% alanine, 12% serine and 5% tyrosine[1]. The *t*RNAs specific for the major amino acids in fibroin account for about 70% of the total *t*RNA population and of these *t*RNA$_1^{Gly}$ is the most predominant (23%). Although there are an estimated 20 copies of the *t*RNA$_1^{Gly}$ gene in *B. Mori*, no *t*RNA$_1^{Gly}$ gene specific to the silk gland has been identified so far[2]. It is therefore important to see whether the various *t*RNA$_1^{Gly}$ gene alleles are expressed differentially and if so, how they are regulated.

2. Results and discussion

In the present study, the transcriptional requirements of *t*RNA$_1^{Gly}$ genes from *B. Mori* have been examined in order to identify the *cis*-acting elements and the *trans*-acting regulatory factors. As a first step towards this end, a homologous nuclear extract from PSG has been developed which could efficiently and accurately transcribe the *t*RNA$_1^{Gly}$ genes *in vitro*. Nine *t*RNA$_1^{Gly}$ genes (pR8, pBmP1, pBmI1, pBmH1, pBmT1, pBmS1, pBmJ1, pBmU1 and pBmK1) which have identical coding regions but vary in their 5′ and 3′ flanking sequences were analyzed for transcription in this homologous system. The genes were differentially transcribed with the highest level of transcription of pR8 followed by pBmI1 and pBmP1 > pBmH1 > pBmT1. The clone pBmS1 which has two tRNA$_1^{Gly}$ genes gave rise to two distinct transcripts. The clone pBmJ1 was barely transcribed whereas pBmU1 and pBmK1 were transcriptionally inactive. Primer extension and S1 nuclease analysis indicated that the transcription of pRB initiated at –4 and that of pBmP1 at –3 and –5, the +1 being designated as the first nucleotide of the mature *t*RNA.

To determine the *cis*-acting elements required for transcription of these genes, deletion mutants were constructed. The parental clone pR8 has the 5′ flanking sequences up to –300 and about 30 nucleotides downstream to the coding region including the termination signals. Deletions of internal promoter or upstream sequences beyond –2, –40 and –150 were constructed and their effect on transcription efficiency was tested. As anticipated, the clone which lacked the B promoter was not transcribed. Similarly, the clone lacking the entire upstream sequences was transcriptionally inactive. However, the presence of sequences up to –40 clearly restored transcription, suggesting that in addition to the interal promoters the 5′ flanking sequences were necessary and sufficient to transcriptional activity of this $tRNA_1^{Gly}$ gene. Even more significantly, deletions beyond –40 and –150 showed enhanced transcription over the parental clone pR8. The higher transcription of a –150 deletion over and above the parental clone suggested the presence of a negative regulatory element in the region between –150 and –300. Further, the possible presence of a second positive regulatory element between –150 and –40 was also implicated from the higher levels of transcription of the deletion clones (–150 upstream deletion being transcribed better than the –40 deletion).

To determine whether the other $tRNA_1^{Gly}$ genes had similar sequence requirements, transcription competition assays were done. The competitors used were either an oligonucleotide spanning the –5 to –38 (corresponding to the putative positive element), or a fragment spanning the negative element. Based on these assays, the positive element was found to be common to all the clones examined. The presence of the negative element was restricted to selected clones. These results suggested that the negative regulatory element may therefore have some role in the differential transcription of the various $tRNA_1^{Gly}$ genes and/or in their tissue-specific expression[3].

DNA–protein interaction studies were carried out to ascertain the role of these elements. A gel mobility shift assay using the –40 to +53 fragment showed a single complex which was effectively chased by an oligonucleotide corresponding to the upstream region (–5 to –38) but not with another oligonucleotide, corresponding to the A box region (+5 to +35). When the region farthest upstream corresponding to the negative element was used for gel-retardation assays, two complexes were seen. The footprinting analysis of this complex indicated a protected region between –270 and –276, corresponding to the sequence TATATAA, an alternating purine–pyrimidine repeat.

Sequencing of the 5′ flanking region of pBmP1 revealed an element TATATAG (–231 to –237) similar to the negative element of pR8. Another motif, nearly identical to the above elements but located in the 3′ flanking region at +233 to +239 was identified. More detailed analysis of the functional determinants of these genes(pBmP1 and pR8) was done by swapping of domains between them. A series of subclones were constructed by systematically transferring various regions of the upstream regulatory sequences from pR8 into a subclone containing the structural and downstream sequences of pBmP1(Fig. 1). *In vitro* transcription of these clones indicated that like pR8, a –4 deletion of pBmP1 was barely transcribed indicating that the 5′ flanking sequences are essential for transcription of this gene also. Transcription analysis of the hybrid genes led to the functional identification of the negative elements in the 5′ and 3′ flanking sequences of pBmP1. When the

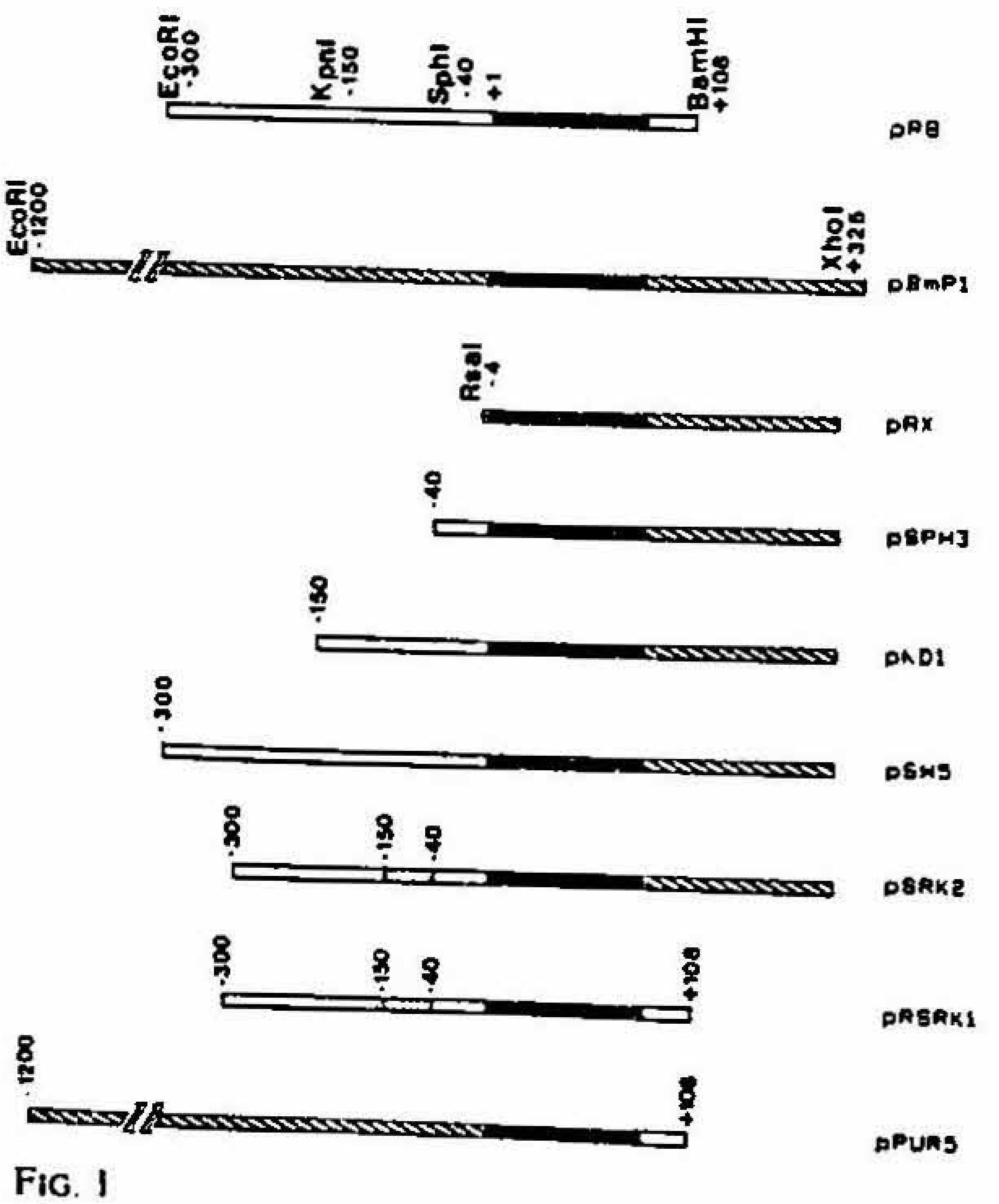

FIG. 1

negative element was moved closer to the coding region in the 5′ upstream location, the level of transcription was severely depressed in both pBmP1 and pR8. Thus the effect of the negative element appears to be distance dependent. The clone pPUR5 (in which the 3′ flanking sequences of pBmP1 were replaced by those of pR8) was efficiently transcribed and at much higher levels than the parental pBmP1. This was expected due to the elimination of the 3′ negative element. However, the transcription was still lower than pR8. The coding and 3′ flanking sequences of pR8 and pPUR5 being identical the lower transcription of pPUR5 was presumably due to the 5′ negative element in pBmP1 being closer to the coding region (–231 to –237) as compared to pRB (between –270 and –276).

To determine whether the downstream negative element of pBmP1 blinds the same nuclear factors as the previously identified negative element of pR8, gel retardation assays were carried out. The assays were done using either the negative element of pR8 as a probe and the negative element of pBmP1 as a competitor, or *vice versa*. Clear competition in protein binding of each fragment by the other suggested that the factors binding to the upstream of pR8 and the downstream of pBmP1 are the same.

The transcription of the *t*RNA$_1^{Gly}$ genes in heterologous systems such as the nuclear extracts from the middle silk gland (MSG) or pupal ovaries was also examined. Generally these extracts were less active in transcription as compared to the PSG nuclear extracts. In all the extracts the clone pR8 was transcribed to the highest levels *in vitro*. The relative efficiencies of transcription of the other *t*RNA$_1^{Gly}$ genes in all the extracts were the same.

References

1. Garel, J. P., Mandel, P., Chavancy, G. and Daillie, J.	*FEBS Lett.*, 1970, 7, 327–329.
2. Fournier, A., Guerin, M. A., Corlet, J. and Clarkson, S.G.	*EMBO J.*, 1984, 3, 1547–1552.
3. Taneja, R., Gopalkrishnan, R. and Gopinathan, K. P.	*Proc. Natn. Acad. Sci. USA*, 1992, 89, 1070–1074.

Thesis Abstract (Ph.D.)

Studies on the molecular mechanism of action of 5-fluorouracil: Altered functions of 5-fluorouracil substituted transfer RNA from rat liver by V. V. Suryanarayana

Research supervisor: R. Nayak
Department: Microbiology and Cell Biology

1. Introduction

5-Fluorouracil (FUra), an analogue of thymine and uracil, has been widely used either singly or in combination with other anticancer drugs in the treatment of a variety of cancers[1]. On the one hand, it is converted to FdUMP causing an irreversible inhibition of DNA synthesis[2], and on the other, it is converted to FUTP and incorporated into RNA[3–4], thereby affecting several vital cellular functions. Substitution of FUra into bacterial *t*RNA known to cause different degrees of inhibition of aminoacylation and changes in the base composition of uridine-derived bases. Little is known about the effect of FUra substitution into *t*RNA of eukaryotes, especially mammals. We examined the mechanism of action of FUra substitution into *t*RNA taking rat liver as the model system.

2. Materials and methods

Male Wistar rats of 2–3 months old were used throughout the study. Methods have been developed to purify *t*RNA with good yield and purity. FUra-substituted *t*RNA was isolated from rats injected i.p. with 50, 250 and 500 mg/kg of FUra. FUra-substituted *t*RNA was separated from unsubstituted *t*RNA using a concave gradient of NaCl (0.325–0.6 M) on DEAE–sephacel column[5]. FUra-substituted *t*RNA was identified by [^{3}H]-labelled marker (yeast) *t*RNA.

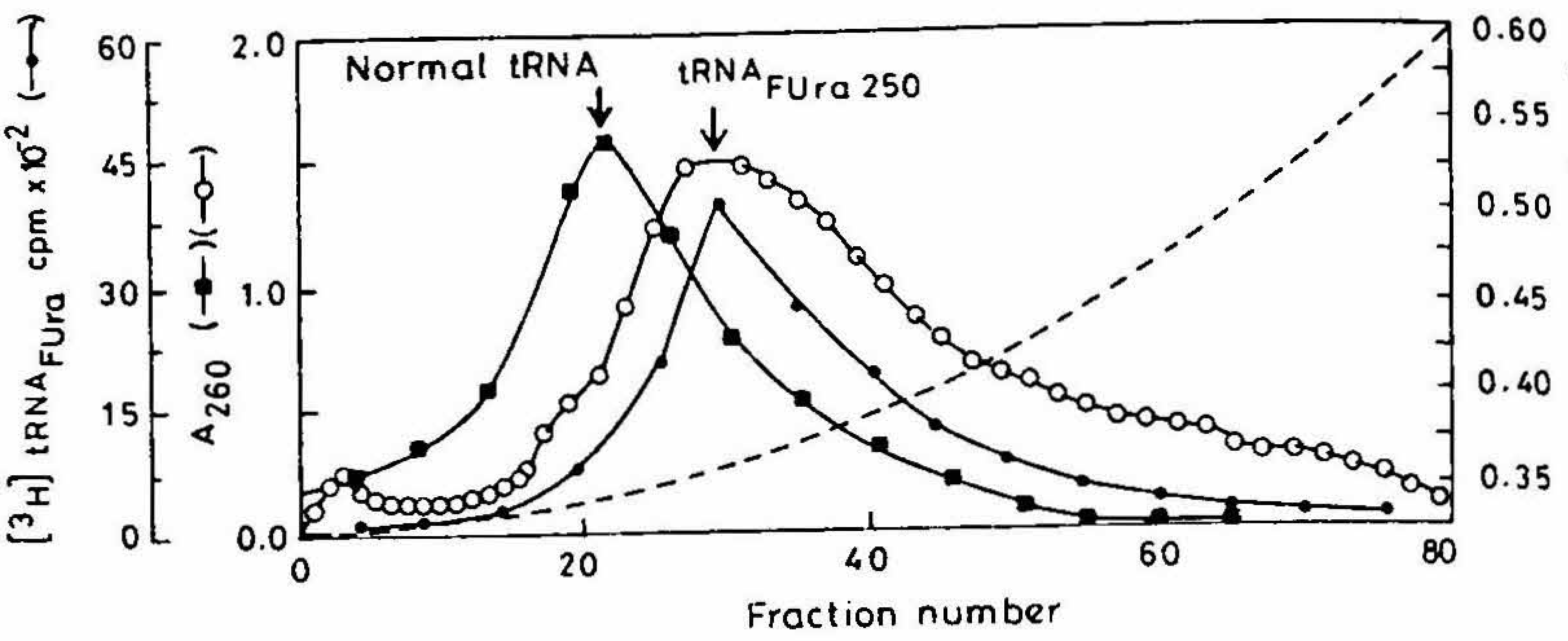

FIG. 1. Separation of rat liver FUra-substituted *t*RNA from unsubstituted *t*RNA by DEAE-sephacel chromatography.

Approximately 200 A$_{260}$ units of FUra–*t*RNA isolated from FUra-injected rats (250 mg/kg body wt) was applied on to a DEAE-sephacel (1.5 × 10 cm) column, in 20 mM Tris-HCl buffer pH 8.9 and 0.325 M NaCl and washed with the same buffer till the absorbance reached the base line.The bound *t*RNA was eluted (--0--) with an upward concave gradient (----) of NaCl (0.325–0.6 M) in the same buffer. Total normal rat liver *t*RNA (---■--) and marker[^{3}H]*t*RNA$_{\mathrm{FUra}}$ (--●--) from yeast were chromatographed in separate experiments, under similar conditions of elution. The flow rate of the column was 8–10 ml/h and fraction size was 2 ml.

Total aminoacyl–*t*RNA synthetases (AARS) were isolated using polyethylene glycol precipitation followed by DEAE–sephacel chromatography[6]. AARS were also isolated from *E. coli* for identifying initiator *t*RNA. A column chromatographic method using Mono Q column has been devised for fractionation of *t*RNA followed by 20% polyacrylamide-7M urea gel electrophoresis. FUra-substituted initiator *t*RNA was purified using normal initiator *t*RNA as a marker on polyacrylamide–urea gel. Thermal denaturation studies[7] and the effect of anti-*t*RNA antibodies on aminoacylation activity of normal and FUra-substituted *t*RNA[8] were carried out.

3. Results and discussion

Total *t*RNA isolated by DEAE-sephacel chromatography was found to be better in yield and activity compared to other protocols. FUra-substituted *t*RNA eluted towards slightly higher concentration of NaCl on DEAE-sephacel column (Fig. 1). It was observed that injection of therapeutic dose (50 mg/kg body wt) of Fura showed an increased acceptance for aspartic acid, serine, tryptophan, lysine, arginine and methionine. There was a decrease in the aminoacylation with increasing FUra dose for several of these individual amino acids indicating a common mechanism of action.

The melting profiles of rat liver *t*RNA showed a T_m of 63°C for normal *t*RNA, while *t*RNA isolated after injecting 50, 250 and 500 mg/kg body wt FUra showed 69, 71 and 71°C, respectively. Fura could behave like cytosine in *t*RNA and instead of base pairing with adenine it could base pair with guanine with three hydrogen bounds. The increase in the T_m implies a more rigid structure of the *t*RNA molecule due to more hydrogen bonds formed after FUra substitution.

In another experiment, total normal *t*RNA or FUra-substituted *t*RNA was preincubated with anti-RNA antibodies followed by the addition of total rat liver aminoacyl– *t*RNA synthetases. There was about 41% inhibition in the aminoacylation of *t*RNA isolated with 50 mg/kg body wt of FUra. The anti-*t*RNA antibodies failed to inhibit aminoacylation of *t*RNA isolated with 250 and 500 mg/kg body wt of FUra. It could be possible that with the incorporation of more FUra into *t*RNA the secondary structure of *t*RNA might have changed leading to an altered conformation. Since the anti-*t*RNA antibodies recognise the conformation of *t*RNA also, an altered conformation of *t*RNA might be a reason for the failure of the antibodies to recognize the *t*RNA with increased substitution of FUra. FUra-substituted initiator *t*RNA isolated under alkaline pH conditions showed 109 and 75% more acceptance of $[^{35}S]$methionine over normal initiator *t*RNA with doses of 50 and 250 mg/kg body wt of Fura, respectively, by *E. coli* AARS, while a dose of 500 mg/kg body wt inhibited the aminoacylation with methionine completely.

4. Conclusions

In the present study it was observed that the substitution of 5-fluorouracil into *t*RNA resulted in a functional alteration in the acceptance of total as well as several of the individual amino acids. It was observed that *t*RNA isolated from rats injected with increasing doses of Fura showed increase in T_m indicating a probable alteration in the secondary structure of the transfer RNA. This was supported by failure of anti-*t*RNA antibodies to recognise the total *t*RNA isolated with higher doses of FUra. FUra-substituted initiator *t*RNA isolated from rat liver showed increased acceptance of methionine at lower doses of FUra, but tended to decrease at higher doses, with the activity being completely abolished at toxic doses, implying a dose-dependent alteration in the conformation of initiator *t*RNA

References

1. Heidelberger, C. — Chemical carcinogenesis, chemotherapy: Cancer's continuing core challenge, *Cancer Res.*, 1970, **30**, 1549–1569.
2. Hartman, K. V. and Heidelberger, C. — Studies on flourinated pyrimidines, *J. Biol. Chem.*, 1961, **236**, 3006–3013.
3. Nayak, R., Martin, D., Stolfi, R., Furth, J. and Speigelman, S. — Pyrimidine nucleosides enhance the anticancer activity of 5FU and augments its incorporation into nuclear RNA, *Proc. Am. Assoc. Cancer Res.*, 1978, **19**, 63.
4. Speigelmann, S., Sawyer, R., Nayak, R., Ritzi, E., Stolfi, R. and Martin, D. — Improving the antitumor activity of 5-fluorouracil by increasing its incorporation into RNA *via* metabolic modulation, *Proc. Natn. Acad. Sci. USA*, 1980, **77**, 4966–4970.
5. Kaiser, I. I. — Studies on 5-fluorouracil containing ribonucleic acid. I. Separation and partial characterization of fluorouracil containing transfer ribonucleic acids from *Escherichia coli*, *Biochemistry*, 1969, **8**, 231–237.
6. Siddiqui, F. A. and Yang, D. C. H. — Generation of multiple forms of methionyl-*t*RNA synthetases from the multi-enzyme complex of mammalian aminoacyl-*t*RNA synthetases by endogenous proteolysis, *Biochem. Biophys. Acta*, 1985, **828**, 177–187.
7. Stein, A. and Crothers, D. M. — Conformational changes of transfer RNA. The role of magnesium (II), *Biochemistry*, 1976, **15**, 160–168.
8. Vaishnav, Y. N. and Antony, A. — Binding of deoxyadenylate and deoxycytidylate antibodies to double stranded DNA, *Biochem. Biophys. Res. Commun.*, 1988, **154**, 118–123.

Thesis Abstract (Ph.D.)

Analysis of some unsteady laminar boundary-layer flows using numerical methods

by M. Sathyakrishna

Research supervisors: G. Nath, A. Chakrabarti and S. Balachandra Rao

Department: Mathematics

1. Introduction

In recent years unsteady flow problems have received wider attention because of their importance in a number of applications in the fields of aerodynamics and hydrodynamics. This thesis presents the analysis of the numerical studies of some unsteady laminar incompressible boundary-layer flow problems. It consists of five chapters. The first chapter deals with a general introduction to boundary-layer theory. In the remaining chapters four different problems are considered: (i) unsteady two-dimensional and axisymmetric flows with an applied magnetic field, (ii) unsteady flow over a moving wall with an applied magnetic field, (iii) unsteady three-dimensional stagnation point flows over a stretching surface, and (iv) unsteady forced convection flow over an infinite rotating disk.

2. Problem formulation

The partial differential equations governing the flow, along with appropriate boundary conditions are written in the dimensional form based on certain assumptions. In the first problem the free stream velocity varies with stream-wise location as well as with time, while the wall temperature varies with time only. In the second problem, the motion of the wall is considered to be time dependent/impulsive. In the third problem the velocity components of the stretching surface and the free-stream velocity vary arbitrarily with time. In the last problem, the angular velocity of the rotating disk and the free stream velocity are time dependent. Using appropriate similarity transformations these equations are transformed into nondimensional form to obtain self-similar, semi-similar, or nonsimilar solutions.

3. Method of solution

The nonlinear equations governing the flow are first linearised using quasilinearisation technique. Then the resulting linear equations are descritised using implicit finite-difference scheme. They are further expressed in the matrix form with a block tri-diagonal structure, which is solved using Varga's algorithm.

4. Results and discussion

Results have been exhibited in the form of tables and graphs. Results of particular cases of these problems have been compared with the available results[1-5]. The effects of various parameters on skin friction, heat transfer, velocity and temperature profiles are considered for the above problems.

In the problem of flow over a cylinder or a sphere[1,6], the skin friction and heat transfer are found to be strongly influenced by the magnetic field and surface mass transfer. The variation in wall temperature affects the heat transfer only.

In the problem of flow over a moving wall[3], the effect of magnetic field is to increase the skin friction and heat transfer. In the impulsive motion case the ultimate steady-state values and the period of transition are affected by the magnetic field. The viscous dissipation prolongs the transient behaviour of the flow.

In the problem of flow over a stretching surface[3], the stretching ratios are found to affect both velocity and thermal field. The skin friction coefficients decrease, whereas the heat transfer increases, when the stretching ratios are positive. Exactly reverse happens when the stretching ratios are negative. The skin friction and heat transfer values are less for a three-dimensional body, when compared with the corresponding values for an axisymmetric body.

In the problem of flow over a rotating disk[4,5], the effect of mass transfer on primary and secondary velocity fields and the thermal field are analysed. The secondary boundary layers are observed to be thicker than the primary boundary layers. The effect of suction is to decrease the boundary-layer thickness, while injection increases the same.

The velocity as well as thermal fields are influenced by the unsteadiness. However, the effect of time on heat transfer is less, when compared to its effect on skin friction.

References

1. Surma Devi, C. D. and Nath, G. — Unsteady non-similar laminar boundary flows with heat and mass transfer, *Acta Technica CSAV*, 1983, 225–239.
2. Tsou, F. K., Sparrow, E. M. and Goldstein, R. J. — Flow and heat transfer in the boundary layer on a continuous moving surface, *Int. J. Heat Mass Transfer*, 1976, **10**, 219–235.

3. Libby, P. A.	Wall shear at a three-dimensional stagnation point with a moving wall, *AIAA J.*, 1974, **12**, 408–409.
4. Cochran, W. G.	The flow due to a rotating disk, *Proc. Cambridge Phil. Soc.*, 1934, **30**, 365–375.
5. Rott, N. and Lewellen, W. S.	Boundary layers due to the combined effects of rotation and translation, *Phys. Fluids*, 1967, **10**, 1867–1873.
6. Schlichting, H.	*Boundary layer theory*, 7th edn, 1979, McGraw-Hill.

Thesis Abstract (Ph.D.)

Numerical investigations of unsteady incompressible boundary-layer flows by A.T. Eswara

Research supervisors: G. Nath and A. Chakrabarti

Department: Mathematics

1. Introduction

The concept of boundary layer, presented by Ludwig Prandtl[1], makes it possible to think intelligently about almost any problem in the real fluid flow. Indeed, Prandtl's theory of boundary-layer flows has become a corner stone in the development of modern fluid mechanics and its allied branches of science, engineering and technology.

Although the boundary-layer theory was first developed for steady laminar flows, it was soon realized that most flow problems encountered in many practical applications are unsteady in nature. Unsteadiness can occur due to the time-dependent body motion or disturbances in the surrounding fluid medium and also due to transient motion of a body or sudden change in the temperature difference between the wall and the free stream. In the study of unsteady flows the introduction of time as an additional variable in the flow complicates the analysis[2]. But with the progress of numerical methods and computational techniques the unsteady boundary-layer computation gained momentum[3] and has become an important, self-standing subfield in fluid mechanics and heat-transfer research.

2. Present investigation

The prime object of present investigation is to obtain numerical solutions of certain problems in unsteady, incompressible laminar boundary-layer theory. The first problem deals with unsteady, mixed convection flow at a three-dimensional stagnation point with large injection rates. In the second problem the effects of variation of viscosity and Prandtl number with temperature on the unsteady, nonsimilar two-dimensional and axisymmetric flows have been investigated. The third problem is a study of the unsteady, MHD flow with heat transfer due to a point sink. The last problem presents an analysis of the unsteady, forced convection flow over a moving longitudinal cylinder. In all the above-mentioned problems the effects of various parameters such as unsteadiness, massive blowing, suction, magnetic field and viscous dissipation on the skin friction and heat-transfer coefficients as well as on the velocity and temperature fields have been studied in detail.

3. Methods of solution

Due to the nonlinearity and split two-point nature of the boundary conditions the boundary-layer equations governing the flow situations in the above problems have been solved by numerical methods. Among the popular numerical methods that are available today the finite-difference scheme are fast, efficient and well suited to boundary-layer problems. In the present work all the problems, except the first one, have been solved by using an implicit finite-difference scheme (involving constant step size) in combination with quasilinearization technique[4]. In the first problem, where the effect of large rates of injection is considered, the quasilinear implicit finite-difference scheme with variable step size has been used in the nodal point region. The reason for using a variable step size is that it keeps the stability of the numerical scheme[5]. However, this method fails to converge in the saddle point region due to the occurrence of reverse flow in one of the components of velocity. In order to overcome this difficulty, the parametric differentiation with implicit finite-difference scheme has been used.

4. Results and conclusions

Both semi-similar and locally, self-similar solutions and also a formal asymptotic solution for the locally self-similar case have been obtained for the problem of unsteady mixed convection flow at a three-dimensional stagnation point with large injection rates. From the results it is observed that both skin friction and heat transfer reduce considerably with the injection of large amount of fluid. The velocity and temperature fields are strongly affected by the buoyancy force and large injection rates. The location of dividing streamline is pushed away from the boundary due to large injection rates but the buouyancy force tends to bring it nearer the boundary. Dual solutions for the locally, self-similar steady flow are found to exist for both, buoyancy assisting and buoyancy opposing flows. The asymptotic solution, obtained by an approximate method, is found to be in good agreement with the numerical solution only when the rate of injection is large.

The temperature-dependent viscosity anad Prandtl number, in the case of unsteady two-dimensional and axisymmetric nonsimilar water boundary-layer flow, are found to have pronounced effect on both skin friction to move upstream. However, the effect of the variable fluid properties is to move it downstream. In general, the results pertaining to variable fluid properties are found to differ, significantly, from those of constant fluid properties.

In the study of the unsteady, incompressible MHD flow due to a point sink two types of unsteadiness, *viz*., unsteady motion due to the free stream velocity distribution varying continuously with time and the transient motion arising due to an impulsive change either in the strength of the point sink or in the wall temperature, have been analysed. It is found that both the types of unsteadiness in the flow have a significant effect on the skin friction and heat transfer. The magnetic field increases the skin friction but reduces the heat transfer. The transient nature of the flow is active for short time or long time depending, respectively, on the impulse imparted on the strength of the point sink or on the wall temperature. The viscous dissipation prolongs the transient behaviour of the flow.

In the last problem, *viz*., unsteady forced convection flow over a moving longitudinal cylinder, it is observed that the results are crucially dependent on the nondimensional parameter which is the ratio of the cylinder velocity and the free stream velocity[7]. For the case of upstream moving cylinder it is found that the solutions exist only for a small range of this nondimensional parameter and further they are found to be nonunique in this region.

References

1. PRANDTL, L.	*Proc. Third Int. Math. Congr.*, Heidelberg 1904,484 (also, NACA TM-452, 1928).
2. POP, I.	*Unsteady laminar boundary layers*, 1983, Bucharest, Romania.
3. CEBECI, T.	*J. Fluid Mech.*, 1986, **163**, 129-140.
4. INOUYE, K. AND TATE, A.	*AIAA J.*, 1974, **12**, 558-560.
5. LIU, T.M. AND CHIU, H. H.	*AIAA J.*, 1976, **14**, 114-116.
6. YAKOVLEV, M. N.	NASA TT - F254, 1965.
7. ESWARA, A.T. AND NATH, G.	*Acta Mech.*, 1962, **93**, 13-28.

Thesis Abstract (Ph.D.)

Studies on quasiperiodic structures and Al–Li–Cu quasicrystals by V. S. K. Balagurusamy

Research supervisors : E. S. R. Gopal and V. Sasisekharan*
Department: Physics (*Molecular Biophysics Unit)

1. Introdution

Icosahedral quasicrystals, which were discovered nearly a decade ago by Shechtman *et al.*[1], to exhibit the crystallographically forbidden 5-fold symmetry are now found to occur in the alloys[2]. This has created a keen interest among workers[3,4]. The structural aspects of these unusual phases are investigated in the present thesis.

2. Finite-size effects in 1d quasiperiodic structures

The effect of finite size on the diffraction characteristics of 1d quasilattice has been studied. The normalized intensity (I/N^2) calculated for weak and strong peaks, nearer and farther from the origin of the reciprocal space is found to fluctuate. The shifts in the position of these peaks with the size of the quasilattice has been calculated. The weak peaks have larger fluctuations than the strong ones. In both the cases, the weak peaks behave differently from the strong ones[5]. These observations cannot be explained by finite-size effects known in the case of periodic lattices.

3. New method of generating 2d quasiperiodic tilings

Two-dimensional nonperiodic tilings with 5, 5, 10 and 10 mm symmetries, generated by inflating rhombuses circumventing the decision-making problem encountered in obtaining the Penrose tiling are discussed[6]. The decorations of the basic rhombuses have been generated to possess a centre-of-inversion at the edge-centres. Further, all the edges of both kinds of rhombuses are identical (Fig.1). The small and big rhombus decorations satisfying these conditions give rise to an inflation factor off ($\tau + 2$) and ($2\tau + 3$) with different variations among them. The ratio of the number of small rhombuses to that of big rhombuses tends to an irrational value τ in infinitely large tilings. The tilings fall into two classes, self-similar and non-self-similar. These tilings are shown to be quasiperiodic. Different features like the occurrence and non-occcurence of the stacking of similar kinds of rhsombuses have been observed. The relevance of these quasiperiodic structures in the actual growth of quasicrystals is pointed out.

4. Analysis of the X-ray data of Al_6CuLi_3 quasicrystal in terms of an approximate cubic cell

Subsequent to the earlier studies carried out in this laboratory on single-grain Al_6CuLi_3 quasicrystal with X-ray precession, Weissenberg and rotation photographs which indicated the possibility of a large body-centred cubic cell (dimension around 60 Å), the X-ray diffraction data collected from a single grain of the same quasicrystal using Arndt–Wonacott (flat-plate oscillation) camera with Cu-K_α radiation are analyzed in order to find more quantitatively how well the cubic-cell approximation describes the quasicrystalline data. The X-ray diffraction peaks were compared with the calculated reflections from the corresponding oscillation range expected for a body-centred cubic crystal. It is found that the approximate cubic-cell indices describe only about 65% of the experimentally observed peaks. This clearly shows that the cubic-cell description of Al_6CuLi_3 quasicrystal which is the core of the multiple-twinning model [7] is far from satisfactory. The Al_6CuLi_3 quasicrystal cannot thus be described satisfactorily by cubic-approximants as suggested by Dmitrienko[8].

5. Indexing the X-ray data to an icosahedral reciprocal space

It has been found that the conditions on the indices to remain integers under 5-fold rotations as given by Cahn *et al.* are not the most general ones. The X-ray diffraction data of Al_6CuLi_3 quasicrystal are analysed with a

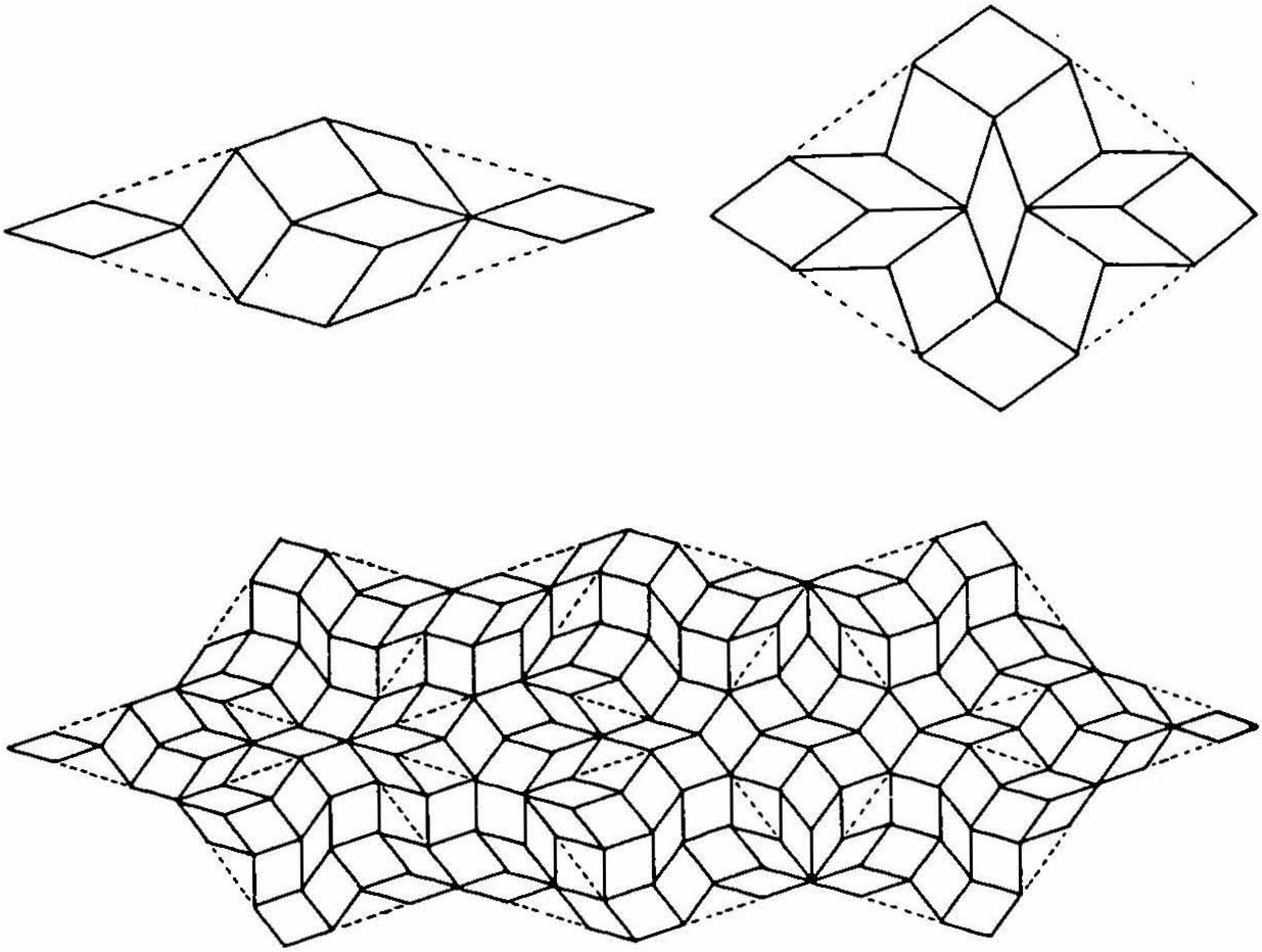

FIG. 1. Small (a) and big (b) rhombus decorations having cetre of inversion at the edge-centres. In addition, all the edges of both decorations are identical. Once inflated small rhombus (c) is also shown.

view to find out whether the icosahedral indices not satisfying Cahn *et al.*'s conditions but the more general ones described here would explain the data. A large number of indices are matching with each experimentally observed peak. The indices not satisfying Cahn *et al.*'s conditions also describe the X-ray diffraction peaks observed from Al$_6$CuLi$_3$ single-grain quasicrystal.

6. Conclusion

The studies on the effect of finite size on the diffraction characteristics of 1d quasilattices show that there are shifts in peak positions and fluctuations in peak intensities with varying size. These effects cannot be explained by the conventional finite-size effects known in the case of periodic lattices.

The decorations of the rhombuses have been arrived at such that they have a centre-of-inversion about their edge-centres and, in addition, all the edges of both kinds of rhombuses are identical. It is therefore possible to generate infinitely large quasiperiodic tilings by inflation/deflation method using unique decoration satisfying these conditions for each kind of rhombus by avoiding the decision-making problem at different stages of inflation. These structures seem to be relevant to the understanding of the actual growth of quasicrystals.

The best-fit dimension of the body-centred cubic cell incompletely describing the X-ray data of single-grain Al$_6$CuLi$_3$ is found to be 60.2 Å. This value is close to 57.8 Å recently arrived at by Pauling[7]. The analysis shows that the approximate cubic cell description which is the core of the multiple-twinning model[7] is able to account for only 65% of the observed peaks which is not adequate. In addition, it also clearly shows that the cubic-approximant description suggested by Dmitrienko[8] is far satisfactory for the quasicrystalline Al$_6$CuLi$_3$.

The more general conditions for the icosahedral indices to remain integers under 5-fold rotations not pointed out by Cahn *et al.*[9] have been discussed. The analysis of X-ray data of Al_6CuLi_3 single-grain quasicrystal in terms of icosahedral indices show that those not satisfying Cahn *et al.*'s conditions also describe the experimental peaks for the value of the scaling factor of the icosahedral reciprocal space (1/16.0 $Å^{-1}$) used here.

References

1. SHECHTMAN, D., BLECH, I. GRATIAS, D., AND CAHN, J. W. — *Phys. Rev. Lett.*, 1984, **53**, 1951–1953.
2. SURYANARAYANA, C. AND JONES, H. — *Int. J. Rapid Solidification*, 1987, **3**, 253–293.
3. STEINHARDT, P.J. AND OSTLUND, S. (eds) — *The physics of quasicrystals*, 1987, World Scientific.
4. JARIC, M.V. (ed.) — *Aperiodicity and order: introduction to quasicrystals*, 1988, Academic Press.
5. BALAGURUSAMY, V. S. K., BARANIDHARAN, S., GOPAL, E. S. R. AND SASISEKHARAN, V. — *Pramana*, 1990, **34**, 525–536.
6. BALAGURUSAMY, V. S. K., RAMESH, K. AND GOPAL, E. S. R. — *Physica B*, 1992, **179**, 249–256.
7. PAULING, L. — *Proc. Natn. Acad. Sci. USA*, 1989, **86**, 8595–8599.
8. DMITRIENKO, V.E. — *J. Phys.*, 1990, **51**, 2717–2732.
9. CAHN, J. W, SHECHTMAN, D. AND GRATIAS, D. — *J. Mater. Res.*, 1986, **1**, 13–26.

Thesis Abstract (Ph.D.)

Development of data processing techniques for laser Doppler velocimeter based flow measurements by K.T.Madhavan

Research supervisors: E. S. Raja Gopal, R. M. Vasu and K. S. Yajnik (NAL)
Department: Physics

1. Introduction

Schemes available for conditional sampling of data on the fluid velocity obtained in analogue form are generally applicable directly to the analogue data or to the digital data obtained by uniformly sampling the analogue data. For non-uniformly sampled digital data in the presence of noise, typical of a laser Doppler velocimeter (LDV), hardly any schemes are available, except those devised for very specific applications. The present work is concerned with the development and application of certain data-processing techniques for measurements in a turbulent flow using LDV. These schemes were designed for : (a) generation of a detector function (or intermittency function) for conditionally sampling the data on velocity obtained by LDV, and (b) determination of 'zone averages' corresponding to the turbulent and non-turbulent regions of the flow. Results of the detailed study and the application of the present schemes in an axisymmetric jet showed good comparison with results obtained by other schemes.

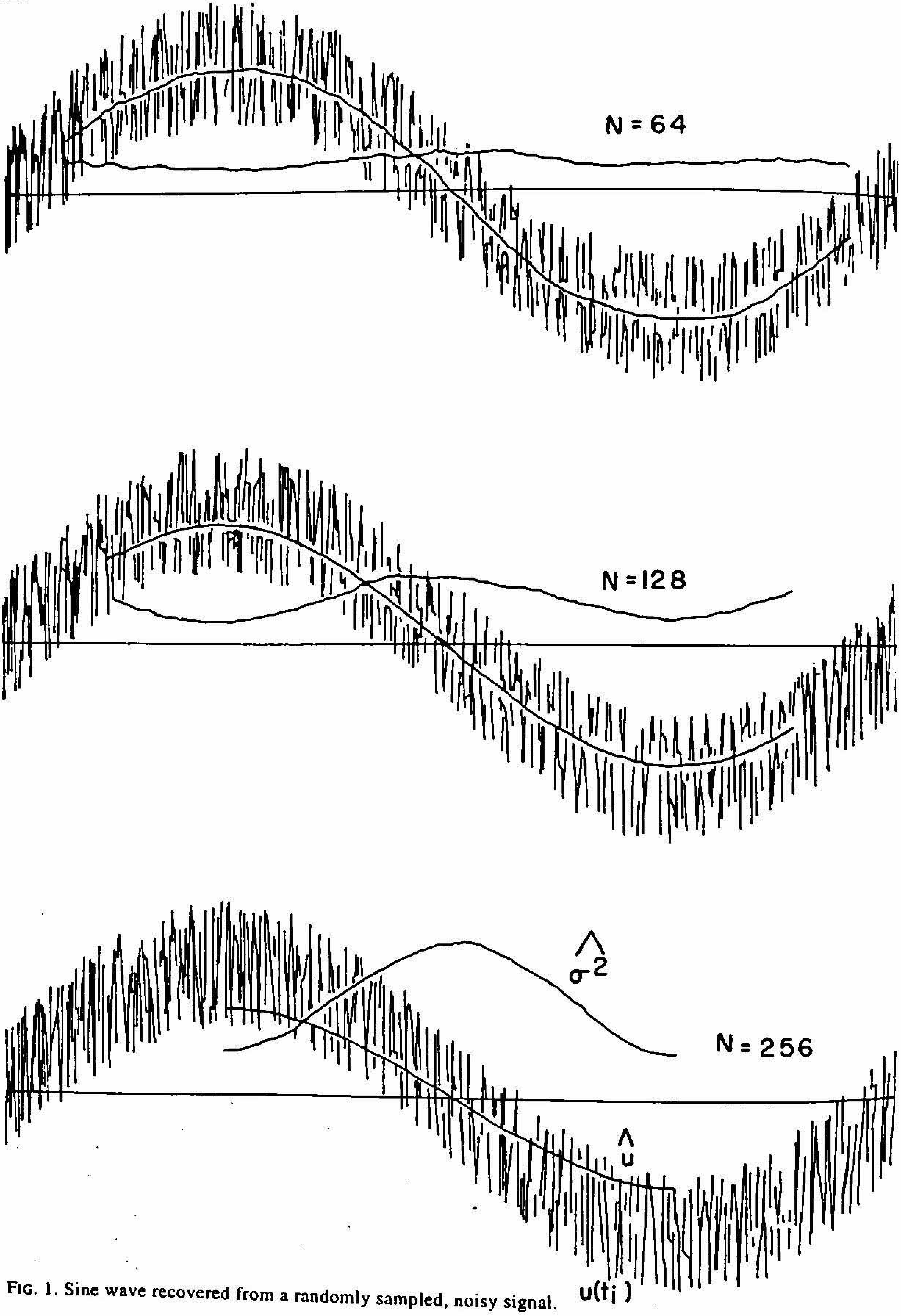

FIG. 1. Sine wave recovered from a randomly sampled, noisy signal.

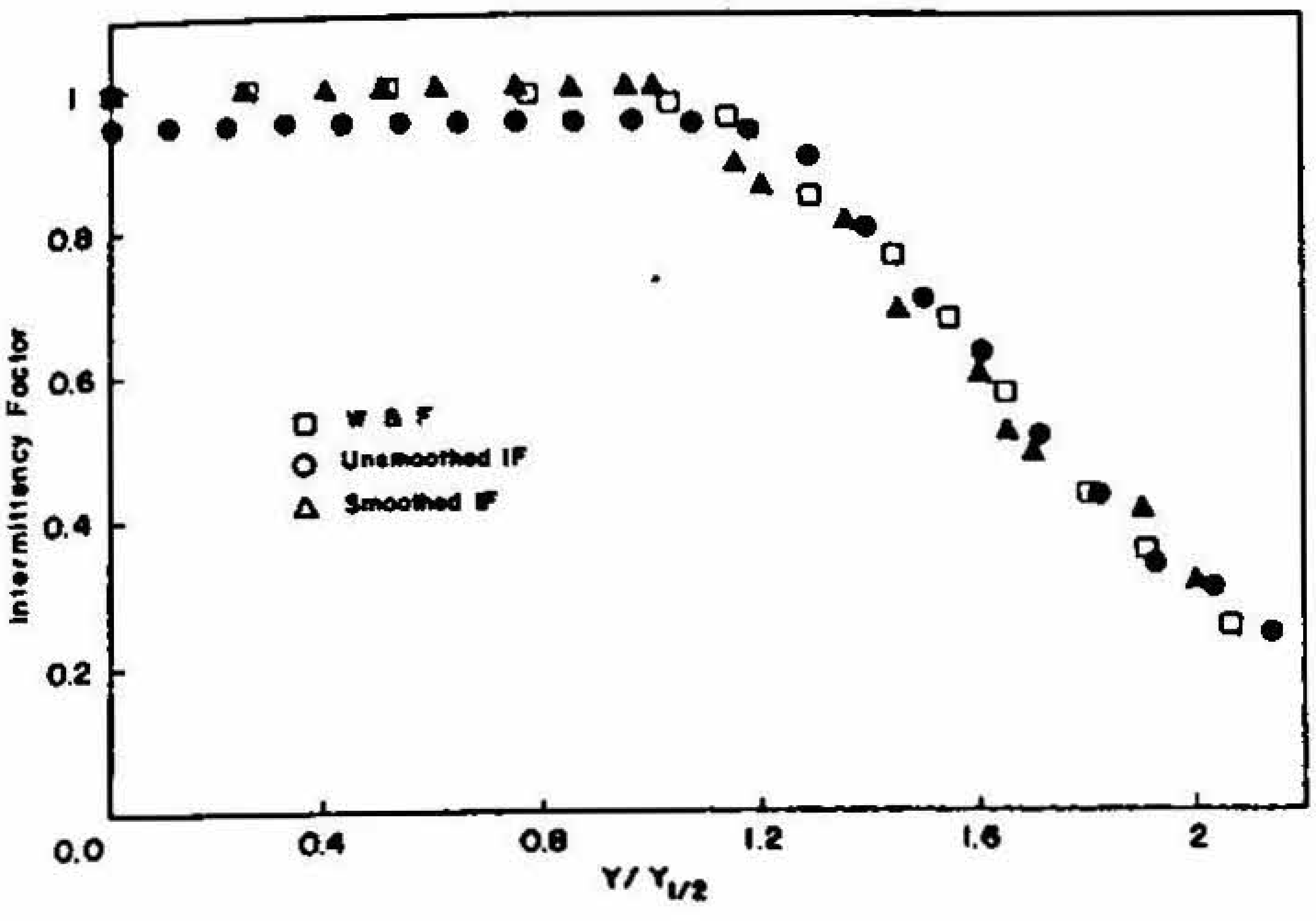

FIG. 2. Comparison of intermittency factors (using smoothed and unsmoothed IF).

2. Data-processing techniques

The data-processing schemes developed were mainly for (a) generation of an intermittency function, (b) smoothing, and (c) determination of zone averages. The intermittency function (IF), which distinguishes the turbulent regions of the flow, was generated as follows:

The instantaneous flow velocities and the time intervals between consecutive data realizations were first measured by LDV. A 'criterion function', representative of turbulence, is then generated by computing the second finite difference of the velocity samples. Spurious dropouts and spikes in IF occur due to uncertainties in the determination of the threshold crossings of the criterion function, non-uniformity and the presence of noise in LDV signals. In order to remove these effects, the criterion function is 'smoothed' by the application of a lowpass filter function. The criterion function is then compared with a threshold to generate IF.

A new scheme called 'variable window averaging' (VWA), similar to a moving window average, is used for the above filtering. It computes the short-time averages of the noisy signal and effectively retrieves signals of low frequency. The algorithm was evaluated by testing the response of a low frequency, discrete sinusoid with various intensities of noise. Figure 1 shows short-time averages ($\hat{u}$) and variances (σ^2) for three different averaging windows. It can be seen that, for averaging windows ≤ (1/16) of the total number of samples in one period, the basic sinusoidal component of the signal is very effectively retrieved.

The occasional 'zeros' or 'dropouts' in IF which occur even during the fully turbulent part of the flow are well known[2]. An approach to digitally smoothen the short-term aberrations in IF was developed[3]. The algorithm used for the digital smoothing involves the removal of (a) isolated 'dropouts' (for number of dropouts ≤ 2) in a continuous string of 1s and (b) isolated 'spikes' (for number of spikes ≤ 2) in a continuous string of 0s.

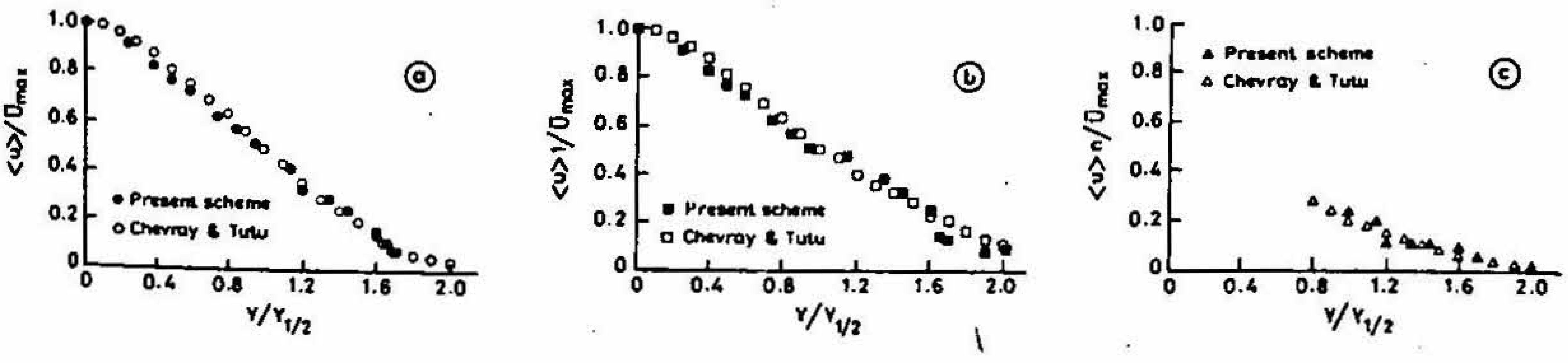

FIG. 3. Conditionally averaged mean velocity profiles.

Using IFs and intermittency factors obtained with the above scheme, a method was developed to determine the 'zone averages' corresponding to the turbulent and non-turbulent regions of a flow.

3. Validation of the schemes

The data-processing schemes were evaluated for the test case of an axisymmetric jet. The choice of this flow configuration was made from the consideration of the importance of conditional sampling techniques in free shear flows like an axisymmetric jet. 'Zone averages' in the self-preserving region of the jet were determined and compared with the results obtained by other methods. Figure 2 shows the comparison of the intermittency factors obtained using the present technique (with unsmoothed and smoothed IFs) and those obtained by Wygnanski and Fidler using hot wire in a similar experiment[3,4] (Y: radial distance, $Y_{1/2}$: jet half-width). Figure 3 shows a comparison of the normalized zone-averaged values corresponding to the turbulent zone ($<u>_t/\overline{U}_{max}$), non-turbulent zone ($<u>_n/\overline{U}_{max}$) and the conventional ($<u>/\overline{U}_{max}$) mean velocities with those obtained by Chevray and Titu[5,6] using 'temperture scheme'. The higher values of axial mean velocities in the turbulent zone with respect to the conventional can be seen to be in good agreement.

The distribution of sample intervals (the time intervals between *valid* LDV data) was also examined. It has been reported in the literature that the arrival rates of scattering particles in the measurement volume follow a Poisson process. It is known that the 'inter-arrival rates' for such a process are exponential. In the present work, the experimentally observed distribution of the inter-arrival rates is approximately exponential subject to certain restrictions.

4. Conclusion

This work describes the development and evaluation of new data-processing techniques for turbulent flows using LDV. An interesting implication is the possibility of conditionally sampled turbulence measurement using *only* a single-component LDV.

References

1. MADHAVAN, K.T., YAJNIK, K.S. AND JAYAVINAYAKA, S. — Variable window averaging for LDV data processing, *Workshop on Application of LDV to Flow Measurements*, NAL, May 29-31, 1990.
2. MUCK, K.C. — *Comparison of various schemes for the generation of the turbulence intermittency function*, Imperial College Aero. Report, No. 80-03, 1980.
3. MADHAVAN, K.T. AND YAJNIK, K.S. — Measurement of turbulence intermittency with a single-component LDV, *Proc. 4th Int. Symp. on Laser Anemometry*, Ohio Aerosp. Inst., Aug. 5-9, 1990, Vol. 3, pp. 23-26.
4. WYGNANSKI, I. AND FIEDLER, H.E. — Some measurements in the self preserving jet, *J. Fluid Mech.*, 1969, 38, 577–612.
5. MADHAVAN, K.T. AND YAJNIK, K.S. — Conditional sampling techniques for LDV data processing, *Proc. 6th Int. Symp. on Application of Laser Tech. to Fluid Mech.*, Instituto Superior Tecnico, Lisbon, July 20–23, 1992.
6. CHEVRAY, R. AND TUTU, N.K. — Intermittency and preferential transport of heat in a round jet. *J. Fluid Mech.*, 1978, 88, 133–160.

Thesis Abstract (Ph.D.)

Applications of coupled-mode theory to fiber and integrated optic waveguide structures by Talabattula Srinivas

Research supervisor: A. Selvarajan
Department: Electrical Communication Engineering

1. Introduction

In the present work Coupled-Mode Theory (CMT) of optical waveguides is[1,2] applied to tackle some important and novel problems in fiber and integrated optics. CMT is concerned with the interaction among a number of waveguides. From application point of view, converse is also profitable, *i.e.*, considering the given complicated waveguide problem in terms of simpler ones. Here, the contribution has been made to three different classes of applications—multiple waveguide coupling, light propagation in thin-clad fiber[3] and inclined waveguide coupling. The work is semi-theoretical in nature, in that, emphasis is put on reducing the results to practical waveguide configurations, rather than mathematical generalizations.

2. CMT

A comprehensive discussion on various aspects of CMT is covered following the introduction. Starting with historical notes, the coverage includes the coupled-mode approaches to waveguide problems, various methods of deriving the coupling coefficients, applications and, criticism on approximation and applicability issues. A simple improvement to conventional CMT that uses the scalar wave equation is derived, and generalised as below:

$$\frac{dU}{dz} = -i(B + M^{-1}L)U,$$

where U is the optical mode field and,

$$\begin{aligned} M &= \{M_{pq},\ p,q=1 \ldots N\}, \\ L &= \{L_{pq},\ p,q,=1 \ldots N\}, \\ U &= \text{column matrix } \{U_p,\ p=1 \ldots N\} \\ \beta &= \text{diagonal matrix } \{\beta_p\, p=1 \ldots N\} \end{aligned}$$

$$\begin{aligned} M_{pq} &= \int \psi_p^* \psi_q \, ds \\ L_{pq} &= \int \Delta n^2 \psi_p^* \psi_q \, ds. \end{aligned}$$

Numerical computations are presented to compare and comment on a wide spectrum of coupling conditions. Various combinations of two-mode coupling situations are considered. Major among them are strongly and weakly coupling geometries coupling between strongly and weakly guiding modes, and coupling between symmetric and asymmetric waveguides.

Multiple wave guide problems are the standard motivation for CMT. Here coupling between three parallel fibers is studied. Coupled-mode equations are solved for different initial waveguide excitations. Comparison with two fiber directional coupler is done. Possible application to multiport couplers, as an extension to common four port directional coupler, is suggested. The use of recently formulated CMT is the additional contribution here.

3. Thin-clad fiber

General interest in doubly clad fiber is due to its improved dispersion characteristics. Here a thin clad fiber is viewed as being derived from a normal infinite clad fiber by removing a major portion of the cladding. Most current fiber-based devices employ a bare unclad fiber. A thin cladding may be recommended for several reasons, like protection or core geometry, stability of propagating modes, or necessity of application. Here light propagation in thin-clad fiber is solved as a coupled-mode problem by decomposing it into hypothetic infinite clad fibers (Fig.1). Such an approach is totally alien to multiple waveguide coupling, even though it

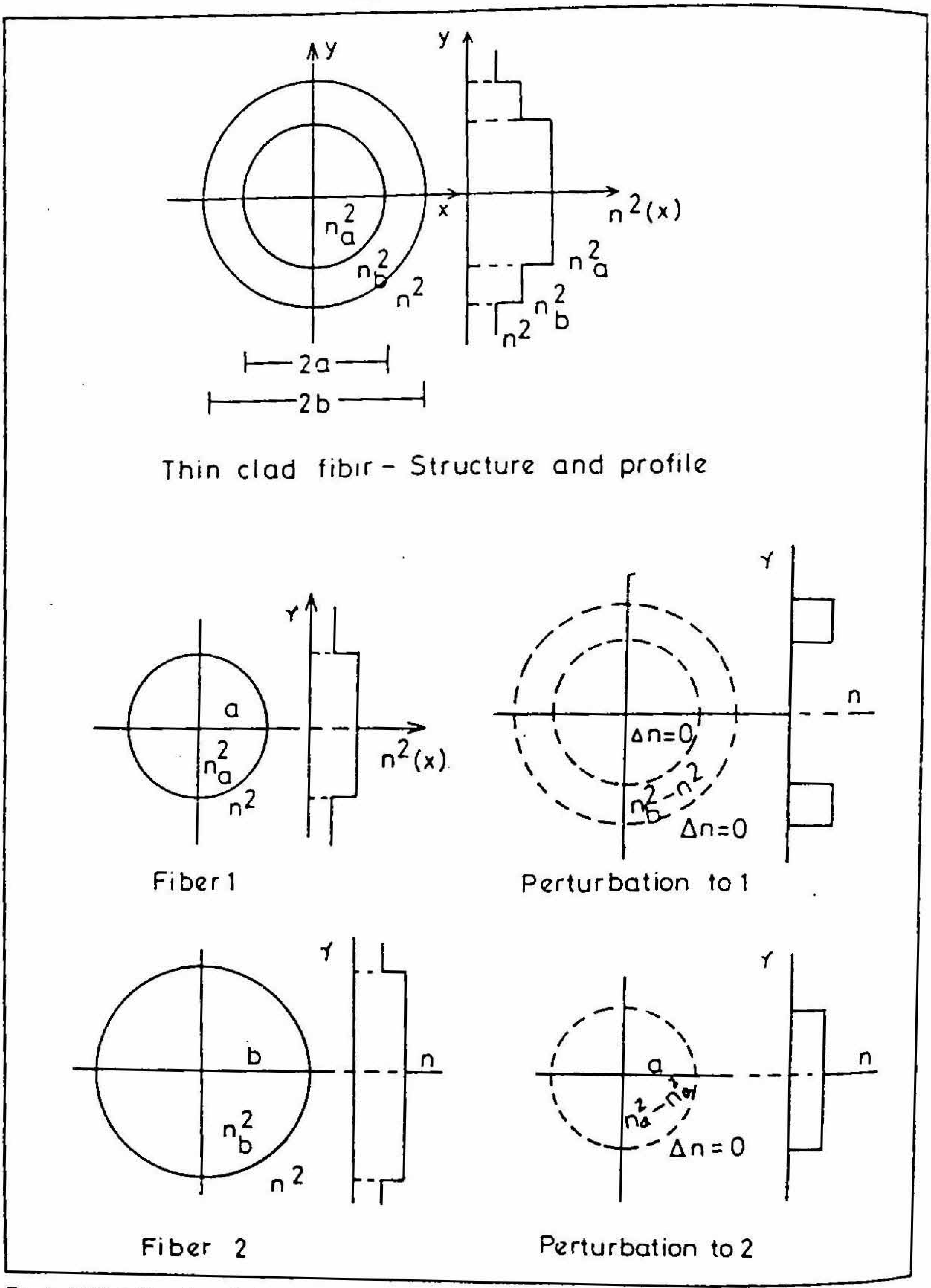

Thin clad fibir - Structure and profile

Fiber 1

Perturbation to 1

Fiber 2

Perturbation to 2

FIG. 1. TCF problem formulation.

satisfies the requirements of CMT, *i.e.*, splitting the refractive index profile in terms of simpler ones and their perturbations. To support the approach the problem is solved directly using appropriate Bessel functions in each of the regions. Necessity to use recently formulated improved CMT is demonstrated by this example.

4. Inclined waveguide couplers

Modal analysis of straight waveguides is an approach to simplify wave propagation problems, by reducing the wave equation to a two-dimensional partial differential equation. When it comes to propagation in non-parallel or curved waveguides, the method is still employed to approximate the propagating fields, making use of normal mode analysis. In the present work, a CMT applicable to inclined waveguides is derived. Each of the coupling waveguides is represented in a separate co-ordinate system and the coupling is considered along an axis in a common co-ordinate system. This way new sets of coupled mode equations are derived that contain coupling coefficients with meanings different from the conventional straight waveguide coupling coefficients. The fields are given by

$$|U_a| \cong \cos\left\{\frac{K}{a_c \tan\theta}\left(1-e^{-za_c \tan\theta}\right)\right\} \text{ and } |U_b| \cong \sin\left\{\frac{K}{a_c \tan\theta}\left(1-e^{-za_c \tan\theta}\right)\right\}.$$

The formulation is applied to simple cases of coupling between inclined waveguides having specific features. The results follow expectations, that the power exchange reduce non-periodically as the waveguides separate out. Comparisons are done with existing theory of inclined waveguide coupling based on CMT of parallel waveguides. The application of standard beam propagation method (BPM) also compares favourably with the theory for specific examples. A full design of a practical directional coupler that includes the inclined portions is also suggested.

5. Conclusion

Applicability-related issues involving CMT of fiber and integrated optics are critically examined. It is commented that a number of possible avenues for further improvements still remain. Some of them are disclosed here, notable among them being the CMT for coupling guided to radiation modes and CMT to study propagation in curved optical waveguides.

References

1. YARIV, A.	Coupled mode theory for guidedwave optics, *IEEE J.*, 1973, **QE-9**, 919–933.
2. HAUS, H.A. AND HUANG, W.	Coupled theory, *Proc. IEEE*, 1991, **79**, 1505–1518.
3. SRINIVAS, T. AND SELVARAJAN, A.	Light propagation in thin-clad fibers, *Conf. on Emerging Optoelectronic Technologies*, SPIE Technical Conf., Bangalore, India, 1991.

Thesis Abstract (Ph.D.)
Dynamical and type 2 characterizations of ideal basis reduction in symbolic algebraic computation by Chandan Haldar
Research supervisor: L. M. Patnaik
Department: Computer Science and Automation

1. Introduction

The ideal basis reduction algorithms (known as Gröbner and standard basis reduction[1,2]) in symbolic algebraic computation have recently emerged as powerful decision procedures with applications in a wide variety of areas. Unlike numerical methods, symbolic algebraic computation (also called computer algebra) works with infinite precision rational arithmetic, retains the algebraic and geometric structure of the problem provides symbolic solutions (sometimes for whole classes of problems) whenever possible, and contributes to the theoretical insight into the problem. For these reasons, computer algebra systems have become increasingly popular. In particular, application of the powerful basis reduction algorithms to various classes of computational problems is growing rapidly.

The complexity issues of the basis reduction algorithms, however, are known only to a limited extent. In general, the dynamics of these computations—the superexponential worst-case complexity, good efficiency in many practical instances, and the strange sensitive dependence of the length of computation on the *initial basis* and on the term ordering used—is poorly understood.

Recently, Blum *et al.*[3] have proposed a theory of computation over arbitrary ordered rings distinct from the classical theory of computation over the set of natural numbers **N**. In particular, they have developed notions of universal machines, recursive and recursively enumerable sets over a ring, and NP-completeness over the set of real numbers **R**. Related models of computation termed *type 2 models of computation* over uncountable sets have been investigated by Weihrauch[4].

In this thesis we study similar models of computation over polynomial and power series rings, and over countable products of these rings with themselves. Blum *et al.*'s model[3] aims primarily at using the tools of classical computation theory for characterizing computations in numerical analysis. The real number model of computation also makes it possible to use certain results in dynamical systems[5,6] in characterizing the dynamics of programs and their complexities. The model we describe provides a complementary framework in which algorithms in symbolic algebraic computation and their complexity can be characterized using tools similar to those used by Blum *et al.*[3] and the tools of the type 2 theory of computation.

2. Ideal basis reduction as discrete semidynamical system

In Blum *et al.*'s dynamical systems view of algorithms or machines, an algorithm is viewed as a mapping from an appropriate state-space to itself. This basic idea is to express the algorithm as a map (an endomorphism) of the state-space of the machine into itself.

Let us write the state-space for Buchberger's Gröbner basis reduction as $\mathcal{S} = \mathrm{N}^3 \times R^{\infty}$, where R is the ring, and N is the set of natural numbers. We write the $\mathcal{G}'$-map as $\mathcal{G}': S \to S$. Let $i,j,k \in \mathrm{N}$, and $x \in R^{\infty}$. Then define the map $\mathcal{G}'$ by

$$\begin{aligned}\mathcal{G}'((i,j,k,x)) = (&\mathcal{N}_i((i,j,k,x)), \mathcal{N}_j((i,j,k,x)), \mathcal{N}_k(i,j,k,x),\\ &\mathcal{N}((1,i,j,k,x)), \mathcal{N}(2,i,j,k,x),\ldots.)\end{aligned} \tag{1}$$

where

$$\mathcal{N}_i((i,j,k)) = \begin{cases} i & \text{if } i = k \text{ or } i < j < i, \text{ and } j < i \\ i+1 & \text{if } i < k \text{ and } j = i, \\ \text{undefined} & \text{in all other cases,} \end{cases} \tag{2}$$

$$\mathcal{N}_j((i,j,k)) = \begin{cases} j & \text{if } i = k \\ j+1 & \text{if } i < k \text{ and } j < i, \\ 1 & \text{if } i < k \text{ and } j = i, \\ \text{undefined} & \text{in all other cases,} \end{cases} \tag{3}$$

$$\mathcal{N}_k((i,j,k,x)) = \begin{cases} k & \text{if } i = k \text{ or } R_{sp}(i,j,k,x) = 0, \\ k+1 & \text{otherwise,} \end{cases} \tag{4}$$

$$\mathcal{N}((l,i,j,k)) = \begin{cases} R_{sp}(i,j,k,x) & \text{if } l = k, \\ x_l & \text{otherwise,} \end{cases} \tag{5}$$

and $R_{sp}(i,j,k,x_1,x_2\ldots.)$ is the reduced form of $Spoly(x_i,x_j)$.

Proposition 2.1. With the initial state-space value $(1, 1, p+1, x'_q, \ldots, x'_q, 0, \ldots)$, *the point* $(q+1, 1, q+1, x'_1, \ldots, x'_q, 0, \ldots)$ *is a fixed point of the* $\mathcal{G}'$*-map where* $\left\{x'_q, \ldots, x'_q\right\}, q \geq p$, *is a Gröbner basis of the ideal* $(x'_1, \ldots, x'_p)$.

If $\alpha : \mathbf{N}^2 \rightarrow \mathbf{N}$ is a function given by

$$a(i,j) = \prod_{r=0}^{i-1} \frac{j-r}{i-r},$$

$$a(i,j) = \begin{cases} 1 & \text{if } i = j, \\ 0 & \text{if } j < i. \end{cases} \tag{6}$$

Then we can express the functions $\mathcal{N}_i$, $\mathcal{N}_j$, $\mathcal{N}_k$ *and* $\mathcal{N}$ as follows.

$$\mathcal{N}((i,j,k)) = i + a(i,j)(1 - a(k,i)), \tag{7}$$

$$\mathcal{N}_j((i,j,k)) = (j+1)(1 - a(k,i))(1 -- a(i,j)) + j\, a(k,i) + (1 - a(k,i))a(i,j). \tag{8}$$

$$\mathcal{N}((i,j,k,x)) = k + (1 - a(k,i))(1 - \mathcal{N}(R_{sp}(i,j,k,x))). \tag{9}$$

$$\mathcal{N}((l,i,j,k,x)) = b(l,k)\, R_{sp}\, (i,j,k,x) + x_l\, (1 - b(l,k)), \tag{10}$$

where the function b: $\mathbf{N}^2 \rightarrow \mathbf{N}$ is the infinite extension of the function a used above, namely,

$$b(i,j) = \prod_{r \neq i, r \in \mathbf{N}} \frac{j-r}{i-r}, i, j, r \in \mathbf{N}.$$

Clearly,

$$b(i,j) = \begin{cases} 1 & \text{if } i = j, \\ 0 & \text{otherwise.} \end{cases} \tag{11}$$

This way, the $\mathcal{G}'$-map is reduced to an algebraic form modulo the ring operations Z and R_{sp}.

We get a metric and a topology (termed respectively the $\mathcal{G}$-metric and the $\mathcal{G}$-topology) on the state-space and on its projection R^{-}, using a numbering of the concerned ring. This makes it possible to study the structure of the $\mathcal{G}$-orbits in the Baire space **B** *via* a representation δ of R^{-} by **B**. Let δ' be the inverse of δ. Then we get the following results.

Lemma 2.2. The $\mathcal{G}$*-topology of* R^{-} *is the final topology of* R^{-} *relative to the representation* δ.

Theorem 2.3. Let $(z_0, z_1, \ldots)$ be the $\mathcal{G}$-orbit of the initial point z_0 in R^{-} under the group action of the $\mathcal{G}$-map. The δ' -image of the orbit $(z_0, z_1, \ldots)$ *in* **B** *is a Cauchy sequence under the Baire metric in* **B**.

Corollary 2.4. A $\mathcal{G}$*-orbit* $(z_0, z_1, \ldots)$ *in* R^{-} *is a Cauchy sequence in* R^{-} *in its final topology.*

Proposition 2.5. Every $x \in R^{-}$ *such that either* $length(x) = q < \infty$ *and* $\{x_1, \ldots, x_q\}$ *is an infinite Gröbner basis of some ideal* I *in* R *or* $length\ (x) = \infty$ *and* $\{x_1, \ldots, x_q\}$ *is an Gröbner basis of some ideal* I *in* R *is a fixed point of the* $\mathcal{G}$*-map in* R^{-}.

3. Type 2 basis reduction machines

In the type 2 model of computation, the three basic uncountable domains of computation are the set of all infinite sequences of natural numbers (Baire space), the set of all subsets of **N**, and the set of all infinite sequences of zeros and ones (the Cantor space). Other uncountable sets are reduced to one of these sets by *effective representations*. The basis reduction algorithms in polynomial and power series rings can be naturally viewed as computations over a countable product of the ring with itself. This makes it possible (using the $\mathcal{G}$-map) to characterize the basis reduction algorithms as type 2 machines.

4. Visualizing the Gröbner map

Preliminary experiments in visualizing the dynamics of basis reduction from within a Lisp-based computer algebra system running under UNIX are reported in the thesis for two variable case. The idea is to graphically plot the terms of polynomials as points in a two-dimensional plane. Redisplaying the basis after every iteration of the main loop in the Gröbner basis reduction algorithm results in an animated graphic display of the way in which the basis gets transformed into the Gröbner basis. Refer to the thesis for the graphical results.

References

1. BUCHBERGER, B. Gröbner bases: An algorithmic method in polynomial ideal theory. In *Recent trends in multidimensional systems theory* (N.K. Bose, ed.), pp. 184–232, 1985, D. Reidel.

2. MORA, T. *Seven variations on standard bases*, Preprint, University of Genova, 1989.

3. BLUM, L., SHUB, M. AND SMALE, S. On theory of computation over the real numbers; NP-completeness, recursive functions and universal machines, *Bull. Am. Math. Soc.*, 1989, **21**, 1–46.

4. WEIHRAUCH, K. *Computability, EATCS Monographs on Theoretical Computer Science* 9, 1987, Springer-Verlag.

5. DEVANEY, R. L. *An introduction to chaotic dynamical systems*, 1986, Addison-Wesley.

6. WIGGINS, S. *Global bifurcations and chaos*, Applied Mathematical Sciences 73, 1988, Springer-Verlag.

Thesis Abstract (Ph.D.)

A unified approach to solve the numerical intersection curve tracing problem in geometric modelling by K.Venugopal

Research supervisor: S.Sathiya Keerthi
Department: Computer Science and Automation

1. Introduction

A major problem in computer-aided geometric design (CAGD) using curved surfaces is the computation of a representation for the intersection curves between areas of geometric modelling and computer-aided design (CAD), such as boundary evaluation, *i.e.*, the conversion from constructive solid geometry (CSG) representation to a boundary representation (B-rep)[1], automatic generation of numerical control (NC) programs, etc. The accuracy required for the intersection curve computation depends on the application. A final CAD product generally has to go through various stages of refinement, with the intersection curve computed at one stage serving as part of the input for later stages. In applications requiring a lot of processing, a high accuracy is required. Reliability and good accuracy are also very important in boundary evaluation, one of the most important problems in solid modelling.

Computing the intersection curves of general surfaces is nontrivial, and except for special classes of algebraic surfaces like quadrics, planes, etc., analytical solutions do not exist for the intersection curve. For surfaces like bicubic patches, the geometric degree of the exact intersection could be as high as 324. So, in general we need to go in for numerical techniques to get an approximation to the intersection curves.

The type of representation of the surfaces has important consequences for the computation of the intersection curves. Popular schemes for representing a surface in R^3 are:

1. implicitly as $g(x^1, x^2, x^3) = 0$; or,
2. piecewise parametric equations over a bounded domain as $X(u,v) = [x^1(u,v), x^2(u,v), x^3(u,v)]$.

The easiest among the cases is when one surface is type 1 and the other is of type 2. Then by a simple substitution, the intersection curve is obtained as

$$g\,(x^1(u,v), x^2(u,v), x^3(u,v)) = 0.$$

A more difficult case is when both the surfaces are of type 1. The intersection curve has then to be obtained by the simultaneous solution of two nonlinear equations in three unknowns. The most difficult case is when both the surfaces are of type 2. The intersection curve is then defined as the solution of a system of three nonlinear equations in four unknowns. For a modeller incorporating both forms of representation the general intersection curve problem can be stated as follows:

Given $(n-1)$ *surfaces defined by* $g\,(x) = 0$, *where* $g : R^n \to R^{n-1}$, *find a parametric representation*, X, *for* $g^{-1}(0) = \{x : g\,(x) = 0\}$, *the curve of intersection.*

Depending upon the types of surfaces involved, n takes the values 2, 3 or 4. The problem as stated above is associated with the following three subproblems:

1. how do we determine one starting point on each of the connected components of $g^{-1}(0)$?
2. given one starting point, $x_0 \in g^{-1}(0)$, how should the connected component of $g^{-1}(0)$ containing x_0 be numerically traced ?
3. If $g^{-1}(0)$, is not a manifold, what should be done to tackle singularities, saddle points and other situations contributing to numerical instability?

In this thesis we address the second problem of tracing in detail. Our main aim is to find the best approach to solve this problem.

2. Literature

The methods available to compute intersection curves fall broadly into the following classes[2-4]: (a) Recursive subdivision methods; (b) Algebraic methods; (c) Geometric methods; (d) Lattice evaluation methods; and (e) Marching methods. Marching methods have proved to be popular as evidenced by the large number of published algorithms using these. Also, compared to the other methods, they give a much more efficient solution of the tracing problem. As the focus of this thesis is on marching methods we only describe these in greater detail. Marching methods[4,5] generate sequence of points, on or near the required intersection curve, by stepping from a current point in a direction controlled by the local differential geometry of the surfaces involved. The methods in this class use the local differential geometry of the intersecting surfaces to set up a system of ordinary differential equations (ODEs) such that the solution curves of these ODEs correspond to the desired intersection curves (most methods do not explicitly set up the ODE). The ODEs are then solved numerically to get an approximation to the intersection curves. At present most of the marching algorithms are scattered in the literature. All of them seem to share the following characteristics:

1. They generate a discrete set of points on $g^{-1}(0)$. This is not good enough for geometric modelling applications. Ideally, a continuously differentiable function, X, which approximates a true paramentrization, X has to be obtained.

2. The problem can be viewed naturally as the solution of a special vector field (an ODE on a manifold). Existing methods do not exploit this formulation advantageously.

3. Most methods employ either a predictor–corrector type of method, or the Taylor series method to numerically solve the problem. Integration methods like Adams multistep methods or the Runge–Kutte (RK) methods do not appear to have been used to solve the ODE. A detailed analysis of the suitability of the various integration methods, for use in geometric modelling, has not been done. This is quite unfortunate as there exist very efficient numerical integration methods which have great relevance to the intersection curve computation problem.

3. Contributions of the thesis

Our contribution is as follows:

1. We provide a clear theory of approximation for marching methods.
2. We incorporate all marching algorithms under a single framework of approaches, *i.e.*, all existing marching schemes are particular instances of the approaches we provide.
3. We carry out a numerical testing on practical intersection problems occurring in geometric modelling applications, to identify the 'best approach' to numerically trace intersection curves.

Below we make a more detailed discussion of the contributions.

3.1. *A theory of approximation*

For α satisfying $g(\alpha) = 0$ let: $g^{-1}(0;\alpha)$ denote the connected component of $g^{-1}(0)$ containing α; and $x(.;\alpha)$ denote the unique arclength parametrization of $g^{-1}(0;\alpha)$ (assuming that the curve is oriented in some way). Given x_0 the aim is to determine $\bar{x}(.)$, an approximate parametrization of $g^{-1}(0;x_0)$. Let $\varepsilon > 0$ be a given tolerance. We say $\bar{x}(.)$ is *strong* ε*–approximant* if $\sup_3\{\| x(s) - x(s;x_0) \|\} \le \varepsilon$. Because marching methods employ local error control (global error control is difficult and very expensive) it is most difficult to ensure that they yield a strong ε-approximant.

In applications such as geometric modelling there is really no need to obtain a strong ε-approximant, *i.e.*, an $\bar{x}(.)$ which is close to $x(.;x_0)$ for all s. What should really be sufficient is an $\bar{x}(.)$ which satisfies the condition that R, the range of $\bar{x}(.)$, and $g^{-1}(0;x_0)$ are close to each other. This is expressed in our definition of a *weak* ε*-approximant* which requires two conditions:(*a*) $R \subset \varepsilon$-spherical extension of $g^{-1}(0;x_0)$; and (*b*) $g^{-1}(0;x_0) \subset \varepsilon$-spherical extension of R. It is easy to see that the two conditions are independent, and that both are important for R and $g^{-1}(0;x_0)$ to be close.

Condition (*a*) is easy to verify (*e.g.*, by checking the value of $g(\bar{x}(s))$ for all s). On the other hand, condition (*b*) is hard to verify, simply because $g^{-1}(0;x_0)$ is unknown to us. Suppose x_f is some final point to be reached (x_f may be implicitly defined, for example, as the intersection of $g^{-1}(0;x_0)$ with a thrid surface) and the aim is to track that part of $g^{-1}(0;x_0)$ from x_0 to x_f. We formally show that, if $\in$ is small enough, condition (*a*) is satisfied, and the endpoint of $\bar{x}(\cdot)$ lies on $g^{-1}(0)$ but is different from x_0, then $\bar{x}(\cdot)$ is a weak 5ε-approximant. We also state a conceptual marching algorithm and formally show how it can be used to obtain a weak ε-approximant.

3.2. *Setting up the vector field*

Let M be an one-dimensional manifold in R^n defined by $g(x)=0$, where $g: R^n \to R^{n-1}$ is such that rank $g_x(x) = n-1 \ \forall x \in g^{-1}(0)$, and $g_x(x)$ denotes the $(n-1) \times n$ Jacobian matrix of g evaluated at x. Let $x(s)$ denote the arclength parametrization of M. It is easy to formulate $x(s)$ as the solution of a vector field. The ODE

$$\dot{x} \underline{\underline{\Delta}} \frac{dx}{ds} = F(x), \tag{1}$$

where $y = F(x)$ is the unique vector satisfying $g_x(x)y = 0$, $\| y \| = 1$, y being along the orientation direction, defines this field on M. In other words, if T_xM denotes the tangent space of M at $x \in M$, then $F(x) \in T_xM \ \forall x \in M$. We suggest three approaches for solving the vector field. They are: Parametrization approach; Perturbation approach; and Differential-algebraic approach. Here we give a brief discussion of their basic working. The thesis discusses these approaches and their suitability for curve tracing in detail.

Parametrization approach: In this approach, we solve at an $\bar{x}_k \in M$, a local ODE involving a single dependent variable. Let $T = F(\bar{x}_k)$ and U be an $n \times (n-1)$ matrix such that $[T|U]$ is an orthogonal matrix. At $\bar{x}_k$ M can be locally parametrized as

$$x(t) = \bar{x}_k + Tt + Uz(t) \tag{2}$$

where $t \in R$ denotes movement along the tangential direction at x_k, and given t, $z(t)$ is the unique solution (nearest to $z = 0$) of

$$g(\bar{x}_k + Tt + U\,z(t)) = 0. \tag{3}$$

From (1) and (2), and after some simplifications we get

$$\frac{dt}{ds} = \dot{t} = < T, F(x(t)) > \overset{\Delta}{=} \rho(t) \tag{4}$$

where $< x, y >$ stands for the inner product of x and y. This local ODE can be solved using a numerical integration method, and using (2) we get a corresponding approximation for the intersection curve.

Perturbation approach: In this approach, a correction is applied to the numerical solution of (1) after each integration step, so as to satisfy $g(x) = 0$. Suppose at the kth step, we have $x_k \in M$, the solution approximant at $s = s_k$. Let $x(.)$ be the local solution of (1) satisfying $x(s_k) = x_k$. Let T denote the integration tolerance. In the $(k+1)$th step the aim is to determine a step size h_k and an $x_{k+1} \in$ M that satisfies.

$$\| x(S_{k+1}) - x_{k+1} \| \le r, \tag{5}$$

where $s_{k+1} = s_k + h_k$. This can be done as follows:

1. Numerically integrate (1) from $x(s_k) = x_k$ using local error control (without concern for the constraint $g(x)=0$) to obtain a step size h_k, and an approximant, $\bar{x}_{k+1}$ that satisfy $\| x(s_{k+1}) - \bar{x}_{k+1} \| \le \tau/2$.
2. Solve the problem

   $$\min \| x - \bar{x}_{k+1} \| \text{ subject to } g(x) = 0;$$

   and set x_{k+1} = the minimizer obtained.

It is easy to show that the x_{k+1} determined by these two steps satisfies (5).

Differential–algebraic approach: In this approach, we treat both the vector field (1) and the algebraic constraints $g(x)=0$, simultaneously. Though the idea appears simple, there is an important numerical difficulty associated with it. The combined system, though consistent is overdetermined with $(2n-1)$ equations required to determine the n-dimensional vector function $x(s)$. Using an idea suggested by Gear[6], we convert the overdetermined system to a square system of differential–algebraic equations (DAEs) of the form

$$\begin{aligned} \dot{x} &= f(x) + g_x(x)^T \dot{z} \\ g(x) &= 0, \end{aligned} \tag{6}$$

where $z(s) \in R^{n-1}$ is an extra vector of variables introduced to make the system square. We establish that every solution of (6) starting from $x_0 \in M$ yields $z \equiv 0$ so that (6) is indeed equivalent to the original system. We solve (6) using special numerical techniques to get an approximation of the intersection curve.

Integration methods: The problem that we solve involves integrating the vector field (1) over a given interval $[s_0, s_f]$. To do this we use discrete variable methods[7-9] like: Taylor series methods; Runge–Kutta (RK) methods such as RK34, RK Fehlberg, and RK DPS; multistep Adams methods; and implicit methods employing backward difference formulas (BDFs). All these methods employ local error control, and ensure that the endpoints of each integration step lie within a tolerance region of the intersection curve.

Numerical testing: We use the following measures to judge the effectiveness of a numerical curve tracing algorithm:

1. cost of computing;
2. accuracy of the approximation;
3. data overhead for storing the intersection curve approximant.

Combining the three approaches with the appropriate integration methods we obtain a range of curve tracing methods. It is interesting to note that all the marching methods described in the literature are special cases of one of the combinations. For example, the numerical curve tracing algorithm of Bajaj *et al.*[5] is nothing but a combination of the Perturbation approach with the Taylor series method. For the sake of comparison the following combinations of approaches/methods are made:

1. Perturbation–RK methods, Adams, Taylor series
2. Parametrization–RK methods
3. Differential–Algebraic approach– BDF.

The objective behind the testing is to compare the various combinations and to make a choice as to a 'best surface intersection curve tracing procedure'. From our testing we have found the Perturbation approach coupled with the RK DPS method to perform significantly better than the other combinations and recommend this combination for curve tracing applications in geometric modelling.

References

1.	Requicha, A. A. G. and Voelcker, H. B.	Solid modelling: a historical summary and contemporary assessment, *IEEE Comp. Graphics Applic.*, 1982, 2(2), 9–24.
2.	Boender, E.	A survey of intersection algorithms for curved surfaces, *Comput. Graphics*, 1991, 15, 109–115.
3.	Lukacs, G.	The generalized inverse matrix and the surface–surface intersection problem, *Theory and practice of geometric modelling* (W. Straser, H-P. Seidel, eds), pp. 167–185, 1989, Springer Verlag.
4.	Pratt, M. J. and Geisow, A. D.	Surface/surface intersection problems, *The mathematics of surfaces*. (J.A.Gregory, ed.), 1986, pp. 117–142, Clarendon Press.
5.	Bajaj, C. L., Hoffman, C. M., Lynch, R. E. and Hopcroft, J. E. H.	Tracing surface intersections, *Comput. Aided Geometric Des.*, 1988, 5, 285–307.
6.	Gear, C. W.	The simultaneous numerical solution of differential–algebraic equations, *IEEE Trans.*, 1971, TC-18, 89–95.
7.	Forsythe, G. E., Malcolm, M. A. and Moler, C. B.	*Computer methods for mathematical computations*, 1977, Prentice-Hall.
8.	Shimpine, L. F.	Some practical RK formulas, *Math Comput.*, 1986, 46, 135–150.
9.	Hall, G. and Watt, J. M. (eds)	*Modern numerical methods for ordinary differential equations*, 1976, Clarendon Press.